# Search for Rare Multi-Pion Decays of the Tau Lepton Using the BABAR Detector

Ruben Ter-Antonyan

SLAC-R-879

Prepared for the Department of Energy
under contract number DE-AC02-76SF00515

Printed in the United States of America. Available from the National Technical Information Service, U.S. Department of Commerce, 5285 Port Royal Road, Springfield, VA 22161.

# SEARCH FOR RARE MULTI-PION DECAYS OF THE TAU LEPTON USING THE *BABAR* DETECTOR

DISSERTATION

Presented in Partial Fulfillment of the Requirements for
the Degree Doctor of Philosophy in the
Graduate School of The Ohio State University

By

Ruben Ter-Antonyan, M.S.

* * * * *

The Ohio State University
2006

| Dissertation Committee: | Approved by |
|---|---|
| Richard D. Kass, Adviser | |
| Klaus Honscheid | |
| Michael A. Lisa | Adviser<br>Physics Graduate Program |
| Junko Shigemitsu | |
| Ralph von Frese | |

# ABSTRACT

A search for the decay of the $\tau$ lepton to rare multi-pion final states is performed using the *BABAR* detector at the PEP-II asymmetric-energy $e^+e^-$ collider. The analysis uses $232\,\mathrm{fb}^{-1}$ of data at center-of-mass energies on or near the $\Upsilon(4\mathrm{S})$ resonance. In the search for the $\tau^- \to 3\pi^-2\pi^+2\pi^0\nu_\tau$ decay, we observe 10 events with an expected background of $6.5^{+2.0}_{-1.4}$ events. In the absence of a signal, we calculate the decay branching ratio upper limit $\mathcal{B}(\tau^- \to 3\pi^-2\pi^+2\pi^0\nu_\tau) < 3.4 \times 10^{-6}$ at the 90 % confidence level. This is more than a factor of 30 improvement over the previously established limit. In addition, we search for the exclusive decay mode $\tau^- \to 2\omega\pi^-\nu_\tau$ with the further decay of $\omega \to \pi^-\pi^+\pi^0$. We observe 1 event, expecting $0.4^{+1.0}_{-0.4}$ background events, and calculate the upper limit $\mathcal{B}(\tau^- \to 2\omega\pi^-\nu_\tau) < 5.4 \times 10^{-7}$ at the 90 % confidence level. This is the first upper limit for this mode.

In the search for the $\tau^- \to 4\pi^-3\pi^+(\pi^0)\nu_\tau$ decay, we observe 24 events with an expected background of $21.6 \pm 1.3$ events. In the absence of a signal, we calculate the upper limit $\mathcal{B}(\tau^- \to 4\pi^-3\pi^+(\pi^0)\nu_\tau) < 3.0 \times 10^{-7}$ at the 90 % confidence level. This is an improvement by nearly an order of magnitude over the previously established limit. In addition, we set the first upper limits for the exclusive seven-pion decays $\mathcal{B}(\tau^- \to 4\pi^-3\pi^+\nu_\tau) < 4.3 \times 10^{-7}$ and $\mathcal{B}(\tau^- \to 4\pi^-3\pi^+\pi^0\nu_\tau) < 2.5 \times 10^{-7}$.

We also study the $\tau^- \rightarrow 3\pi^-2\pi^+\pi^0\nu_\tau$ mode and measure its branching ratio $\mathcal{B}(\tau^- \rightarrow 3\pi^-2\pi^+\pi^0\nu_\tau) = (1.79 \pm 0.04 \pm 0.14) \times 10^{-4}$, which is consistent with and more precise than the measurements from other experiments.

Dedicated to

my lovely wife Katya, our newborn daughter Natalie,

and my parents Susanna and Samvel.

# ACKNOWLEDGMENTS

I wish to express my gratitude to a group of people without whom this work would have never been possible.

Foremost, I thank my family: my wife Katya, who was always there for me and shared my joy and frustration; my newborn daughter Natalie, who, even as an unborn child, motivated me to work hard and defend in time, right before her birthday; my parents and my brother, who were always incredibly encouraging and supportive.

I wish to express my deepest appreciation to my advisor, wise and all-knowing Professor Richard Kass, whose help and guidance in my research were invaluable. He passed me his knowledge and experience for which I am very grateful. I have learned a lot from him in and outside the physics world. I could not have done this work without his support.

I would like to thank my collaborators at SLAC, Dr. Carsten Hast and Dr. Thomas Allmendinger for their colossal help and support in this research project. They have had a tremendous impact on this analysis.

I am grateful to Professor K.K. Gan, the $\tau$ guru, for his thoughtful advice on $\tau$ physics. He also supervised my hardware project for the ATLAS experiment at the LHC. Not only did he teach me everything about the pixel detector, he also taught me to appreciate fine French and Asian cuisine!

My gratitude also goes to Professors Klaus Honscheid and Harris Kagan for fruitful discussions and comments on my research. Klaus was also a member of my dissertation committee, who I also thank for their advice and comments on my dissertation.

I thank the Tau Analysis Working Group at SLAC for helpful discussions, reviews and comments on my analysis.

I would also like to acknowledge all graduate students and postdocs who I worked with at the Ohio State University. Among them, my officemate Dirk Hufnagel - a computer wiz in demand by all the high energy physics folks at the OSU, James Morris who replaced me on the *BABAR*'s lettered release administrator job, Shane Smith - an engineer also in high demand at the OSU, Amir Rahimi, Kregg Arms, and the postdocs at SLAC: Paul (Jack) Jackson, Gabrielle Benelli and Teela Pulliam.

Last, but not the least, I thank my friends and close relatives for their support.

Everybody who showed interest and belief in this analysis, thank you!

# TABLE OF CONTENTS

**Page**

Chapters:

Appendices:

# LIST OF TABLES

**Table** **Page**

# LIST OF FIGURES

**Figure** **Page**

# CHAPTER 1

# INTRODUCTION

> "*Physics is like sex. Sure, it may give some practical results, but that's not why we do it.*" –*Richard Feynman*

A longstanding fundamental question humans have been trying to answer is "What is the world made of?" Five centuries B.C. a Greek philosopher Empedocles postulated the four fundamental elements of matter: water, earth, air and fire. Another Greek philosopher Democritus, argued that all matter is made up of various imperishable indivisible elements, $\alpha\tau o\mu o\nu$ in Greek, or atoms in English. Today we realize that the word "atom" is misleading, and atoms are not as fundamental as people thought they were for a long time. In 1909 Rutherford demonstrated that atoms are made of nucleons (protons and neutrons), bounded in a nucleus, and electrons orbiting them. However, in 1964 it was suggested by Gell-Mann and Zweig that protons and neutrons are not fundamental either and are made of *quarks*. So far all evidence suggests that quarks are fundamental. Electrons, which are another constituent of an atom, are also fundamental. They belong to the *lepton* family. Both quarks and leptons are presently thought of as the fundamental building blocks of nature.

The theory, or rather a collection of related theories, describing the properties and interactions of fundamental particles (except gravity) is called the *Standard*

*Model*. It incorporates theories of quantum electrodynamics, quantum chromodynamics and the weak processes. The Standard Model has been quite successful in describing observations in elementary particle physics for the last 30 years. Its predictions are accurate and are confirmed by various experiments. Despite its efficiency, the Standard Model is not complete, and there is plenty of indirect evidence for exciting new physics "beyond the Standard Model".

## 1.1 The Standard Model

This section is divided into two, first an introduction to the fundamental particles and their properties, then a discussion of the forces and interactions between them.

### 1.1.1 The Fundamental Particles

According to the Standard Model, all matter is made of six leptons and six quarks. Also, for every matter particle, there is an antiparticle with exactly the same mass but opposite-signed additive quantum numbers (e.g. electric charge). Leptons are divided into three families (see Table 1.1), the first (electron) family being the lightest. The electrons ($e$), muons ($\mu$) and taus ($\tau$) have a negative charge, while the neutrinos are electrically neutral. Each of the leptons carries its own family lepton number. In the Standard Model lepton number is always conserved. For instance, the $\tau$ lepton decay is always accompanied with a $\nu_\tau$ neutrino to conserve the $\tau$ lepton number.

There are six quarks with six different "flavors", shown in Table 1.1. The up ($u$), charm ($c$) and top ($t$) quarks have a positive charge +2/3 (in units of electron charge), while the down ($d$), strange ($s$) and bottom ($b$) quarks have a negative charge -1/3. Both leptons and quarks are spin-1/2 particles, or fermions, divided into three generations. What we see in nature surrounding us is made of the first generation quarks and leptons. For instance, protons and neutrons are made of ($uud$) and ($udd$) quark combinations. Second and third generation quarks and leptons decay quickly into quarks and leptons of the first generation. For instance, the $\tau$ leptons can decay to muons, which will in turn decay to first generation electrons.

| **Leptons** | Mass (MeV/$c^2$) | Charge | **Quarks** | Mass (GeV/$c^2$) | Charge |
|---|---|---|---|---|---|
| $e$ | 0.511 | -1 | $u$p | 0.002-0.004 | +2/3 |
| $\nu_e$ | $< 3 \times 10^{-6}$ | 0 | $d$own | 0.002-0.004 | -1/3 |
| $\mu$ | 105.658 | -1 | $c$harm | 1.15-1.35 | +2/3 |
| $\nu_\mu$ | <0.19 | 0 | $s$trange | 0.08-0.13 | -1/3 |
| $\tau$ | 1777.0±0.3 | -1 | $t$op | 174.3±5.1 | +2/3 |
| $\nu_\tau$ | <18.2 | 0 | $b$ottom | 4.1-4.4 | -1/3 |

Table 1.1: Three generations of leptons and quarks and their properties [6].

Unlike leptons, quarks are never found in isolation. They are confined to groups with other quarks, forming baryons (bound state of three quarks) and mesons (bound state of a quark-antiquark pair).

Besides flavors, quarks also carry three colors (“red”, “green”, and “blue”). This was originally suggested to avoid the violation of the Pauli exclusion principle forbidding more than one spin-1/2 fermion to occupy the same state, as would happen with the $\Delta^{++}(uuu)$ resonance. However, hadrons formed from the bound states of quarks are color-neutral, meaning they either carry all three colors (the baryons), or color-anticolor (the mesons).

### 1.1.2 The Fundamental Forces

There are four known forces responsible for interactions between the fundamental particles: strong, electromagnetic, weak and gravitational. In everyday life we only encounter the gravitational and electromagnetic forces. The weak and strong forces are responsible for interactions like particle decays and nuclear binding. Each force is mediated by an interaction-specific particle, a gauge boson (integer-spin particle). Particles interact by exchanging gauge bosons. These force-carrier particles are fundamental, but are not considered as matter particles. The properties of the gauge bosons are shown in Table 1.2 for each of the forces.

| Force | Mediator | Charge | Spin | Mass (GeV/c$^2$) | Range (m) |
|---|---|---|---|---|---|
| Strong | gluon ($g$) | 0 | 1 | 0 | $< 10^{-15}$ |
| Electromagnetic | photon ($\gamma$) | 0 | 1 | 0 | $\infty$ |
| Weak | $W^{\pm}$, $Z^0$ bosons | $\pm 1$, 0 | 1 | 80.4, 91.2 | $< 10^{-15}$ |
| Gravity | graviton | 0 | 2 | 0 | $\infty$ |

Table 1.2: Fundamental forces and associated mediators.

The strength of each of the forces depends on the range of the interaction in a complicated way. The strong and weak forces become noticeable only at interaction ranges smaller than $10^{-15}$ m, while the electromagnetic and gravitational forces have infinite range. I will give a short description of each force below.

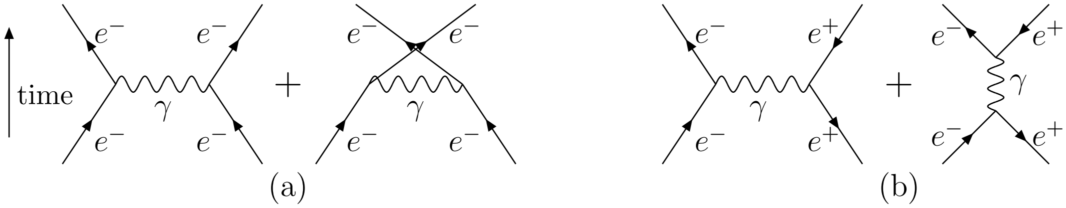

Figure 1.1: Feynman diagrams of electromagnetic interactions between two electrons in Moeller scattering (a); and electron and positron in Bhabha scattering (b).

**Electromagnetic force**

The electromagnetic force is well known and well studied. Most of the technology we use is based on electromagnetism. The theory that describes it is called quantum electrodynamics (QED).

The electromagnetic field is propagated by a photon. A simple Coulomb repulsion (or *Moeller scattering*) of two electrons is nothing else but a photon exchange between the electrons, depicted in Figure 1.1 as a Feynman diagram. For comparison, the same figure contains a Feynman diagram of the Coulomb attraction between the electron and positron. The process can also go through $e^+e^-$ annihilation and creation. In QED this process $e^- + e^+ \rightarrow e^- + e^+$ is called *Bhabha scattering*[1]. The exchange photon is "virtual" and cannot be observed.

The strength of the electromagnetic interaction is characterized by the fine structure constant $\alpha = (e^2/\hbar c) = 1/137$. In fact, each vertex contributes a square-root of this factor, therefore multi-vertex Feynman diagrams usually make a negligible contribution to the analyzed process.

---

[1] This process has a significant impact on the $e^+e^-$-colliding experiments due to its large cross-section.

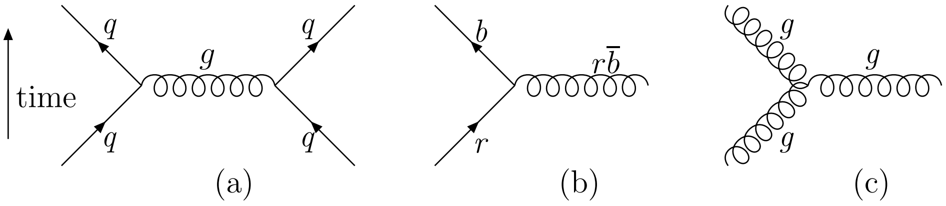

Figure 1.2: Feynman diagrams of strong interactions: (a) interaction between two quarks by a gluon exchange; (b) quark color changing at the vertex and emitting a gluon carrying the color difference. (c) direct gluon-gluon coupling.

### Strong force

The strong force is described by quantum chromodynamics (QCD). When it comes to very short range particle interactions, this force is the strongest of the four. However, the strong force only couples to quarks. Mediators of the strong force are called gluons. Gluons, like quarks, are color-charged particles (unlike the photon, which is electrically neutral). Quarks interact by exchanging gluons, which can also interact among themselves (see Figure 1.2). As a quark emits a gluon, it changes color, and the gluon carries the initial quark color and the final quark anti-color. Similar to the charge conservation in QED, the color is always conserved in QCD. So is the quark flavor.

The color force field created by a gluon exchange is very strong and holds the quarks together. Unlike the electromagnetic force, the strong force strengthens when the distance between the quarks increases, so it is very hard to pull two quarks apart. If that happens (e.g. as a result of a high-energy collision of quarks) a quark-antiquark pair is created and one of the quarks is coupled to the isolated quark, forming a meson.

An example of strong interaction between quarks as a result of a proton-antiproton collision ($p\overline{p} \rightarrow n\overline{n}$) is shown in Figure 1.3. Here, the $\overline{u}$ and $u$ quarks annihilate emitting a gluon, while another $\overline{u}$ quark from an antiproton emits a gluon which creates $d\overline{d}$ quark pair. As a result, a pair or neutron-antineutron is created.

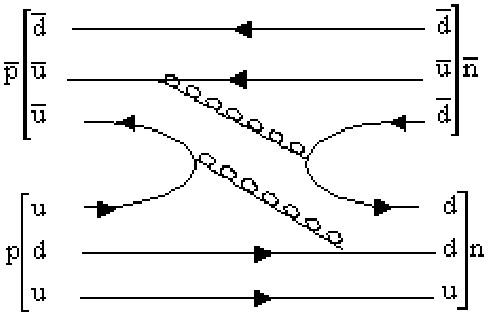

Figure 1.3: Feynman diagram illustrating strong interaction between quarks in the $p\overline{p} \rightarrow n\overline{n}$ process.

### Weak force

Like the strong force, the weak force is a very short-range force, noticeable at the nuclear scale. It is responsible for processes like a particle decay and nuclear radioactivity. In particular, the decay of the $\tau$ lepton, which is the topic of this thesis, is a result of the weak interaction. All particles (quarks and leptons) interact weakly. The mediator of the weak force is either a charged $W^{\pm}$, or a neutral $Z^0$ boson, depending on the process. Both are rather massive (see Table 1.1) but still fundamental particles. When a charged lepton decays or converts to a neutrino, or a negatively charged quark ($d$, $s$, and $b$) converts to a positively charged quark ($u$, $c$ and $t$ respectively), a charged $W$ boson is emitted. A neutral $Z^0$ boson is

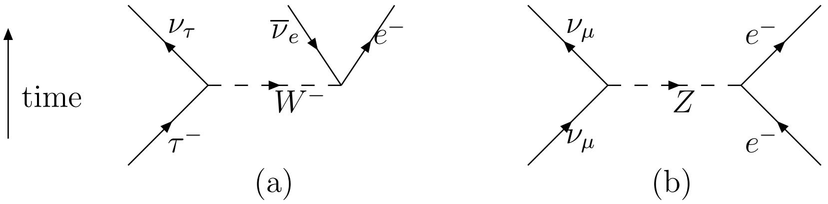

Figure 1.4: Feynman diagrams of weak interactions: (a) tau decay $\tau^- \rightarrow e^-\nu_\tau\overline{\nu}_e$; (b) neutrino-electron scattering $\nu_\mu e^- \rightarrow \nu_\mu e^-$.

emitted when a quark or a lepton turn into their anti-particles, or in the process of scattering. In any case, the charge is conserved. Examples of weak interactions are shown in Figure 1.4 as Feynman diagrams.

The vertex of weak interacting leptons connects only same generation leptons, so the lepton number is always conserved. The quarks, however, do not conserve flavor in weak interactions, as they do in strong interactions. If a charged $W$ is emitted, the quark changes its flavor and its charge. A typical example of a neutron weak decay $n \rightarrow pe^-\overline{\nu}_e$ is shown in Figure 1.5. Here a "down" quark decays to an "up" quark and emits a $W^-$, which creates a pair of same generation leptons.

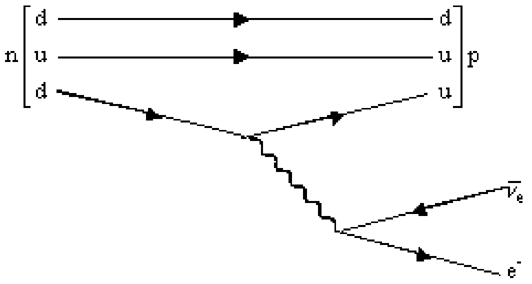

Figure 1.5: Feynman diagram of a neutron decay $n \rightarrow pe^-\overline{\nu}_e$, illustrating the weak interaction of the quarks.

Quarks favor couplings within the same generation. Couplings with different-generation quarks are possible, but not favored. Instead of coupling to the physical $d$, $s$, and $b$ quarks, the $u$, $c$ and $t$ quarks couple to mass eigenstates $d'$, $s'$, and $b'$,

$$\begin{pmatrix} u \\ d' \end{pmatrix} \begin{pmatrix} c \\ s' \end{pmatrix} \begin{pmatrix} t \\ b' \end{pmatrix} \tag{1.1}$$

where $d'$, $s'$, and $b'$ can be written as

$$\begin{pmatrix} d' \\ s' \\ b' \end{pmatrix} = \begin{pmatrix} V_{ud} & V_{us} & V_{ub} \\ V_{cd} & V_{cs} & V_{cb} \\ V_{td} & V_{ts} & V_{tb} \end{pmatrix} \begin{pmatrix} d \\ s \\ b \end{pmatrix} \tag{1.2}$$

This 3×3 matrix is called the Cabibbo-Kobayashi-Maskawa (CKM) matrix. The matrix elements are measured experimentally:

$$\begin{pmatrix} 0.9741-0.9756 & 0.219-0.226 & 0.0025-0.0048 \\ 0.219-0.226 & 0.9732-0.9748 & 0.038-0.044 \\ 0.004-0.014 & 0.037-0.044 & 0.9990-0.9993 \end{pmatrix}. \tag{1.3}$$

**Gravitational force**

The gravitational force is not included in the Standard Model. Its effect is dramatic in our everyday life, but negligible for the fundamental particles and their interactions. The mediator of gravity is believed to be a spin-2 boson called *graviton*, but it has not been observed to date. Gravity is described by the General Relativity theory.

## 1.2 The $\tau$ Lepton

This section contains details on one of the fundamental particles of the Standard Model - the $\tau$ lepton. It is divided into two subsections, one describing the discovery and the basic properties of the $\tau$, the other discussing theoretical calculations of multi-pion $\tau$ decays, which is directly related to this dissertation topic.

### 1.2.1 Discovery of the $\tau$ Lepton and its Properties

The $\tau$ is the heaviest (3500 times heavier than an electron) and the most short-lived (decays 10 million times faster than a muon) lepton. It was discovered in 1975 by Martin Perl and his co-workers from the MARK I collaboration [1]. Back then muons were easily produced in $e^+e^- \to \mu^+\mu^-$ collisions, and if there were new charged leptons $L$ they would be observed in a similar way ($e^+e^- \to L^+L^-$) once the $e^+e^-$ collision energy was larger than twice the mass of the new lepton $L$. Among various possible decay channels, the $L$ lepton should decay into lighter electrons and muons with corresponding neutrinos (3-body decays). A clear signature for such an event would be e.g. $L_1 \to e\overline{\nu}_e\nu\tau$ and $L_2 \to \mu\overline{\nu}_\mu\nu\tau$ (or vice versa). It was observed in 1974 at the Stanford Linear Accelerator Center with the collision energy reaching 4.8 GeV (see the event diagram and the observation in Figure 1.6). It took M. Perl and his colleagues a year to prove that the events were not background, such as charm events or standard QED processes [2]. The $\tau$ discovery was later confirmed by PLUTO [3] and DASP [4] experiments in Germany. In 1977 the lepton was named '$\tau$' as the first letter of the Greek word $\tau\rho\iota\tau o\nu$, meaning 'third' [5]. Thus, the $\tau$ lepton started the third generation of fundamental particles. In 1995 M. Perl received the Nobel Prize for the discovery of the $\tau$.

Some of the most important properties [6] of the $\tau$ lepton are:

- Produced in pairs in $e^+e^-$ collisions (see Figure 1.7) with a cross-section $\sigma(e^+e^- \to \tau^+\tau^-) = 0.89\,\mathrm{nb}$ (at the CM energy of the *BABAR* experiment)
- Mass: $M_\tau \;=\; 1777.0 \pm 0.3\,\mathrm{MeV/c^2}$
- Lifetime: $\tau \;=\; 290.6 \pm 1.1\,\mathrm{fs}$

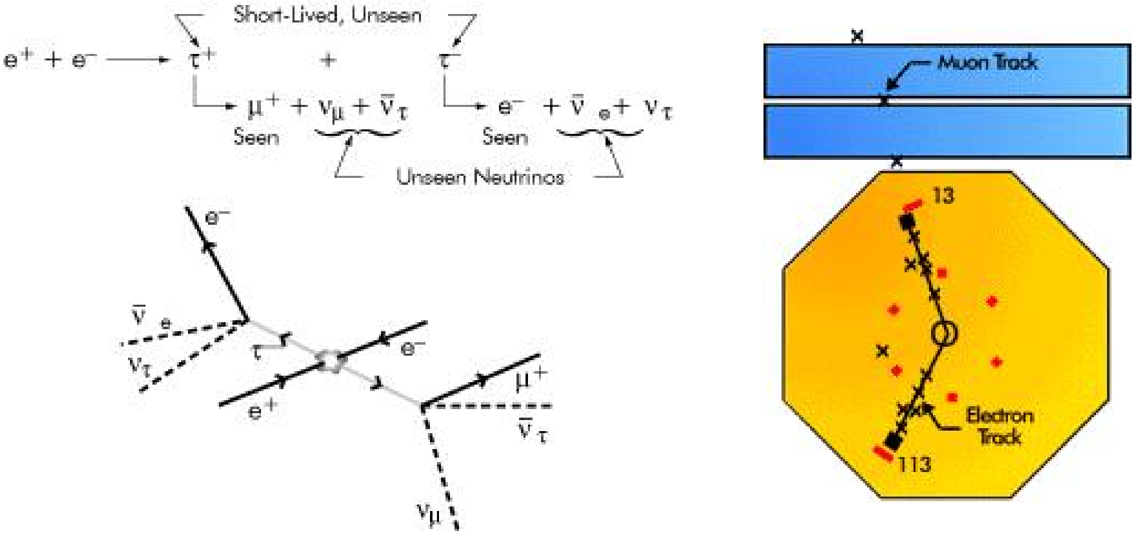

Figure 1.6: The diagrams of $e^+e^- \to \tau^+\tau^-$ event with further decays of the $\tau$ leptons (left) and observation in the MARK I detector (right).

- Interacts via electromagnetic and weak forces
- The only lepton able to decay to hadrons as well as to leptons
- Decays are always accompanied by a $\tau$ neutrino (in SM)
- ~85% of the time the $\tau$ decays to 1 charged track + neutrino (1-prong decay) with or without neutrals

The $\tau$ discovery was based on 24 observed $e^+e^- \to \tau^+\tau^-$ events. Nowadays, high-luminosity experiments like *BABAR* and Belle produce hundreds of millions of $\tau$ leptons, allowing precision measurements and searches for new decay modes. *Branching ratios* (see Appendix A) of $\tau$ decays are shown in Table 3.1. Current 'hot' $\tau$ studies include: search for lepton flavor violating decays, ($\tau \to l\gamma$, $\tau \to lll$, etc) search for second-class currents (e.g $\tau \to \eta\pi\nu_\tau$, see Appendix A), strange

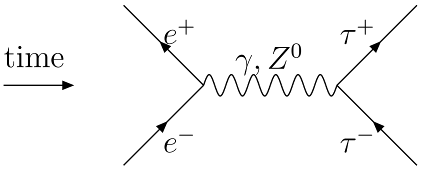

Figure 1.7: Feynman diagram of the $\tau$-pair production in $e^+e^-$ collisions.

spectral function measurements (decays involving kaons), CP-violating decay ($\tau \to K_{S,L}\pi\nu_\tau$), multi-hadron decays via resonances, and $\nu_\tau$ mass limit.

### 1.2.2 Multi-pion Decays of the $\tau$ Lepton

To date, $\tau$ decays with up to 6 pions and a neutrino have been observed. The branching ratio of the $\tau^- \to 3\pi^-2\pi^+\pi^0\nu_\tau$ decay is $\mathcal{B}(\tau^- \to 3\pi^-2\pi^+\pi^0\nu_\tau) = (1.81 \pm 0.27)\times 10^{-4}$ [6]. The first attempt to measure the branching ratio of the 7-pion decay mode $\tau^- \to 4\pi^-3\pi^+\nu_\tau$ was made by the HRS experiment in 1987 [7]. They failed to see any evidence for a signal and set an upper limit $\mathcal{B}(\tau^- \to 4\pi^-3\pi^+\nu_\tau) < 2.9\times 10^{-4}$. So did two other experiments 10 years later: OPAL set $\mathcal{B}(\tau^- \to 4\pi^-3\pi^+\nu_\tau) < 1.8 \times 10^{-5}$ [8] and CLEO set $\mathcal{B}(\tau^- \to 4\pi^-3\pi^+\nu_\tau) < 2.4 \times 10^{-6}$ [9] upper limits at 90% confidence level. The question then was, how small is the 7-pion $\tau$ decay branching ratio? The decay is allowed in the Standard Model. Before we discuss who is to blame for non-observation of the $\tau^- \to 4\pi^-3\pi^+\nu_\tau$ decay, we briefly discuss Fermi's "Golden Rule" for calculating decay rates.

The decay rate (see Appendix A) is determined by the amplitude of the decay, which contains the dynamical information of the process, and the available phase space, providing kinematical information based on the masses, energies and momenta of initial and final decay products:

$$d\Gamma = \frac{1}{2E_0}|\mathcal{M}|^2 \frac{d^3\mathbf{p}_1}{(2\pi)^3 2E_1} \ldots \frac{d^3\mathbf{p}_n}{(2\pi)^3 2E_n}(2\pi)^4\delta^4(p_0 - p_1 - \ldots - p_n) \tag{1.4}$$

where a particle with index 0 decays to $n$ other particles with different energies and momenta. The $\mathcal{M}$ here refers to the amplitude (or the matrix element) of the decay, while all the other coefficients refer to the phase space (or the density of final states). The high multiplicity $\tau$ decays, like the seven-pion decay mode we are searching for, have considerably smaller available phase space compared to the lower multiplicity decays, which decreases their decay rates. Similarly, the decays to heavier particles have smaller phase space than the decay to lighter particles.

The calculation of the amplitude $|\mathcal{M}|$ for two-body and three-body decays can sometimes be done using the "Feynman rules" of evaluating the Feynman diagrams of the decays. For example, in the case of the three-body decay $\tau^- \to e^-\nu_\tau\overline{\nu}_e$ (see Feynman diagram on Figure 1.4 (left)), the amplitude can be derived following the Feynman rules [10]:

$$|\mathcal{M}|^2 = \left(\frac{g_W}{M_W}\right)^4 m_\tau E_{\overline{\nu}_e}(m_\tau - 2E_{\overline{\nu}_e}) \tag{1.5}$$

in the $\tau$ rest frame. Here, $g_W = \sqrt{4\pi\alpha_W}$ is the weak coupling constant. Skipping the phase space calculations, the decay rate yields [11]:

$$\Gamma(\tau^- \to e^-\nu_\tau\overline{\nu}_e) = \frac{G_F^2 m_\tau^5}{192\pi^3}(1 + \delta_l) \tag{1.6}$$

where $G_F = \frac{\sqrt{2}}{8}\left(\frac{g_W}{M_W}\right)^2$ is called the Fermi coupling constant, and $\delta_l$ is a small correction factor due to finite mass of the electron, QED radiative processes and the $W^\pm$ propagator. The decay rate of the $\tau^- \to \mu^-\nu_\tau\overline{\nu}_\mu$ mode is the same, except for the correction factor. The branching ratio is calculated from

$$\mathcal{B}(\tau^- \to l^-\nu_\tau\overline{\nu}_l) = \frac{\Gamma(\tau^- \to l^-\nu_\tau\overline{\nu}_l)}{\Gamma_{tot}} \tag{1.7}$$

where $l$ stands for a lepton ($e$ or $\mu$), and $\Gamma_{tot}$ is the total decay rate of the $\tau$. Given that $\Gamma_{tot} = 1/\tau$, and $\tau = 290.6 \pm 1.1$ fs, the branching ratios of the leptonic $\tau$ decays are $\mathcal{B}(\tau^- \to e^- \nu_\tau \overline{\nu}_e) = (17.772 \pm 0.075)\%$ and $\mathcal{B}(\tau^- \to \mu^- \nu_\tau \overline{\nu}_\mu) = (17.282 \pm 0.073)\%$. These calculations are in good agreement with the experimentally measured branching ratios within their errors [6].

For the hadronic decays of the $\tau$ lepton, the $W^\pm$ couples to a quark-antiquark pair, which is then exposed to strong interactions combining with quarks and antiquarks spontaneously created from the vacuum to form hadrons. This hadronization process is rather complicated and its calculation is not straightforward. The amplitude of the hadronic $\tau$ decays is given by [11]:

$$i\mathcal{M} = \frac{4G_\mathrm{F}}{\sqrt{2}} J_\tau^\mu J_\mu^{had} \tag{1.8}$$

where $J_\tau^\mu$ is a standard left-handed leptonic current and $J_\mu^{had}$ is a hadronic current not known a priori. In a simple case of $\tau^- \to \pi^- \nu_\tau$ decay, shown in Figure 1.8 (a), the hadronic current can be written as $J_\mu^\pi = \cos\theta_C f_\pi p_\mu$ [11], where $\theta_C$ is the Cabibbo angle, $f_\pi \simeq 93.3\,\mathrm{MeV}$ is the pion decay constant, and $p_\mu^\pi$ is its four-momentum. The strength of the weak current coupling to the pion is determined by the $f_\pi \cos\theta_C$ factor. The decay rate of this simplest pionic mode is calculated to be:

$$\Gamma(\tau^- \to \pi^- \nu_\tau) = \frac{G_F^2 f_\pi^2 \cos^2\theta_C}{16\pi} m_\tau^3 \Big(1 - \frac{m_\pi^2}{m_\tau^2}\Big)^2 \tag{1.9}$$

This yields a branching ratio of (10.87±0.05)%, which is in reasonable agreement with the measured value of (11.08±0.13)% [11].

The calculation of the multi-pion decay rates is much more complicated, and there is no explicit solution, especially for exclusive decays involving resonances. To conserve the G-parity [10, 11], the multi-pion $\tau$ decays proceed through axial-vector

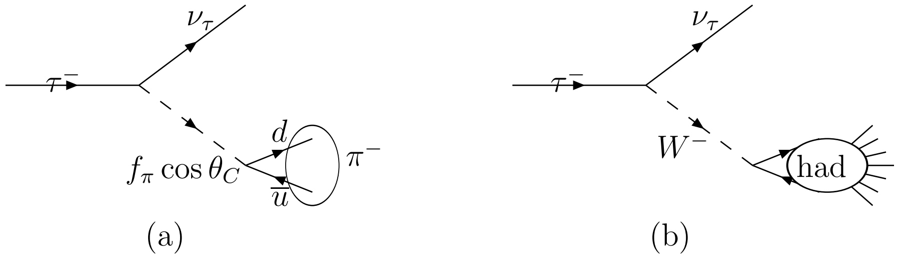

(a) (b)

Figure 1.8: Feynman diagrams of the $\tau^- \to \pi^-\nu_\tau$ (a) and $\tau^- \to 7\pi\nu_\tau$ (b) decays

currents. In this case, an effective field theory, called chiral perturbation theory [12], based on hadrons instead of quarks as elementary fields, can be applied to evaluate the decay rates. The theory is based on chiral Lagrangian calculations [13], and is valid for low-momentum particles in the decay $\tau^- \to 4\pi^-3\pi^+\nu_\tau$. The complete effective Lagrangian contains both lepton and hadron currents, and to the lowest order reads:

$$\mathcal{L} = \frac{G_F}{\sqrt{2}} \int d^4x \overline{\Psi}_\tau(x)\gamma_\mu\gamma_5\Psi_\nu(x)c_7(\partial_\mu\phi)\phi^6 \tag{1.10}$$

where $c_7$ is a constant term from the axial vector current for the seven-pion decay calculated in Ref. [13]. Integrating the expression 1.10 by parts and using Fermi's Golden rule, the decay rate yields

$$\Gamma(\tau^- \to 4\pi^-3\pi^+\nu_\tau) = \Big(\frac{c_7}{7}\Big)^2 \frac{G_F^2 m_\tau^3 \overline{\Phi}(m_\tau, m_\pi, m_\pi, m_\pi, m_\pi, m_\pi, m_\pi, m_\pi, 0)}{(2f_\pi)^{10}(2\pi)^{24}} \tag{1.11}$$

where $\overline{\Phi}$ is the eight-body phase space of the decay.

The phase space can be evaluated using the composition formula [13]

$$\Phi_{(n_1+n_2)}(M) = \prod \int_{(n_1 m_\pi)^2}^{\infty} dM_1^2 \int_{(n_2 m_\pi)^2}^{\infty} dM_2^2 \frac{\lambda^{1/2}(M, M_1, M_2)}{2M^2} \Phi_{n_1}(M_1)\Phi_{n_1}(M_2)\Theta(\lambda) \tag{1.12}$$

where $\lambda^{1/2} = \sqrt{[M^2 - (M_1 + M_2)^2][M^2 - (M_1 - M_2)^2]}$, $M$ is the invariant mass of the $n$-particle system, $M_1$ and $M_2$ are the masses of the subsystems with $n_1$ and $n_2$ particles, and $\Theta(\lambda)$ is the unit step function. Here, the normalization factors of $(2\pi)^{-3}$ for each final state particle in the phase space are not included in the $\overline{\Phi}$, but are present in the decay rate calculation (see eq. 1.11). Table 1.3 shows the calculated phase space (in units of $\mathrm{GeV}^{2n-2}$ for $n+1$ particles) for $n = 1, 2...8$ pions.

| $n$ in $\tau \to n\pi\nu_\tau$ | Phase space $\Phi_{n\pi}$ |
|---|---|
| 1 | 1.56111 |
| 2 | 3.10573 |
| 3 | 1.75786 |
| 4 | 0.383552 |
| 5 | 0.00354896 |
| 6 | 0.00139612 |
| 7 | $2.17774\times10^{-5}$ |
| 8 | $1.15161\times10^{-7}$ |

Table 1.3: Phase space integral for $\tau$ decays to $n$ charged pions and a neutrino [13].

The branching ratio of the seven-pion $\tau$ decay can be calculated from the expression

$$\mathcal{B}(\tau^- \to 4\pi^-3\pi^+\nu_\tau) = \mathcal{B}(\tau^- \to 3\pi^-2\pi^+\nu_\tau)\frac{\overline{\Phi}_{7\pi}}{(2\pi)^6(2f_\pi)^4\overline{\Phi}_{5\pi}}\Big(\frac{5c_7}{7c_5}\Big)^2 \qquad (1.13)$$

where the $\mathcal{B}(\tau^- \to 3\pi^-2\pi^+\nu_\tau) = 0.1\%$, the phase space factors $\overline{\Phi}_{7\pi}$ and $\overline{\Phi}_{5\pi}$ are listed in Table 1.3, and the $(5c_7/7c_5)$ factor is evaluated to be 1/30 [13]. The final prediction of the seven-pion $\tau$ decay branching ratio yields[2]

$$\mathcal{B}(\tau^- \to 4\pi^-3\pi^+\nu_\tau) \simeq 6 \times 10^{-12} \qquad (1.14)$$

---

[2] Ref. [13] assumed $\mathcal{B}(\tau^- \to 3\pi^-2\pi^+\nu_\tau) = 1\%$ by mistake, and calculated $\mathcal{B}(\tau^- \to 4\pi^-3\pi^+\nu_\tau) \simeq 6 \times 10^{-11}$

The predicted seven-pion branching ratio is hopelessly small due to the substantial decrease in the phase space (a factor of $10^{-6}$). However, if the decay goes through a resonance, like $a_1(1240)$, $a_2(1320)$, $\pi(1300)$ etc., the decay rate could be significantly enhanced, similar to the $\tau^- \to 3\pi^- 2\pi^+ \pi^0 \nu_\tau$ decays dominated by the $\omega$ and $\eta$ resonances [14]. This makes the search for the seven-pion $\tau$ decay particularly interesting, since its observation will hinge on the existence of a narrow resonance in a subchannel. Another important implication of the seven-pion $\tau$ decay is a potentially more stringent bound on the upper limit of the $\tau$ neutrino mass due to phase space limitations. The current limit $m_{\nu_\tau} < 18.2\,\mathrm{MeV}$ is based on the $\tau^- \to 3\pi^- 2\pi^+ \nu_\tau$ decays [15] with much larger phase space compared to the 7-prong decays.

In 1994 the CLEO collaboration searched for another seven-pion mode with five charged and two neutral pions, $\tau^- \to 3\pi^- 2\pi^+ 2\pi^0 \nu_\tau$, but had to set an upper limit $\mathcal{B}(\tau^- \to 3\pi^- 2\pi^+ 2\pi^0 \nu_\tau) < 1.1 \times 10^{-4}$ yet again [16]. The difference between the $\tau^- \to 3\pi^- 2\pi^+ 2\pi^0 \nu_\tau$ and $\tau^- \to 4\pi^- 3\pi^+ \nu_\tau$ mode is that the former can proceed through resonances, and turn a 7-body decay to 5- or even 3-body decay. The fact that the $\tau^- \to 3\pi^- 2\pi^+ \pi^0 \nu_\tau$ decay goes primarily through the $\tau \to \omega \pi^- \pi^+ \pi^- \nu_\tau$ channel suggests that the $\omega$ will also dominate the 7-pion decays.

Another strong argument for the 7-pion $\tau$ decays via resonant subchannels is the prediction from an isospin model [17]. In 1960 Pais showed that a system of $N\pi$ ($N = 2 - 8$) mesons can be defined by three "correlation numbers" $(N_1, N_2, N_3)$ [18]. Specific values of these numbers define the number of triplets ($N_3$), which are $3\pi$-subsystems with isospin $I = 0$ ($\omega$ state), doublets ($N_2 - N_3$), which are $2\pi$-subsystems with isospin $I = 1$ ($\rho$ state), and singlets ($N_1 - N_2$), which are the remaining single pions. For a given $N$,

$$N_1 + N_2 + N_3 = N, \qquad N_1 \geq N_2 \geq N_3 \geq 0 \tag{1.15}$$

A set of all possible configurations make up a partition of the $N\pi$ system. States belonging to a given partition have the same isospin, 1 or 0. If $(N_1 - N_3)$ and $(N_2 - N_3)$ are both even, then $I = 0$, otherwise $I = 1$. Tau decays require the $N\pi$ system to have $I = 1$. There are six 7-pion partitions, or isospin states, with $I = 1$, and four possible decay channels, shown in Table 1.4. The branching fraction coefficients of each final state in a given partition are calculated using group theory [17, 18].

| Isospin state | $\pi^-6\pi^0$ | $2\pi^-\pi^+4\pi^0$ | $3\pi^-2\pi^+2\pi^0$ | $4\pi^-3\pi^+$ |
|---|---|---|---|---|
| (700) $7\pi$ | $\frac{1}{21}$ | $\frac{4}{35}$ | $\frac{8}{35}$ | $\frac{64}{105}$ |
| (610) $\rho5\pi$ | $\frac{3}{14}$ | $\frac{3}{14}$ | $\frac{8}{35}$ | $\frac{12}{35}$ |
| (520) $2\rho3\pi$ | 0 | $\frac{1}{7}$ | $\frac{18}{35}$ | $\frac{12}{35}$ |
| (430) $3\rho\pi$ | 0 | $\frac{2}{5}$ | $\frac{3}{10}$ | $\frac{3}{10}$ |
| (421) $\omega\rho2\pi$ | 0 | $\frac{2}{5}$ | $\frac{3}{5}$ | 0 |
| (322) $2\omega\pi$ | 0 | 0 | 1 | 0 |

Table 1.4: Isospin coefficients for seven-pion states.

An observed final state of the 7-pion $\tau$ decay can be written as a linear combination of the possible isospin states using these coefficients, e.g:

$$\Gamma(\tau^- \to 3\pi^-2\pi^+2\pi^0\nu_\tau) = \frac{8}{35}\Gamma_{7\pi} + \frac{8}{35}\Gamma_{\rho5\pi} + \frac{18}{35}\Gamma_{2\rho3\pi} + \frac{3}{10}\Gamma_{3\rho\pi} + \frac{3}{5}\Gamma_{\omega\rho2\pi} + \Gamma_{2\omega\pi} \tag{1.16}$$

This suggests that if the seven-pion $\tau$ decays are in fact dominated by the $\omega$ resonance, the $\tau^- \to 3\pi^-2\pi^+2\pi^0\nu_\tau$ mode will have the largest branching ratio, and will most likely go through the $2\omega\pi$ channel.

In this thesis, I present the results of the searches for $\tau^- \rightarrow 4\pi^-3\pi^+(\pi^0)\nu_\tau$ [19], $\tau^- \rightarrow 3\pi^-2\pi^+2\pi^0\nu_\tau$ and $\tau^- \rightarrow 2\omega\pi^-\nu_\tau$ [20].

# CHAPTER 2

# THE *BABAR* EXPERIMENT

The search for the rare multi-pion decay modes of the $\tau$ lepton uses data collected with the *BABAR* detector at the PEP-II (Positron-Electron Project) asymmetric-energy $e^+e^-$ storage ring operated at the Stanford Linear Accelerator Center (SLAC) in Menlo Park, CA. The *BABAR* experiment has the largest collaboration of physicists in the country that targets the CP-violating decays of the B mesons. The specific design of the PEP-II rings [21] and the *BABAR* detector [22] optimizes the production of B mesons for CP violation studies. Indeed, the collider operates 89% of the time at the center-of-mass energy $\sqrt{s}$=10.58 GeV, the rest mass of the $\Upsilon$(4S) resonance. The cross-section for $e^+e^- \to B\overline{B}$ is 1.05 nb. Moreover, the asymmetric design of the PEP-II rings provides longitudinal boost to the $B$ mesons, which are otherwise produced almost at rest. The boost allows the separation of the decay vertexes of the $B$ and $\overline{B}$, and to determine their relative decay times. Another 11% of the time the data is taken 40 MeV below the $\Upsilon$(4S) resonance to produce non-$B\overline{B}$ events for background studies.

Although the *BABAR* detector was designed specifically to be a $B$-meson factory, it is also more than suitable for other physics topics like bottom and charm meson and $\tau$ lepton decays. In fact, with the $e^+e^- \to \tau^+\tau^-$ cross section of 0.89 nb, the *BABAR* is also a $\tau$ factory.

In this chapter, I will briefly describe the PEP-II storage rings and the main components of the *BABAR* detector.

## 2.1 The PEP-II Collider

The PEP-II facility (see Figure 2.1), completed in 1998, was constructed by a collaboration of three National Labs: SLAC, LBL and LLNL. It consists of two independent storage rings with a circumference of 2200 m each, located on top of each other in the tunnel. The 3 km linear accelerator (linac) is used as an injector of the high-momentum electron and positron beams into the storage rings. The electrons are produced by an electron gun, which uses polarized laser light to knock off the electrons from a semiconductor surface. They are then accelerated by the electric field and injected into the linear accelerator. A portion of the electrons is used to produce positrons by colliding them with tungsten and producing $e^+e^-$ pairs. The positrons are then collected and injected into the linac. Only a small portion of the linac is used for the *BABAR* experiment. The electron and positron beams are transported and injected to the PEP-II rings through dedicated bypass lines. The direction of the beams from their production to collision is controlled by bending magnets. Ultra-high vacuum, essential for a proper transport and acceleration of the beams, is maintained in the beam pipe of the linac and PEP-II rings by a state-of-the-art copper vacuum chamber.

The electron beam of 9.0 GeV is accelerated in the high-energy ring (HER) and collided with the counter-rotating positron beam of 3.1 GeV. The positron

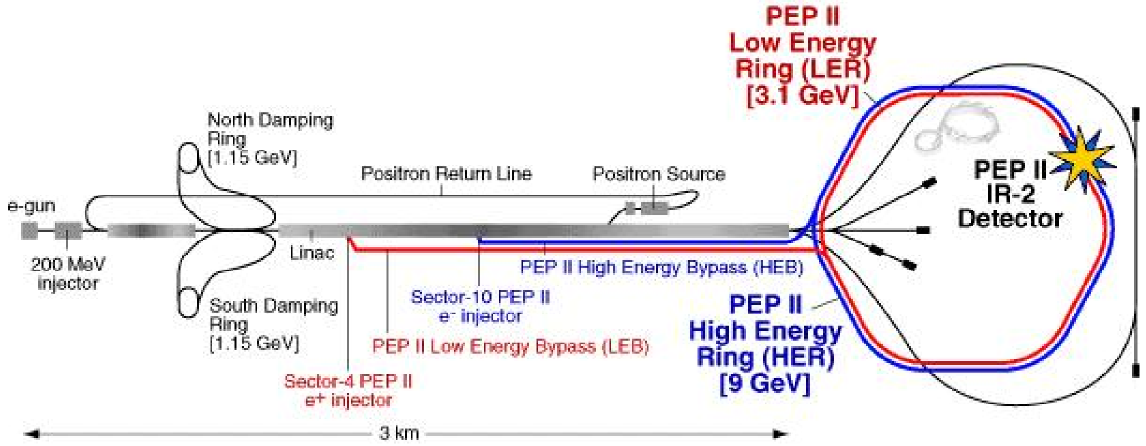

Figure 2.1: PEP-II facility and the linear accelerator layout.

beam is accelerated in the low-energy ring (LER) located on top of the HER. This asymmetric-energy $e^+e^-$ collision results in a Lorentz boost of $\beta\gamma$=0.56 to the $\Upsilon$(4S) resonance in the direction of the electrons. The collision occurs inside the *BABAR* detector. The two beams are brought together for collision in the interaction region, as shown in Figure 2.2. To ensure a head-on collision and a further separation of the beams, bending and focusing magnets are located very close to the interaction point (IP). This is arguably one of the most important and complicated parts of the PEP-II design with a large impact on the *BABAR* detector.

PEP-II is a high-luminosity collider, with the design instantaneous *luminosity* $3\times10^{33}\,\mathrm{cm}^{-2}\mathrm{s}^{-1}$ (see Appendix A), maintaining up to 1658 bunches of electrons and positrons with the bunch spacing of 4.2 ns. The design luminosity was reached in October 2000, and five years later the peak luminosity is $10\times10^{33}\,\mathrm{cm}^{-2}\mathrm{s}^{-1}$. The total integrated luminosity delivered by the PEP-II and recorded by the *BABAR* detector since the beginning of operation in November 1999 is shown in Figure 2.3.

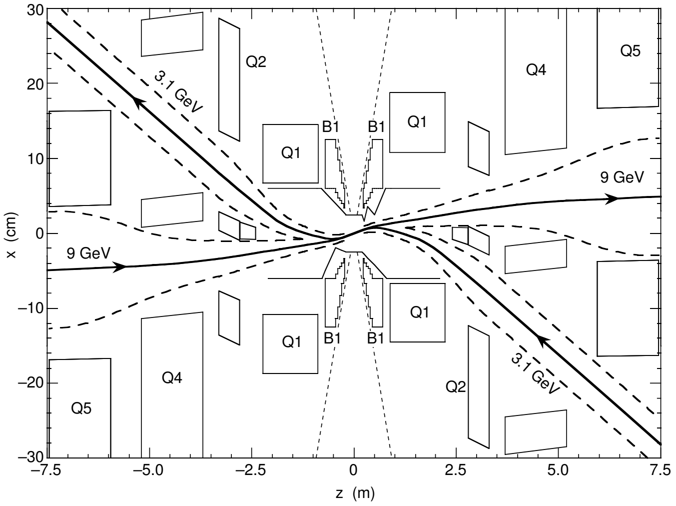

Figure 2.2: PEP-II interaction region where the electron (9 GeV) and positron (3.1 GeV) beams collide inside the *BABAR* detector. Bending ("B") and focusing quadrupole ("QD") magnets are responsible for the head-on collision of the beams.

It is estimated that by 2008 the *BABAR* detector will record up to 1 $\mathrm{ab}^{-1}$ of data. This thesis is based on the recorded data luminosity of 232 $\mathrm{fb}^{-1}$.

## 2.2 The *BABAR* Detector

Most of the particles produced in an $e^+e^-$ collision and used in the studies of the bottom and charm mesons, as well as the $\tau$ leptons, are short-lived and decay very close to the IP. To correctly reconstruct a decay, the particle trajectories and momenta need to be precisely measured. Moreover, accurate particle identification needs to be performed to differentiate between various types of charged tracks and neutrals. All these requirements are met in the *BABAR* detector utilizing the following components:

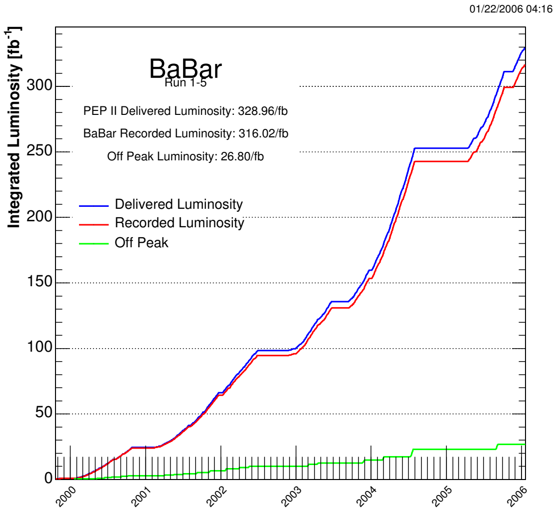

Figure 2.3: Integrated luminosity since 1999 delivered by the PEP-II (blue) and recorded by the *BABAR* detector on the $\Upsilon(4S)$ resonance (red) and 40 MeV below it (green).

- **Silicon Vertex Tracker (SVT)**, located the closest to the interaction point and provides precision measurement of angles and positions of charged tracks.

- **Drift Chamber (DCH)**, determines positions and momenta of charged tracks by their curvature in the magnetic field, as well as identifies charged particles by their ionization trails.

- **Detector of Internally Reflected Cherenkov light (DIRC)**, measures the angle of Cherenkov radiation and indirectly identifies its mass, hence identifying the particle itself.

- **Electromagnetic Calorimeter (EMC)**, measures energies and identifies electrons, positrons and photons.

- **1.5 T Solenoidal Magnet**, provides a 1.5 T magnetic field, which is used in the measurement of a charged particle's momentum.
- **Instrumented Flux Return**, identifies muons and neutral hadrons.

Distribution of material in the various detector systems is shown in Figure 2.4 in units of radiation lengths. The longitudinal and the end views of the *BABAR* detector are shown in Figure 2.5 [22]. The main detector components are described in detail below.

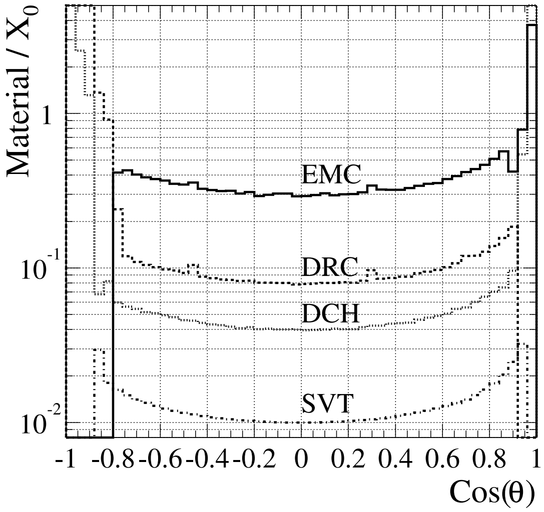

Figure 2.4: Amount of material (in units of radiation lengths) which a particle emerging from the IP with a polar angle $\theta$ passes before it reaches the first active element of a specific detector system.

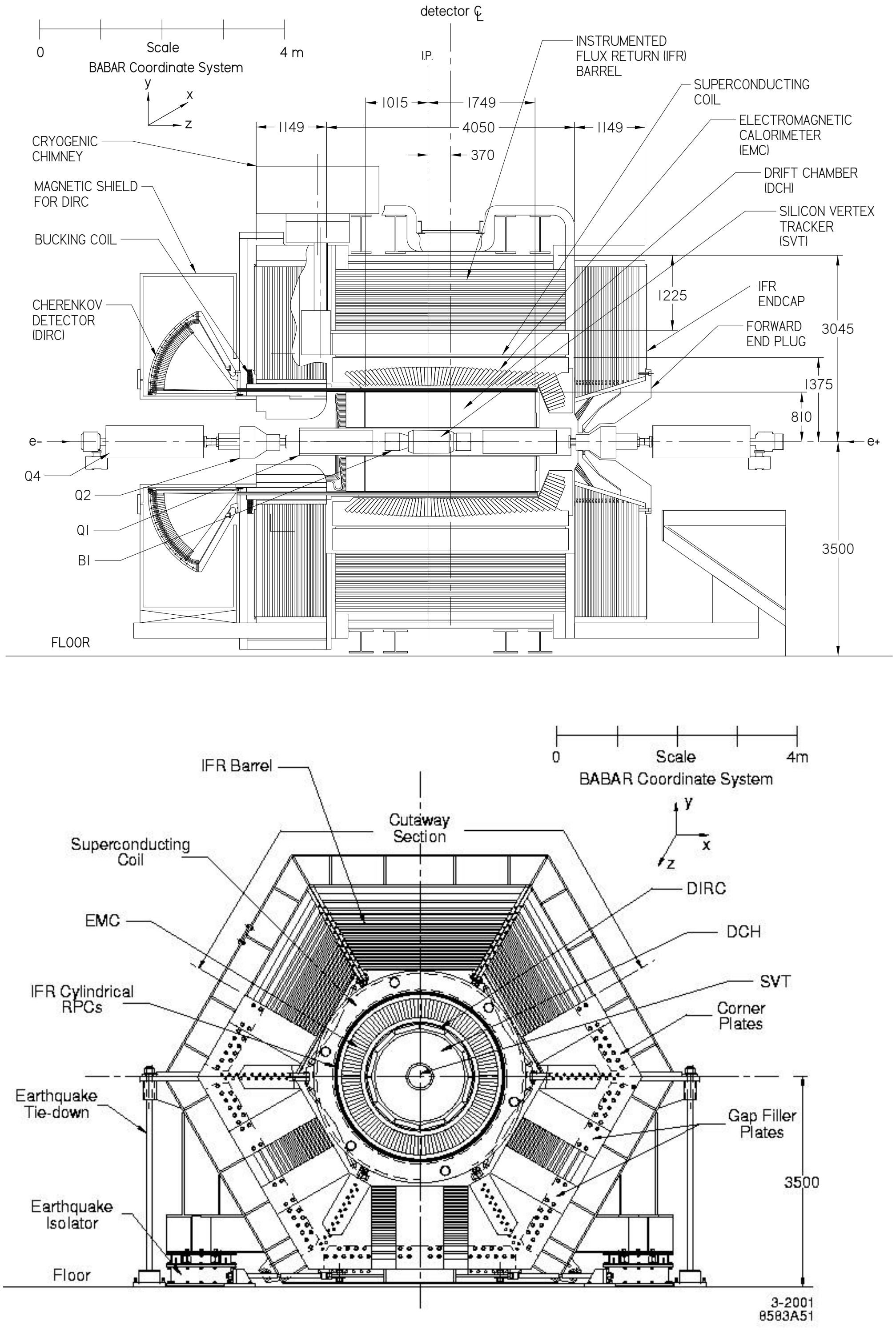

Figure 2.5: The longitudinal section (top) and the end view (bottom) of the *BABAR* detector.

### 2.2.1 Silicon Vertex Tracker

The Silicon Vertex Tracker [22], shown in Figure 2.6, is the closest particle tracking system to the interaction region, located just outside of the 27.8 mm radius beam pipe, and inside the ∼4.5 m-long support tube. It consists of five layers of modules, each containing 300 $\mu$m thick double-sided silicon strip sensors. The innermost three layers with radii of 32, 40 and 54 mm respectively measure the event vertex from the position and angle information of a particle. The remaining two layers are located at larger radii (91-144 mm), and provide accurate tracking information, which links the trajectories to the information from the drift chamber.

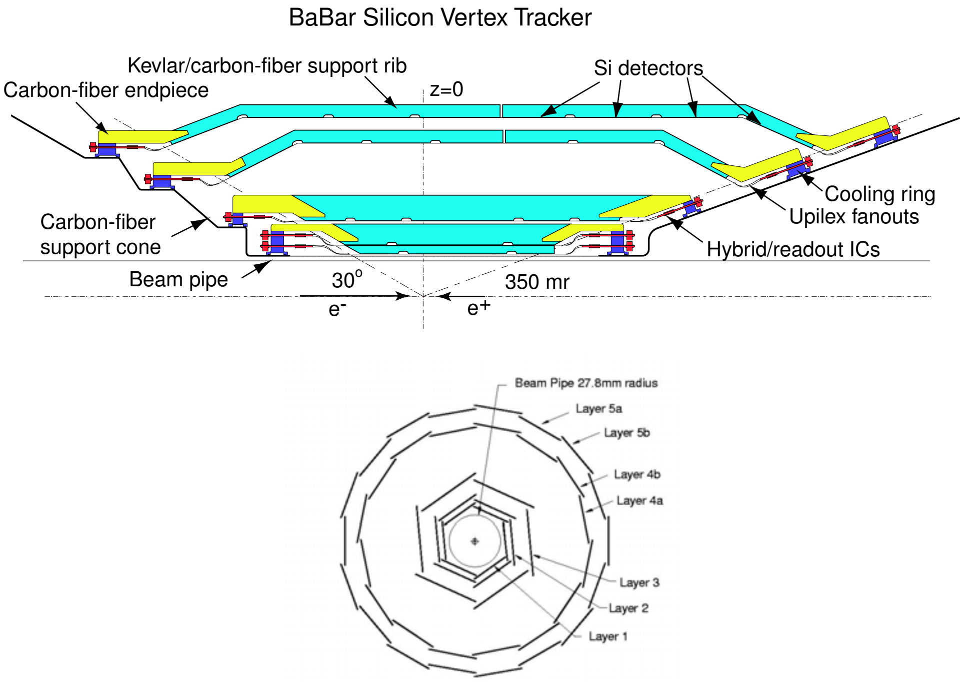

Figure 2.6: The longitudinal section (top) and the transverse view (bottom) of the Silicon Vertex Tracker in the *BABAR* detector.

There are six different types of sensors, varying in size from $43\times42\mathrm{mm}^2$ ($z\times\phi$) to $68\times53\mathrm{mm}^2$. The strips on the opposite sides of each sensor are orthogonal to each other, and are either parallel or perpendicular to the beam axis. The strips that are parallel to the beam axis are called the $\phi$ strips and measure the $\phi$ of the trajectory. Their orthogonal partners are called the $z$ strips and measure the $z$ position of the hit along the beam line. The signals from the strips are brought to the readout electronics. There are ∼150,000 readout channels in the SVT. The vertex resolution is better than 80 $\mu$m along the z-axis, and ∼100 $\mu$m in the plane perpendicular to the beam line.

The SVT is sensitive to tracks with the polar angle between 20° and 150°. For tracks with low transverse momenta ($p_T < 120$ MeV/c) that are not measured by the drift chamber, the SVT serves as a standalone detector. This had an important impact on the SVT design, since the identification of low-$p_T$ tracks is crucial for reconstruction of bottom and charm mesons.

Being so close to the interaction region, the SVT is exposed to 2 Mrad of ionizing radiation over its lifetime. To ensure proper operation of the SVT, radiation-hard electronics is used in the detector.

### 2.2.2 Drift Chamber

The Drift Chamber [22] is the next component of the *BABAR* charge particle tracking system after the SVT. It is located outside of the support tube and provides high precision momentum and angle measurement of charged tracks, as well as ionization information. In the case of the particle originating from the interaction region, the DCH track information is used along with the position and trajectory measurements by the SVT. However, if the track originates outside the SVT as a result of a particle decay, the reconstruction of the primary particle relies solely on the drift chamber. The DCH can also identify the particle by measuring the ionization loss d$E$/d$x$ (see Figure 2.7). This works well in the region $< 1$ GeV/c$^2$.

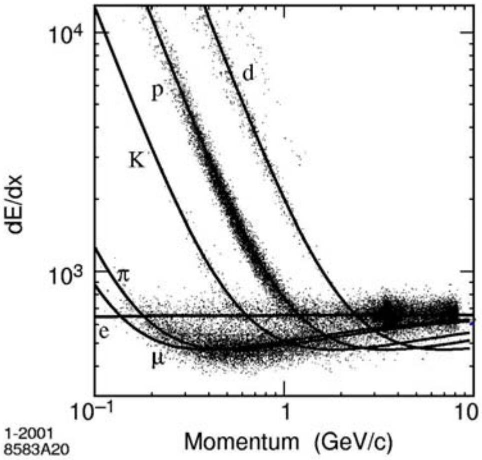

Figure 2.7: Ionization energy loss in the DCH as a function of track momenta. Various types of tracks are identified by the d$E$/d$x$ information, as represented by the curves on the plot.

The drift chamber, a longitudinal view of which is shown in Figure 2.8, is a 280 cm-long cylinder bounded radially by the support tube at its inner radius of 23.6 cm and by the DIRC at its outer radius of 80.9 cm. Because of the asymmetric-energy $e^+e^-$ collisions, the center of the DCH is shifted by 37 cm from the interaction point along the electron beam direction. The DCH has 40 cylindrical layers containing a total of 7104 small hexagonal drift cells with sense wires (see Figure 2.8, right). The tungsten-rhelium sense wires are 20 micron in diameter, with a positive high voltage (1960 V) applied to them. The chamber is filled with a gas mixture: 80% helium and 20% isobutane.

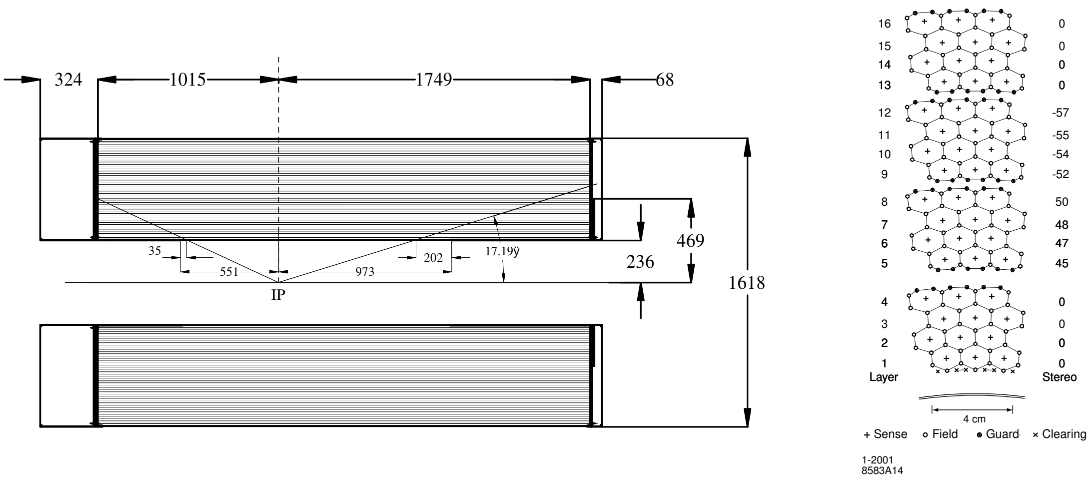

Figure 2.8: The longitudinal section of the DCH (left) and the schematic layout of drift cells for the innermost layers (right).

The reconstruction of a particle's trajectory is based on its ionization trails in the DCH. When a charged particle passes through the chamber it ionizes the gas molecules. The emitted electrons are attracted to the sense wires. While drifting toward the wire, they knock loose more electrons and give a large electronic signal when the cascade of electrons reaches the sense wire. The measurement of the drift time provides the precise position of the track. A track with $p_T > 180$ MeV/c entering the DCH within the polar angle range of $17.2^\circ < \theta < 152.6^\circ$ from the interaction point passes through at least a half of the layers while curving in the magnetic field parallel to the beam axis. The measurement of the curvature provides a precise measurement of the transverse momentum of the particle. Tracking efficiency of the DCH for high-$p_T$ tracks is about 98%. Combined with the SVT, the tracking efficiency is close to 100%.

### 2.2.3 Detector of Internally Reflected Cherenkov Light

The DIRC [22] is a very effective and novel Cherenkov radiation detector. It is located immediately outside of the drift chamber. It provides a precise measurement of the particle's velocity by measuring the angle of *Cherenkov radiation* (see Appendix A). As it is shown in Figure 2.9, a particle that passes through the DCH and enters the DIRC goes through a fused silica bar ($n = 1.473$) and emits Cherenkov light at an angle $cos\theta_c = 1/n\beta$ ($\beta = v/c$). The light is trapped inside the radiator bar by total internal reflection, and propagates to the rear end of the *BABAR* detector emerging into a water-filled expansion region, called the standoff box. The photons are detected by an array of photomultiplier tubes and the Cherenkov angle, and consequently the particle's velocity is measured. Knowing the particle velocity from the DIRC and the momentum from the DCH, it is possible to calculate the mass of the particle, and hence to identify it.

The DIRC is the primary particle identification system in the *BABAR* detector for high-momentum particles with $p > 700$ MeV/c. Low-momentum track identification relies on ionization loss measurements from the DCH. The DIRC can identify five types of particles: $e$, $\mu$, $\pi$, $K$, $p$. One of the crucial tasks of the DIRC is to provide $\pi/K$ separation of $\sim 4\sigma$ or greater. Figure 2.10 shows the reconstruction of a $D^0$ meson decaying into $K\pi$ with and without the DIRC for kaon identification. The difference is obvious: a much cleaner $D^0$ signal is obtained using the DIRC.

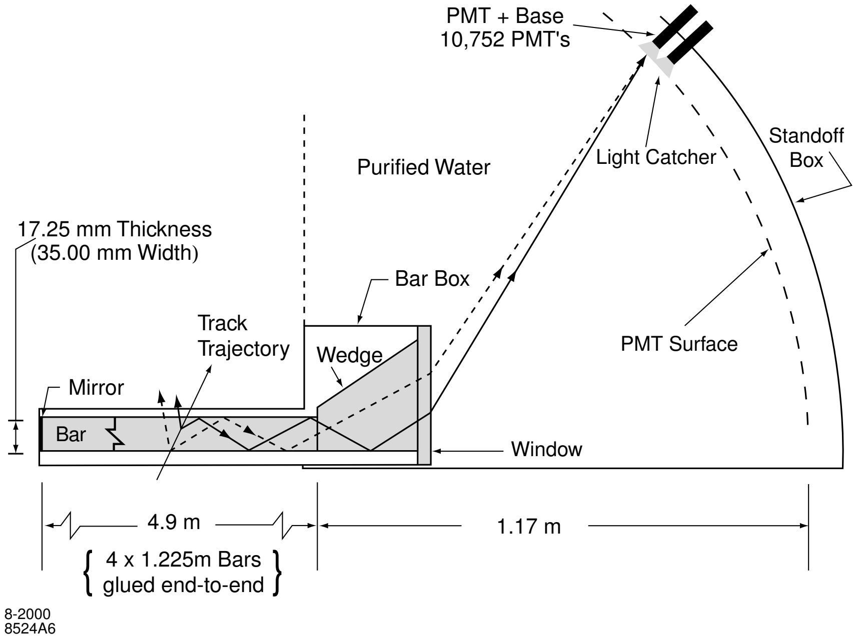

Figure 2.9: Schematics of the DIRC fused silica radiator bar (gray) and imaging region (the PMT Surface and the Standoff Box).

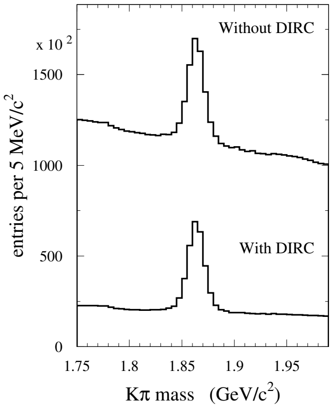

Figure 2.10: Invariant $K\pi$ inclusive mass spectrum with (bottom plot) and without (top plot) the use of the DIRC for kaon identification. The peak in the mass plot corresponds to the $D^0$ meson.

### 2.2.4 Electromagnetic Calorimeter

Both the DCH and DIRC are used to track and identify *charged* particles. Neutral particles are detected by the electromagnetic calorimeter [22], which measures electromagnetic showers with excellent efficiency over a wide energy range from 20 MeV to 9 GeV. The EMC is a hermetic, total-absorption calorimeter, composed of segmented array of 6580 thallium-doped CsI crystals, of which 5880 are located in a cylindrical barrel and 940 are in conical forward endcap (see Figure 2.11).

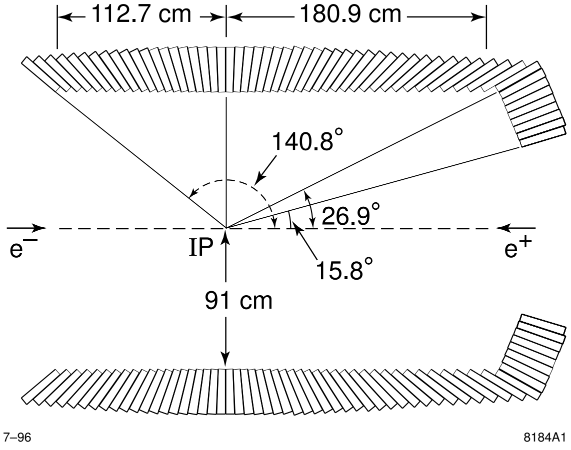

Figure 2.11: Longitudinal cross-section of the EMC.

A particle passing through a crystal produces an electromagnetic shower. The shower is usually scattered over adjacent crystals, forming a cluster of energy deposits. The energy deposited in the crystals is turned into light, which is measured with silicon photodiodes that are matched to the spectrum of the scintillation light. The "primary" crystal in a cluster is required to have an energy of at least 10 MeV. Surrounding crystals absorb as little as 1 MeV. The EMC absorbs the energy of both charged and neutral particles. If the position of the cluster in the EMC is matched with a charged track trajectory the cluster is associated with the charged particle. Otherwise, it is a cluster from a neutral particle. On average, 16 clusters are detected per hadronic event, of which only 6 are associated with charged tracks.

One of the most important functions of the EMC is electron identification. The identification algorithm is based on the shower energy, lateral shower moments and track momentum. In particular, the ratio of the shower energy to the track momentum $E/p$ is usually close to 1 for electrons, and much smaller for hadrons.

### 2.2.5 Instrumented Flux Return

The outermost part of the *BABAR* detector, located just outside of the solenoidal magnet, is the Instrumented Flux Return [22], designed to identify muons and neutral hadrons that penetrate the inner detector and do not get absorbed in the EMC. The IFR, shown in Figure 2.12, consists of a barrel and forward and backward endcaps made of steel. The IFR has 806 resistive plate chambers (RPC) (see Figure 2.12, right), serving as detectors, installed in the spaces between the segmented steel plates. The detection of a particle passing through the IFR is based on the ionization of the gas inside the RPC. The ionization produces a discharge, which is detected by aluminum strip electrodes in the RPC.

Although muons are identified by the IFR, the information from other detector components are crucial for a complete reconstruction of the particle trajectory. The muon candidate in the IFR is required to be reconstructed by the tracking system, and have energy loss consistent with a muon in the EMC.

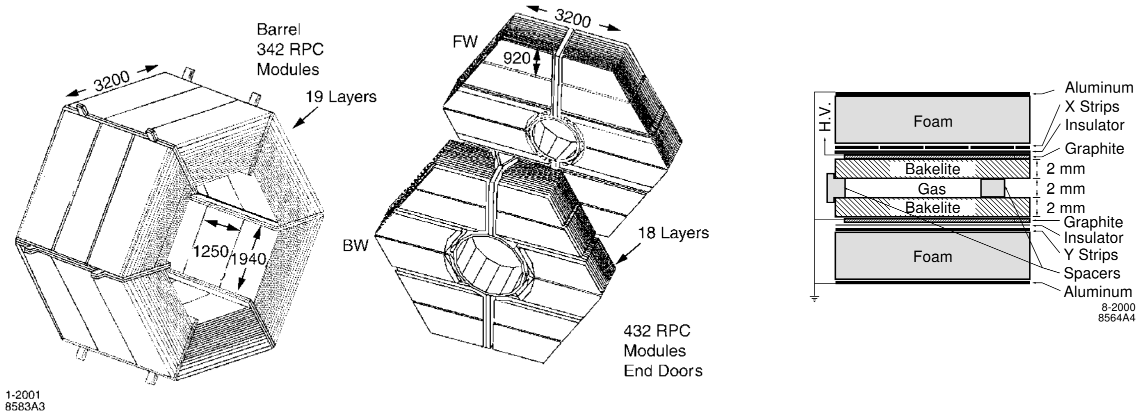

Figure 2.12: Barrel sector (left) and forward (FW) and backward (BW) endcaps, cross-section of the RPC (right).

The IFR covers the polar angle range of $15^\circ < \theta < 157^\circ$. It originally had high efficiency. However, due to radiation related problems the efficiency in large parts of the detector is less than 50%.

### 2.2.6 Trigger

At the *BABAR* design luminosity, event rates are about 20 kHz, from which less than 0.5% are used in physics analyses. Clearly, events need to be filtered before being recorded for further study. The purpose of the trigger system [22] is to reject background and select events of interest with high efficiency. The total event rate is typically under 120 Hz. The trigger efficiency has to be greater than 99% for $e^+e^- \to B\overline{B}$, and greater than 95% for other $e^+e^- \to q\overline{q}$ events. The total trigger efficiency for $e^+e^- \to \tau^+\tau^-$ events used in this analysis is typically in the range of 90-95%, depending on the $\tau$ decay channel.

The trigger system at *BABAR* consists of two levels: Level 1 (L1) hardware and Level 3 (L3) software triggers. The L1 trigger, performing the first stage of the rate reduction, uses raw information from the detector subsystems to select or reject an event. Its decision is based on how well an event was measured in DCH, EMC and IFR. The selection criteria at this trigger level are very loose, and the typical output rate is about 1 kHz with event processing time of about $12\,\mu$s.

The selected events are passed to the L3 trigger, which is the second stage of the event filtering process. It performs track fitting and clustering, selects tracks with higher quality, better information regarding the timing and the $z$ positions of the hits, better defined EMC shower shapes and clusters. Basically, the L3 trigger software comprises event reconstruction and classification. The software runs on the *BABAR* online computer farm.

The L3 trigger output rate is $\sim$90 Hz for events of physics analysis interest, and $\sim$30 Hz for events used in diagnostic and calibration procedures. The event processing time is 8.5 ms on average. Events that pass the trigger system are stored in the database and analyzed by us, the knowledge-hungry physicists. To analyze the data we use ROOT, an object-oriented data analysis framework [23].

# CHAPTER 3

# EVENT SELECTION

## 3.1 Signal and Background

$\tau^+\tau^-$ pairs are produced from $e^+e^-$ collisions in the *BABAR* detector at the center-of-mass energy of 10.58 GeV with a 0.89 nb cross section. Each of the $\tau$ leptons then decays in a very short time period, on average 290 fs (in its rest frame) [6], making it difficult to establish a decay vertex distinguishing a hadronic decay of the $\tau$ lepton from an $e^+e^- \to q\overline{q}$ process. The goal of this analysis is to isolate samples of $\tau^- \to 4\pi^-3\pi^+(\pi^0)\nu_\tau$ and $\tau^- \to 3\pi^-2\pi^+2\pi^0\nu_\tau$ decays, which we call the signal. The invariant mass of signal events is expected to be below the $\tau$ mass of 1.777 GeV/c$^2$ due to the unmeasured neutrino in the decay. The signal in data is established by counting events in the signal region, which is defined as $1.3 < M_\tau < 1.8$ GeV/c$^2$, and subtracting off the number of expected background events in this region.

The background to the signal multi-pion $\tau$ decays comes from hadronization ($e^+e^- \to q\overline{q}$) and $\tau$ migration processes. For the $\tau^- \to 4\pi^-3\pi^+(\pi^0)\nu_\tau$ signal mode, the $\tau$ background stems from the decays $\tau^- \to 3\pi^-2\pi^+\pi^0\nu_\tau$ and $\tau^- \to 2\pi^-\pi^+2\pi^0\nu_\tau$, where the $\pi^0$ mesons decay to $\gamma\gamma$ (in 99% of cases) and the photons undergo conversions in the detector material creating $e^+e^-$ pairs, or a Dalitz decay $\pi^0 \to e^+e^-\gamma$ (1%). The main $\tau$ background to $\tau^- \to 3\pi^-2\pi^+2\pi^0\nu_\tau$ signal decay comes from the $\tau^- \to 3\pi^-2\pi^+\pi^0\nu_\tau$ mode, where one additional (fake) $\pi^0$ is reconstructed, and 3-prong modes with 2 or 3 $\pi^0$'s.

The hadronization process $e^+e^- \to q\overline{q}$ ($q\overline{q}$=$u\overline{u}$,$d\overline{d}$,$c\overline{c}$,$s\overline{s}$) is the major and dominant background for both signal modes. The processes of $e^+e^- \to (u\overline{u}, d\overline{d}, s\overline{s})$ (≡uds) and $e^+e^- \to c\overline{c}$ have different properties and are studied separately.

Properties of signal and background are studied using Monte Carlo (MC) simulation. The event selection criteria were developed to suppress the background from both $q\overline{q}$ and multi-prong $\tau$ events, while maintaining a high signal efficiency level.

## 3.2 Data and Monte Carlo Samples

This analysis is based on data recorded by the *BABAR* detector at the PEP-II asymmetric-energy $e^+e^-$ storage ring operated at the Stanford Linear Accelerator Center. The data sample consists of $L = 232\,\mathrm{fb}^{-1}$ integrated luminosity recorded at $\sqrt{s} = 10.58\,\mathrm{GeV}$ and $10.54\,\mathrm{GeV}$ between 1999 and 2004, and contains $N_{\tau\tau} = L \times \sigma_{\tau\tau} = 2.06 \times 10^8$ $\tau^+\tau^-$ events, which corresponds to over 400 million $\tau$ decays.

For the multi-pion $\tau$ decay signal and background studies Monte Carlo samples are used in this analysis. The KK2F [24] generator is used to create $\tau^+\tau^-$ according to the electroweak interaction. Generic decays of $\tau$ leptons are simulated with the TAUOLA [25] using measured branching ratios for $\tau$ decay modes, which are shown in Table 3.1. The signal decays $\tau^- \to 4\pi^-3\pi^+(\pi^0)\nu_\tau$ and $\tau^- \to 3\pi^-2\pi^+2\pi^0\nu_\tau$ are simulated using phase space with a V-A interaction. Continuum $q\overline{q}$ events are generated using the JetSet package [26]. All Monte Carlo background samples are scaled to the data luminosity according to their production cross sections, shown

| $\tau$ decay mode | Branching ratio | $\tau$ decay mode | Branching ratio |
|---|---|---|---|
| $e\overline{\nu_e}\nu_\tau$ | 0.1781 | $\mu\overline{\nu_\mu}\nu_\tau$ | 0.1737 |
| $\pi\nu_\tau$ | 0.1108 | $\rho\nu_\tau$ | 0.2532 |
| $a1\ \nu_\tau$ | 0.1825 | $K\nu_\tau$ | 0.0071 |
| $K^*\nu_\tau$ | 0.0128 | $2\pi^-\pi^+\pi^0\nu_\tau$ | 0.0450 |
| $\pi^-3\pi^0\nu_\tau$ | 0.0123 | $2\pi^-\pi^+2\pi^0\nu_\tau$ | 0.0050 |
| $3\pi^-2\pi^+\nu_\tau$ | 0.0008 | $3\pi^-2\pi^+\pi^0\nu_\tau$ | 0.0002 |
| $2\pi^-\pi^+3\pi^0\nu_\tau$ | 0.0003 | $K^+K^-\pi^+\nu_\tau$ | 0.0019 |
| $\overline{K^0}K^0\pi^+\nu_\tau$ | 0.0012 | $K^+\overline{K^0}\pi^0\nu_\tau$ | 0.0030 |
| $K^+2\pi^0\nu_\tau$ | 0.0010 | $K^+\pi^-\pi^+\nu_\tau$ | 0.0023 |
| $K^0\pi^0\pi^+\nu_\tau$ | 0.0039 | $\eta\pi^-\pi^0\nu_\tau$ | 0.0017 |
| $\pi^-\pi^0\gamma\nu_\tau$ | 0.0016 | $K^-K^0\gamma\nu_\tau$ | 0.0016 |

Table 3.1: Generic $\tau$ Monte Carlo Branching Ratios implemented in the TAUOLA.

in Table 3.2. Extra samples of $\tau^- \rightarrow 3\pi^-2\pi^+\pi^0\nu_\tau$ and $\tau^- \rightarrow 2\pi^-\pi^+2\pi^0\nu_\tau$ are generated in order to study their impact on our signal modes.

## 3.3 Pre-Selection

Both MC and data samples contain lots of events (see Table 3.2), and therefore some filtering needs to be done, called pre-selection. The pre-selection cuts are loose but efficient, rejecting more than 99.5% of background while retaining ∼30% of the signal.

### 3.3.1 Tau1N Skim

The Tau1N skim was designed for a common use by the Tau Analysis Working Group at *BABAR*. The skim is designed to select $\tau$-pair events classified as 1-N(N≥3) topology. This first part of the pre-selection eliminates more than 90% of the background.

| Mode | Cross section (nb) | Luminosity ($\mathrm{fb}^{-1}$) | Events |
|---|---|---|---|
| Data (on+off peak) | | 232 | $32.8 \times 10^8$ |
| $e^+e^- \to \tau^+\tau^-$ | 0.89 | 459 | $4.1 \times 10^8$ |
| $e^+e^- \to u\overline{u}, d\overline{d}, s\overline{s}$ | 2.09 | 318 | $6.6 \times 10^8$ |
| $e^+e^- \to c\overline{c}$ | 1.30 | 322 | $4.2 \times 10^8$ |
| $e^+e^- \to B^0\overline{B^0}$ | 0.53 | 241 | $1.3 \times 10^8$ |
| $e^+e^- \to B^+B^-$ | 0.53 | 274 | $1.4 \times 10^8$ |
| $\tau^- \to 3\pi^-2\pi^+\pi^0\nu_\tau$ | $\mathcal{B} = 1.8 \times 10^{-4}$ | 1437 | 468000 |
| $\tau^- \to 2\pi^-\pi^+2\pi^0\nu_\tau$ | $\mathcal{B} = 5.0 \times 10^{-3}$ | 216 | 1920000 |
| $\tau^- \to 4\pi^-3\pi^+\nu_\tau$ | phase space | | 240000 |
| $\tau^- \to 4\pi^-3\pi^+\pi^0\nu_\tau$ | phase space | | 240000 |
| $\tau^- \to 3\pi^-2\pi^+2\pi^0\nu_\tau$ | phase space | | 480000 |

Table 3.2: Data and Monte Carlo samples used in this analysis.

The overall multiplicity is required to be >2 and ≤10 charged tracks in the event. Next, the event is divided into two hemispheres based on the plane perpendicular to the thrust axis. The thrust [26] is defined by

$$T = \max_{|\mathbf{n}|=1} \frac{\sum_i |\mathbf{n} \cdot \mathbf{p}_i|}{\sum_i |\mathbf{p}_i|} \tag{3.1}$$

where $\mathbf{n}$ is a unit vector. By definition, the thrust axis is chosen to minimize the sum of transverse momenta of all particles in an event, where momenta is taken with respect to this axis. The thrust is calculated in the center of mass system using all charged tracks and neutrals in the event. The number of neutrals (with energy > 50 MeV) in each hemisphere is required to be less than or equal to 6, to keep up to $3\pi^0$'s from each $\tau$ decay. The number of tracks in each hemisphere is used to determine the topology of the event. Good tracks from the interaction region are required to have a distance of closest approach in the transverse plane to the beam axis ($\mathrm{DOCA}_{XY}$) of not more than 1.5 cm and an absolute value of the distance of closest approach in the $z$-direction smaller than 10 cm. These tracks belong to the *GoodTracksVeryLoose* (GTVL) list. The topology definition is based on the number of GTVL tracks: the Tau1N skim requires 1 GTVL in one hemisphere, recoiling against N≥3 GTVL in the other hemisphere. Also, the combined mass of all tracks and neutrals is required to be less than 3 GeV/$c^2$ per hemisphere.

Additional pre-selection criteria include cuts on the second Fox-Wolfram moment, energy deposited in the EMC, missing mass in the event. These are designed to reduce background from $B\overline{B}$, Bhabha and 2-photon processes.

Based on the skimmed events, a refined pre-selection, specific for this analysis, is performed.

### 3.3.2 Photon Conversion Rejection

Charged tracks from photon conversions in generic $\tau$ decays contribute to an increased multiplicity of the event and therefore contribute to the number of selected signal candidate events. The standard *BABAR* conversion finder tries to combine pairs of oppositely charged tracks to a common vertex. Due to their nature these tracks are nearly parallel at the photon conversion point. In order for an event to be retained in this analysis we demand the distance in X and Y between two tracks at point of closest approach to be larger than 0.2 cm and the invariant mass calculated from these two tracks to be larger than 5 MeV/$c^2$. Though these cuts clean up the event sample considerably we had to develop more stringent cuts to suppress the background from the converted photons to acceptable levels (see section 3.6).

### 3.3.3 Looper Rejection

In the multi-hadron events low-momentum tracks with $\theta_{lab} \simeq \pi/2$ can pass through the interaction region multiple times and result in copies of the initial track with similar momenta. These tracks are called "loopers" (see Figure 3.1). A pair of tracks satisfying following requirements is considered a looper candidate:

- both tracks have SVT hits
- $p_{t,lab} < 0.2$ GeV/c for each track
- $|\cos\theta_{lab}| < 0.18$ for each track
- $|\Delta p_{t,lab}| = |p^i_{t,lab} - p^j_{t,lab}| < 0.1$ GeV/c

It is important not to reject the primary looper track, but the "fake" duplicate tracks. From the list of the looper candidate tracks we keep the track with the smallest distance of closest approach to the beamspot along the Z-axis, considering it to be the primary track.

The looper rejection criteria reduce the background from loopers by almost 90%, while the signal rejection rate is negligibly low.

### 3.3.4 Charged Track Candidates

Out of the 1-N topology events passing the Tau1N skim, we select the ones with $N = 5(7)$ GTVL for the $\tau^- \to 3\pi^-2\pi^+2\pi^0\nu_\tau$ ($\tau^- \to 4\pi^-3\pi^+(\pi^0)\nu_\tau$) search. In addition to the 6(8) GTVL tracks in an event, a minimum 4(6) of these 6(8) tracks are required to have at least 12 drift chamber hits and a minimum transverse momentum of 100 MeV/c. Such tracks belong to the *GoodTrackLoose* (GTL) list.

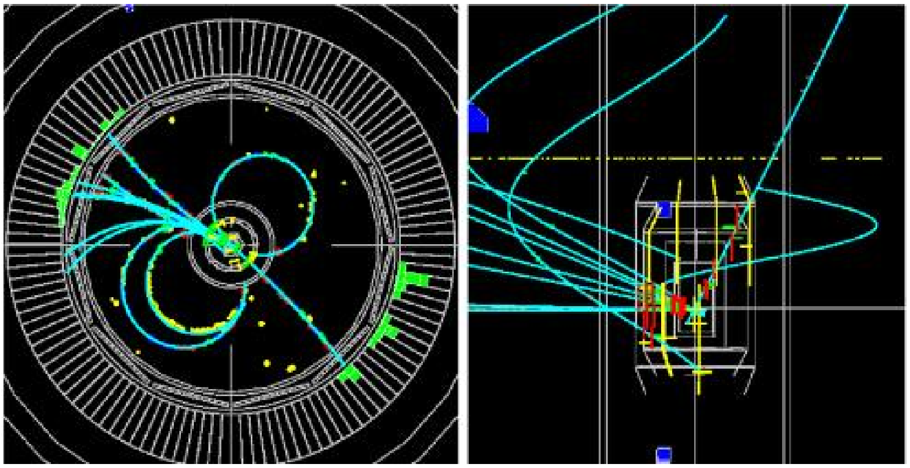

Figure 3.1: A *BABAR* detector display of an event with a looper. Left plot: the r-$\phi$ plane; Right plot: the r-z plane.

The track on the tag side is required to be a GTL. The net charge of the event has to be zero.

A graphical example of a 1-7 topology event is shown in figure 3.2. In this typical scenario of a 7-prong $\tau$ decay simulated by Monte Carlo, 8 tracks have been reconstructed on the 7-prong side, but only 7 are selected, since one of the tracks evidently does not come from the $e^+e^-$ interaction point (see the right plot in Figure 3.2) and therefore does not pass the *GoodTracksVeryLoose* criteria.

### 3.3.5 Photon Candidates

In the *BABAR* framework, the default neutrals are candidates from the *CalorNeutral* list. This list includes EMC bumps not associated with a charged track, with photon mass hypothesis assigned. It is a very loose list, with lots of "fake" photons

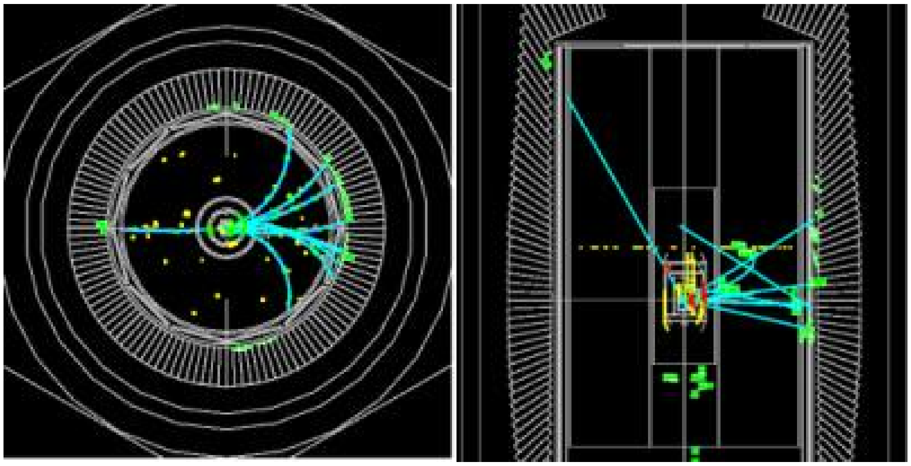

Figure 3.2: Monte Carlo simulated 1-7 topology event demonstration by the *BABAR* Event Display package. Left plot: Front view; Right plot: Top view.

according to MC truth information. In order to discriminate against noise and background from backscattering in the calorimeter we demand in $\tau^- \to 3\pi^- 2\pi^+ 2\pi^0 \nu_\tau$ ($\tau^- \to 4\pi^- 3\pi^+ (\pi^0) \nu_\tau$) analysis:

- $\mathrm{E}_{cluster} > 50\,\mathrm{MeV}$ ($> 70\,\mathrm{MeV}$)
- number of crystal hits $> 2$ ($> 3$)
- lateral energy distribution (LAT) $< 0.6$ ($< 0.8$) (see Appendix A)
- $\Delta\alpha > 0.08$ radians (no cut)

where $\Delta\alpha$ is a 3-d angle between the positions of the cluster and the impact point of the nearest charged track at the EMC surface given by

$$\Delta\alpha = \cos^{-1}[\cos\theta_{cluster}\cos\theta_{track} + \sin\theta_{cluster}\sin\theta_{track}\cos(\phi_{cluster} - \phi_{track})]. \quad (3.2)$$

Figure 3.3 compares the distinctive cut quantities of true and fake photons in the signal MC sample after the pre-selection cuts. The purity of the selected photons, defined as the ratio between the number of true photons and the total number of photons in the signal MC sample, is 86% for the $\tau^- \rightarrow 3\pi^-2\pi^+2\pi^0\nu_\tau$ analysis, and 75% for the $\tau^- \rightarrow 4\pi^-3\pi^+(\pi^0)\nu_\tau$ analysis. The efficiency of this selection in the signal, defined as $N_\gamma^{selected}/N_\gamma^{total}$, equals 87% for the $\tau^- \rightarrow 3\pi^-2\pi^+2\pi^0\nu_\tau$, and 80% for the $\tau^- \rightarrow 4\pi^-3\pi^+(\pi^0)\nu_\tau$ analysis.

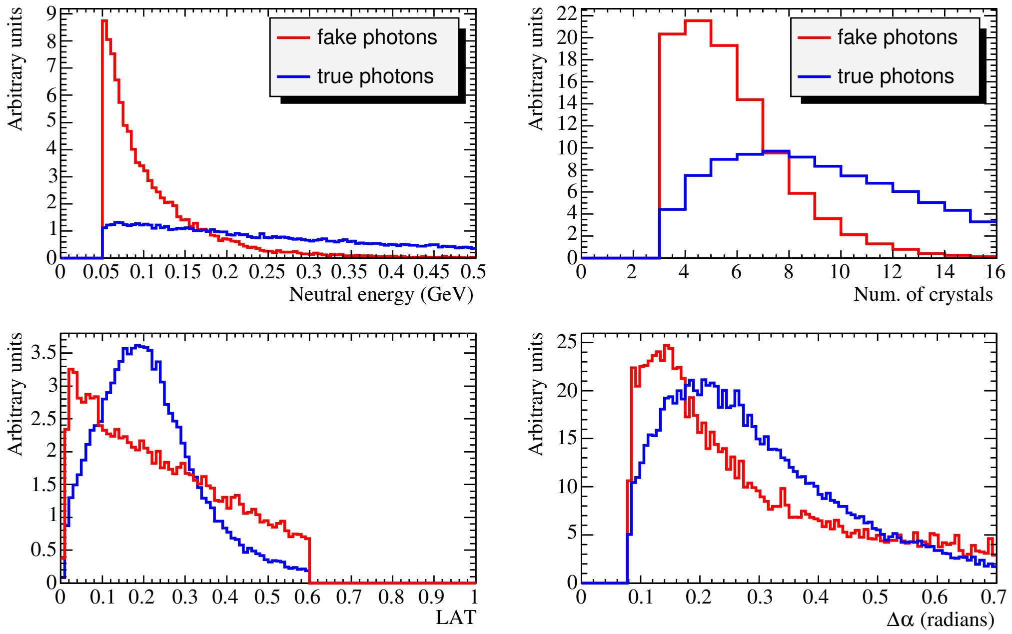

Figure 3.3: Distinction between MC true and fake photons by cluster energy, crystal hits, LAT moment and the angle between the photons and the closest track. All distributions are normalized to unit area ×100.

### 3.3.6 Event Thrust Magnitude

One of the most efficient quantities to discriminate $q\overline{q}$ background from the signal is the event thrust magnitude. It varies from 0.5 for isotropic events to 1.0 for back-to-back events. Since $e^+e^- \rightarrow q\overline{q}$ events are more isotropic that $e^+e^- \rightarrow \tau^+\tau^-$, we demand the event thrust magnitude to be larger than 0.9 to select $\tau$-like events. This cut reduces the background from $q\overline{q}$ events by more than 90%. In particular, the background from $B\overline{B}$ events is suppressed to a negligible level after the thrust cut. The thrust magnitude for signal and background events is shown in Figure 3.4.

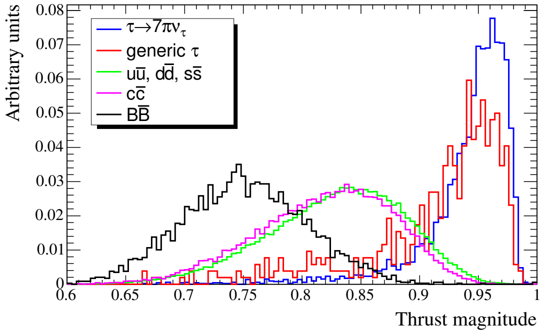

Figure 3.4: Thrust magnitude of the event after the topology selection for Monte Carlo samples of the 7-prong signal (blue), bkg. from generic $\tau$ events (red), uds (green), $c\overline{c}$ (magenta) and $B\overline{B}$ (black).

### 3.3.7 Pre-selection Efficiency

The efficiencies of the pre-selection cuts are shown in Table 3.3. Only contributing backgrounds are shown in the table. The background to the 5-prong signal events is suppressed by more than 99.8%, while the background to the 7-prong events is suppressed by more than 99.99%. However, the background level is still quite high after the cuts. Therefore, additional selection criteria are applied to suppress the remaining background for both topologies.

| Cuts | generic $\tau$ (%) | $uds$ (%) | $c\overline{c}$ (%) | $B\overline{B}$ (%) | $\tau^- \rightarrow 4\pi^-3\pi^+(\pi^0)\nu_\tau$ | $\tau^- \rightarrow 3\pi^-2\pi^+2\pi^0\nu_\tau$ |
|---|---|---|---|---|---|---|
| **Tau1N skim** | | | | | | |
| Trigger | 83.8 | 95.9 | 99.0 | 99.9 | 92.3 | 91.0 |
| Track multiplicity | 68.1 | 78.3 | 72.8 | 46.9 | 79.9 | 85.8 |
| Neutrals multiplicity | 67.9 | 66.4 | 55.7 | 29.3 | 79.8 | 85.1 |
| Topology 1-N (N$\geq$3) | 16.0 | 6.1 | 4.3 | 0.7 | 58.7 | 63.5 |
| **Track and Neutral Quality** | | | | | | |
| Topology 1-5 | 0.2 | 2.3 | 1.8 | 0.3 | | 33.3 |
| Topology 1-7 | 0.0009 | 0.11 | 0.10 | 0.03 | 25.8 | |
| **Thrust Magnitude** | | | | | | |
| Topology 1-5 | 0.13 | 0.21 | 0.10 | 0.001 | | 30.1 |
| Topology 1-7 | 0.0006 | 0.01 | 0.006 | 0.0001 | 22.9 | |
| **Num. evts. in 232 fb$^{-1}$** | | | | | | |
| Topology 1-5 | 536848 | 1018248 | 301600 | 2436 | | |
| Topology 1-7 | 1151 | 48488 | 18096 | 244 | | |

Table 3.3: Efficiency (%) of the Monte Carlo samples after each pre-selection cut. The cuts are multiplicative. The track quality cuts include the looper and the conversion rejection criteria.

## 3.4 Additional Pre-selection Criteria for the $\tau^- \rightarrow 3\pi^-2\pi^+2\pi^0\nu_\tau$ Analysis

### 3.4.1 Reconstruction of $\pi^0$

For the $\tau^- \rightarrow 3\pi^-2\pi^+2\pi^0\nu_\tau$ analysis, correct reconstruction of the $\pi^0$ mesons is crucial for the background suppression. In the *BABAR* framework, a $\pi^0$ is reconstructed from 2 photon candidates, neutral clusters with $E_{cluster} > 30$ MeV and LAT<0.8.

Depending on the reconstructed invariant mass of the photon candidates, $\pi^0$'s are sorted into different lists. We start out with the *pi0Loose* list, which only contains $\pi^0$ candidates with $100 < M_{\gamma\gamma} < 160$ MeV and $E_{\gamma\gamma} > 200$ MeV. We then create a sublist of $\pi^0$'s, suitable for this analysis. The following requirements must be met for a sublist $\pi^0$:

- daughters of the $\pi^0$ must pass the photon selection criteria 3.3.5,
- $E_{\pi^0} > 300$ MeV,
- high energy $\pi^0$'s ($E_{\pi^0} > 450$ MeV) are selected first within the mass range of $113 < M_{\gamma\gamma} < 155$ MeV/c$^2$ (the $3\sigma$ limit of the $\pi^0$ distribution),
- the rest of the $\pi^0$'s are selected within the mass range of $120 < M_{\gamma\gamma} < 148$ MeV/c$^2$ (the $2\sigma$ limit of the $\pi^0$ distribution),
- combinatorial background is removed by keeping the $\pi^0$'s with the smallest $|M_{\gamma\gamma} - M_{\pi^0}|$.

Cutting on the $\pi^0$ energy ensures higher purity of the $\pi^0$ selection.

Figure 3.5 shows the mass spectra of the *pi0Loose* and the sublist $\pi^0$'s that pass the above criteria. Figure 3.6 shows the mass spectrum of all reconstructed $\pi^0$'s in the $\tau^- \to 3\pi^- 2\pi^+ 2\pi^0 \nu_\tau$ sample (top plot), and the mass spectrum of only 2 selected $\pi^0$'s (bottom plot). The purity of the final selection with 2 reconstructed $\pi^0$'s is 80.3%, while the efficiency is 13.0%.

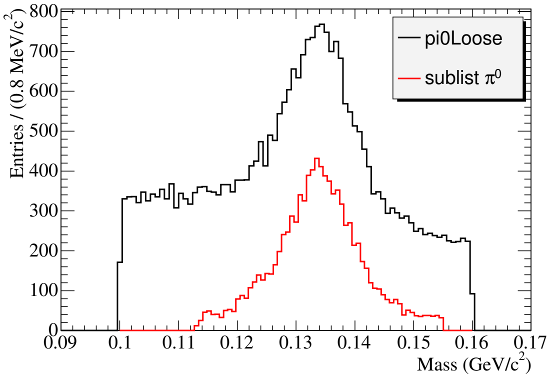

Figure 3.5: Mass spectra of pi0Loose and sublist $\pi^0$'s in the signal MC.

### 3.4.2 Visible Energy

Since the $\tau$ events are always accompanied by at least 1 neutrino in each hemisphere, the visible energy, defined as the CM energy of the charged tracks plus reconstructed $\pi^0$'s, has to be less than the CM beam energy of 5.29 GeV in each hemisphere. This requirement reduces background from $q\overline{q}$ events. It is also quite efficient against $\tau^- \to 3\pi^- 2\pi^+ \pi^0 \nu_\tau$ events that include an additional fake $\pi^0$ for the visible energy calculation in the signal hemisphere. Figure 3.7 shows visible energy distributions for signal, $q\overline{q}$ and $\tau^- \to 3\pi^- 2\pi^+ \pi^0 \nu_\tau$ events on the signal side.

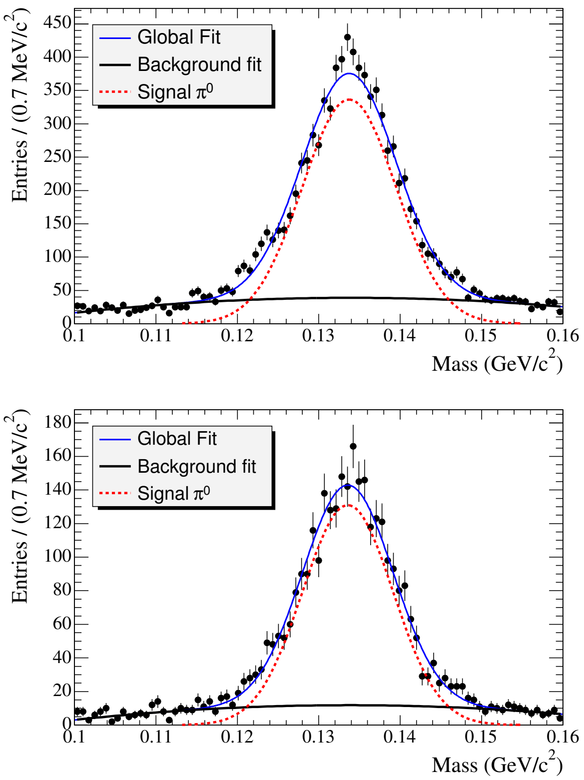

Figure 3.6: Mass spectrum of all sublist $\pi^0$'s (top plot) and exactly 2 selected $\pi^0$'s (bottom plot) in the $\tau^- \to 3\pi^- 2\pi^+ 2\pi^0 \nu_\tau$ MC sample. $\pi^0$'s with masses outside the [113, 155] MeV region are plotted for background estimate only, and are not included in the sublist of reconstructed $\pi^0$'s.

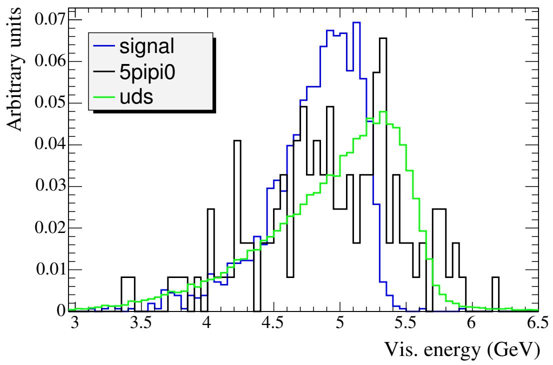

Figure 3.7: Visible energy distributions for MC signal, $q\overline{q}$ and $\tau^- \to 3\pi^- 2\pi^+ \pi^0 \nu_\tau$ events on the signal side. All distributions are normalized to unit area.

### 3.4.3 Residual Neutral Energy on the Signal Side

When the $\tau^- \rightarrow 3\pi^-2\pi^+2\pi^0\nu_\tau$ events are reconstructed, there should be no or very little neutral energy left unaccounted for on the signal side. On the other hand, $q\overline{q}$ events can contain a lot more neutrals that were left out of the $\pi^0$ reconstruction. Also, $\tau^- \rightarrow 2\pi^-\pi^+3\pi^0\nu_\tau$ events have a relatively large branching fraction and contribute significantly to the background. Requiring the residual neutral energy on the signal side be less than 300 MeV helps reduce this background.

### 3.4.4 Efficiency of Additional Pre-Selection

The efficiency of the pre-selection cuts are shown in Table 3.4. The contamination from $B\overline{B}$ events is negligible compared to $uds$ and $c\overline{c}$ backgrounds and generally have an invariant mass much larger than $M_\tau$. Therefore $B\overline{B}$ events will be omitted from further discussions.

| Cuts | gen.$\tau$(%) | $uds$(%) | $c\overline{c}$(%) | $B\overline{B}$(%) | signal(%) |
|---|---|---|---|---|---|
| General pre-selection | 0.13 | 0.21 | 0.10 | 0.001 | 30.1 |
| Reconstruction of 2 $\pi^0$'s | $6.7\times10^{-4}$ | $9.7\times10^{-3}$ | $4.8\times10^{-3}$ | $2.8\times10^{-5}$ | 3.9 |
| Visible and residual neutral energy cuts | $4.5\times10^{-4}$ | $4.2\times10^{-3}$ | $2.7\times10^{-3}$ | $1.9\times10^{-5}$ | 3.5 |
| Num. evts. in 232 $\text{fb}^{-1}$ | 941 | 20979 | 8380 | 48 | |

Table 3.4: Pre-selection efficiency (%) of the Monte Carlo samples for the $\tau^- \rightarrow 3\pi^-2\pi^+2\pi^0\nu_\tau$ analysis. The final number of background events after the pre-selection is normalized to 232 $\text{fb}^{-1}$ for each MC background sample.

## 3.5 Invariant and Pseudo Mass of the $\tau$

The key variable for reconstructing a signal $\tau$ event is the invariant mass of the $\tau$ decay products. The signal is expected to peak slightly below the $\tau$ mass of 1.777 GeV/c$^2$ due to the undetected neutrino. The background from generic $\tau$ events is expected to peak around the $\tau$-lepton mass, but has a very wide mass spectrum varying between 1.3 and 2.5 GeV/c$^2$. Tau events with masses above the $\tau$ mass are due to the photon conversions that are reconstructed as charged tracks with a pion mass hypothesis, and/or $\pi^0$'s included in the mass calculation. For example, the $\tau^- \rightarrow 3\pi^-2\pi^+\pi^0\nu_\tau$ mode is the dominant $\tau$ background for both $\tau^- \rightarrow 4\pi^-3\pi^+(\pi^0)\nu_\tau$ and $\tau^- \rightarrow 3\pi^-2\pi^+2\pi^0\nu_\tau$ modes. In the first case, the background comes from photon conversion daughters ($e^+e^-$ pair) identified as charged tracks with pion mass hypothesis. Hence, the invariant mass of these seven tracks can be larger than the $\tau$ mass of 1.777 GeV/c$^2$. In the second case, a fake $\pi^0$ is picked up, and the invariant mass can again be larger than the $\tau$ mass.

Hadronic $q\overline{q}$ events typically have an invariant mass larger than the $\tau$ mass, which ultimately makes them easier to distinguish from the signal events. But there are 30-50 times more of these events than the $\tau$ background (after pre-selection), which makes them the dominant background in the signal region.

If the $\tau$ neutrino is assumed to be massless and the $\tau$-lepton direction is approximated by the vector momentum of the charged tracks and reconstructed $\pi^0$'s, the following variable can approximate the invariant mass (see Appendix B):

$$m_\tau^{*2} = 2(E_{beam} - E_{7h})(E_{7h} - P_{7h}) + m_{7h}^2 \tag{3.3}$$

where $E_{beam}$ is the beam energy in the CM frame, and $E_{7h}$, $P_{7h}$ and $m_{7h}$ are energy, momentum and the invariant mass of the 7 hadrons in the CM frame, respectively. This variable is called the $\tau$ pseudo mass [27]. The approximation of the neutrino direction is justifiable for 7-hadron $\tau$ decays. The invariant and pseudo-mass distributions are shown in Figure 3.8 for signal and background. The factor $E_{beam} - E_{7h}$ in Equation 3.3 is the smallest for the signal, and the highest for the $q\overline{q}$ background, making the signal-background separation significantly larger. The pseudo-mass spectrum of signal events has a sharp cut-off at the $\tau$ mass. The signal region defined for the invariant mass scale is the same for the pseudo mass scale, and is between 1.3 and 1.8 GeV/c$^2$. The $\tau$ pseudo mass will be used to identify signal events. The $\tau$ pseudo-mass calculation is based on seven charged tracks for $\tau^- \to 4\pi^-3\pi^+(\pi^0)\nu_\tau$, and five tracks and two reconstructed $\pi^0$s for $\tau^- \to 3\pi^-2\pi^+2\pi^0\nu_\tau$ analyses.

Full pseudo-mass spectra for MC background samples are shown in Figure 3.9 for the $\tau^- \to 3\pi^-2\pi^+2\pi^0\nu_\tau$ analysis. The main components of the $q\overline{q}$ background, *uds* and $c\overline{c}$, are shown separately. The $\tau$ background consists of 1-, 3- and 5-prong events. Tau modes with the biggest contribution to the background are also shown. After the pre-selection, the $\tau$ background is dominated by the 3-prong modes, which are suppressed after particle identification (ID) and conversion veto requirements, described in chapter 3.6. The hardest-to-suppress $\tau$ background for both $\tau^- \to 3\pi^-2\pi^+2\pi^0\nu_\tau$ and $\tau^- \to 4\pi^-3\pi^+(\pi^0)\nu_\tau$ studies comes from the $\tau^- \to 3\pi^-2\pi^+\pi^0\nu_\tau$ mode, which becomes the dominant $\tau$ background after all cuts.

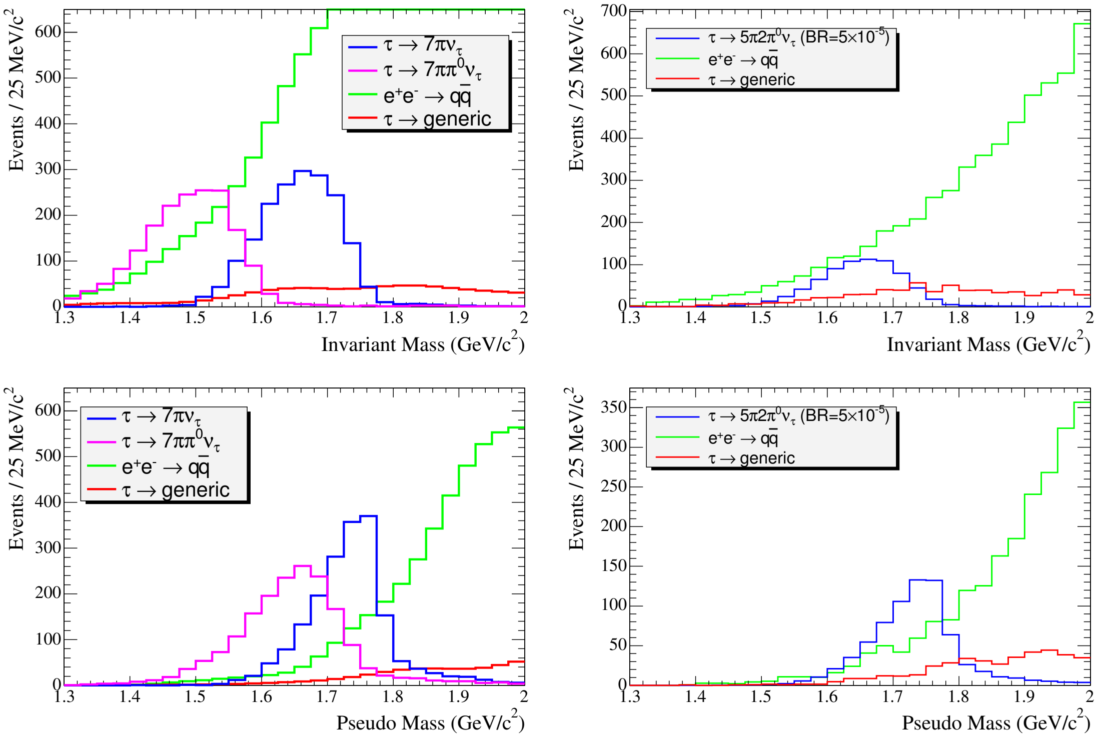

Figure 3.8: Invariant mass (top plots) and pseudo-mass (bottom plots) distributions shown for signal and background MC samples. Left plots: $\tau^- \to 4\pi^-3\pi^+(\pi^0)\nu_\tau$ analysis; Right plots: $\tau^- \to 3\pi^-2\pi^+2\pi^0\nu_\tau$ analysis.

## 3.6 Background Suppression

Although the pre-selection rejects 99.9% of the background, it is far from sufficient to extract a signal with a very low branching ratio. To suppress the remaining background, further cuts are applied on variables selected based upon how well they distinguish between the signal and background. Some cuts and variables are different for the $\tau^- \to 4\pi^-3\pi^+(\pi^0)\nu_\tau$ and $\tau^- \to 3\pi^-2\pi^+2\pi^0\nu_\tau$ analyses. Each cut is described below.

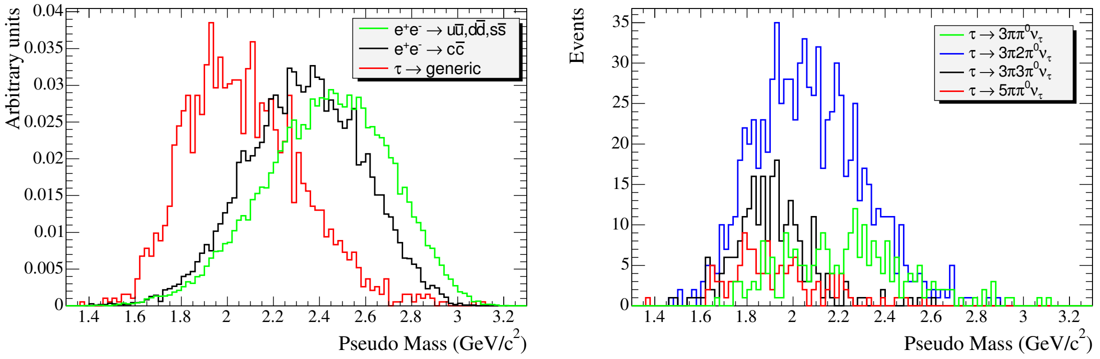

Figure 3.9: Left plot: Pseudo-mass distributions of generic $\tau$, $uds$ and $c\bar{c}$ background MC samples normalized to unit area. Right plot: Signal-side pseudo-mass distribution of the most contributing MC $\tau$ background modes after the pre-selection.

### 3.6.1 Particle ID on the Signal Side

Particle ID information on the signal side is used in both 7-prong and 5-prong analyses to reject the background from $\tau$ events contributing through photon conversions. These events will generally have an $e^+e^-$ pair on the signal side. To reject them, we use a standard *BABAR* pion likelihood selector (see Appendix A) with tight and loose criteria: all charged tracks on the signal side have to satisfy the tight pion likelihood criteria, except for one that has to fulfill at least the loose criteria. Allowing one track to be only loosely identified as a pion gives satisfactory background reduction, while keeping the signal efficiency reasonably high. Also, a fairly large number of kaons are expected from the $q\bar{q}$ events, especially from $c\bar{c}$.

### 3.6.2 Photon Conversion Veto on the Signal Side

To further discriminate against the $\tau$ background events with photon conversions and remaining loopers, we develop criteria vetoing conversions based on the information on track's transverse momentum and a distance of the closest approach (DOCA) to the beamspot. Typically, charged tracks from photon conversions have larger DOCA and lower than average $p_t$. Figure 3.10 (top plots) shows the track $p_t$ (left plot) and $DOCA_{XY}$ (right plot) distributions for the 5-prong signal and 3-prong $\tau$ background samples. Notice that the majority of the low-$p_t$ and large $DOCA_{XY}$ tracks in the 3-prong background events are fake pions (dashed distribution in the plots). Since the 3-prong background events need 2 fake pions to fake the signal, both of them are likely to have low $p_t$'s and large $DOCA_{XY}$'s. Variables $p_t^{lowest1} + p_t^{lowest2}$ and $DOCA_{XY}^{largest1} + DOCA_{XY}^{largest2}$ are shown Figure 3.10 (bottom plots). To veto the photon conversions and low quality tracks, we apply the following criteria in the $\tau^- \to 3\pi^- 2\pi^+ 2\pi^0 \nu_\tau$ analysis:

- $p_t \ > \ 0.1$ GeV/c for each track
- $p_t^{lowest1} + p_t^{lowest2} \ > \ 0.4$ GeV/c for each event
- $DOCA_{XY}^{largest1} + DOCA_{XY}^{largest2} \ < \ 0.4$ cm for each event

In the $\tau^- \to 4\pi^- 3\pi^+ (\pi^0) \nu_\tau$ analysis, a slightly different approach is used for conversion veto: a variable $DOCA_{XY}/p_t$ is required to be less than 0.7 cm×c/GeV for each track, provided the $p_t \ > \ 0.1$ GeV/c cut is already applied. The advantage of this variable is that it uses the correlation information between the transverse momentum of the tracks and their DOCA. This makes the cut more efficient than cuts applied on these two variables separately.

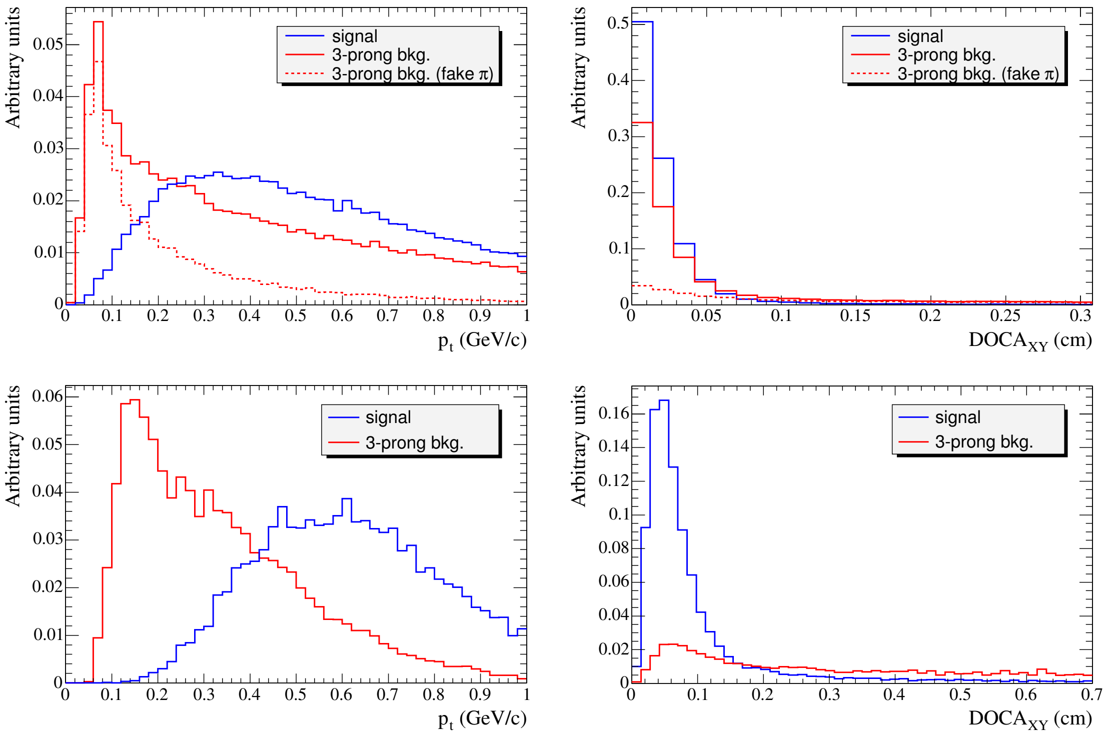

Figure 3.10: $p_t$ (left upper plot) and $DOCA_{XY}$ (right upper plot) distributions of the signal-side tracks for signal and 3-prong background MC samples. The dashed line represents tracks not matched to the true pions. The $p_t^{lowest1} + p_t^{lowest2}$ (left bottom plot) and $DOCA_{XY}^{largest1} + DOCA_{XY}^{largest2}$ (right bottom plot) distributions of the signal-side tracks for signal and 3-prong background MC samples after the pre-selection. Signal and 3-prong $\tau$ background distributions are normalized to unit area.

### 3.6.3 Tagging the 1-prong Side

Information on the 1-prong (tag) side is used to reject the $q\overline{q}$ background. Since leptons are not expected in $e^+e^- \rightarrow q\overline{q}$ processes, requiring a lepton on the tag side effectively rejects this background. In addition, $q\overline{q}$ events typically have higher photon multiplicity, and cutting on the number of photons on the tag side also helps to suppress the background. Table 3.5 shows different 1-prong tag efficiencies for $\tau^- \rightarrow 3\pi^-2\pi^+2\pi^0\nu_\tau$ signal and background samples. Each tag consists of an identified lepton ($e$ or $\mu$), hadron (pion or kaon), $\rho$-meson and an allowed number of photons on the tag side. Lepton tags assume a tightly identified lepton (see Appendix A). The hadron tag consists of a track failing the lepton ID. The $\rho$ tag requires a $\rho$ meson, reconstructed from a hadron and a $\pi^0$ on the 1-prong side. Criteria for a reconstructed $\rho$ are:

- $\pi^0$ satisfies the criteria in chapter 3.4.1,
- $0.650 < m_{h\pi^0} < 0.875$ GeV/c$^2$

The lepton tags have significantly less $q\overline{q}$ background and are selected in both of our analyses. The hadron ($\pi/K$) and $\rho$ tags, although efficient, are much more contaminated with $q\overline{q}$ background. The choice of the tags is different for each analysis, and depend on the maximal S/$\sqrt{B}$, where S is the signal and B is the expected background in the signal region after all cuts. Events with the following 1-prong tags are selected for $\tau^- \rightarrow 4\pi^-3\pi^+(\pi^0)\nu_\tau$ and $\tau^- \rightarrow 3\pi^-2\pi^+2\pi^0\nu_\tau$ analyses:

- electron with at most 1 photon on the tag side ($\tau^- \rightarrow 4\pi^-3\pi^+(\pi^0)\nu_\tau$ and $\tau^- \rightarrow 3\pi^-2\pi^+2\pi^0\nu_\tau$)
- muon with at most 1 photon on the tag side ($\tau^- \rightarrow 4\pi^-3\pi^+(\pi^0)\nu_\tau$ and $\tau^- \rightarrow 3\pi^-2\pi^+2\pi^0\nu_\tau$)
- reconstructed $\rho$ with no additional photon on the tag side ($\tau^- \rightarrow 4\pi^-3\pi^+(\pi^0)\nu_\tau$)
- hadron with no additional photon on the tag side ($\tau^- \rightarrow 4\pi^-3\pi^+(\pi^0)\nu_\tau$)

In the $\tau^- \rightarrow 3\pi^-2\pi^+2\pi^0\nu_\tau$ analysis, the energy of the allowed photon is required to be less than 500 MeV.

| **1-prong Tags** | **signal** | **generic** $\tau$(%) | **uds** (%) | $c\bar{c}$(%) |
|---|---|---|---|---|
| e + 0$\gamma$ | 13.2±0.3 | 12.9±0.9 | 0.2±0.0 | 0.7±0.1 |
| e + 1$\gamma$ | 5.8±0.2 | 5.7±0.6 | 0.4±0.0 | 1.4±0.1 |
| e + > 1$\gamma$ | 1.9±0.2 | 2.5±0.6 | 2.1±0.2 | 9.4±0.7 |
| $\mu$ + 0$\gamma$ | 9.4±0.2 | 8.4±0.7 | 0.1±0.0 | 0.5±0.1 |
| $\mu$ + 1$\gamma$ | 2.0±0.1 | 2.1±0.3 | 0.2±0.0 | 1.0±0.1 |
| $\mu$ + > 1$\gamma$ | 0.6 ±0.1 | 0.7±0.3 | 0.5±0.1 | 4.4±0.5 |
| $\rho$ + 0$\gamma$ | 8.6±0.2 | 9.0±0.7 | 2.7±0.1 | 1.3±0.1 |
| $\rho$ + 1$\gamma$ | 4.4±0.2 | 4.5±0.5 | 4.1±0.1 | 2.6±0.1 |
| $\rho$ + > 1$\gamma$ | 5.5±0.3 | 5.1±0.9 | 13.9±0.4 | 15.3±0.7 |
| h + 0$\gamma$ | 19.8±0.4 | 19.1±1.1 | 8.7±0.2 | 2.8±0.2 |
| h + 1$\gamma$ | 12.8±0.3 | 13.4±0.9 | 14.6±0.2 | 7.0±0.2 |
| h + > 1$\gamma$ | 16.0±0.6 | 16.6±1.8 | 52.5±2.7 | 53.6±1.6 |

Table 3.5: MC efficiencies (%) of the 1-prong tags after the pre-selection in the $\tau^- \to 3\pi^-2\pi^+2\pi^0\nu_\tau$ analysis. Here, e and $\mu$ mean a tightly identified electron and muon. The hadron tag "h" implies a particle **not** identified as an electron, muon or a $\rho$-meson. The table is similar for the $\tau^- \to 4\pi^-3\pi^+(\pi^0)\nu_\tau$ analysis.

### 3.6.4 Background Suppression Summary

The cumulative efficiencies of the event selection cuts are shown in Tables 3.6 and 3.7 for $\tau^- \to 4\pi^-3\pi^+(\pi^0)\nu_\tau$ and $\tau^- \to 3\pi^-2\pi^+2\pi^0\nu_\tau$ analyses respectively. In both analyses, the background is suppressed to minimal levels, and the signal efficiencies allow us to probe the signal decay branching ratios down to $O(10^{-7})$. Below is the summary and conclusion of the signal selection using the cut-based approach:

- Monte Carlo simulations are used to study and develop the cuts for signal-background separation.

- Background from the generic $\tau$ events is suppressed by using particle ID, transverse momentum and DOCA$_{XY}$ information on the signal side. The remaining $\tau$ background is primarily from the $\tau^- \to 3\pi^- 2\pi^+ \pi^0 \nu_\tau$ decay contributing though a reconstruction of a fake $\pi^0$.

- Background from $q\overline{q}$, which consists of *uds* and $c\overline{c}$ processes, is suppressed after tagging the 1-prong with a lepton tag and replacing the invariant mass of the signal side tracks with the pseudo mass. Background from $B\overline{B}$ is insignificant and does not contribute to the signal region.

In conclusion, we show the $\tau^- \to 4\pi^- 3\pi^+ \nu_\tau$, $\tau^- \to 4\pi^- 3\pi^+ \pi^0 \nu_\tau$ and $\tau^- \to 3\pi^- 2\pi^+ 2\pi^0 \nu_\tau$ selection efficiencies as a function of the $\tau$ pseudo mass (see Figure 3.11), based on the MC truth matched particles. As expected, the distribution is flat in the signal region. The drop of the efficiency at the higher mass, outside the signal region, is primarily due to the cut on the thrust magnitude, which is correlated with the pseudo mass and tends to reject high-mass events.

| **Cuts applied** | $\mathbf{7}\pi\nu_\tau$(%) | $\mathbf{7}\pi\pi^0\nu_\tau$(%) | **gen.** $\tau$ | $\mathbf{5}\pi\nu_\tau$ | $\mathbf{5}\pi\pi^0\nu_\tau$ | $q\overline{q}$ |
|---|---|---|---|---|---|---|
| Pre-selection | 23.6±1.4 | 22.8±1.4 | 767 | 198 | 187 | 47719 |
| Pion ID (signal side) | 20.7±1.3 | 19.6±1.3 | 108 | 64 | 75 | 17289 |
| Conversion veto (signal side) | 15.8±1.0 | 14.9±1.0 | 0 | 4.7 | 9.2 | 5293 |
| 1-prong tags | 10.2±0.7 | 9.6±0.7 | 0 | 1.7 | 4.2 | 659 |
| $1.3 < \mathrm{M}_{pseudo}^{7prong} < 1.8$ GeV/c$^2$ | 9.4±0.6 | 9.3±0.6 | 0 | 0.4 | 0.8 | 3.1 |

Table 3.6: $\tau^- \to 4\pi^- 3\pi^+ (\pi^0) \nu_\tau$ analysis. Effect of the cuts applied to each MC sample. All background samples are scaled to 232 fb$^{-1}$ data luminosity. Generic $\tau$ background is a combination of 1- and 3-prong $\tau$ events. $5\pi$ and $5\pi\pi^0$ are the additional samples studied as a main background from $\tau$ events. Signal efficiency is given in (%), background is shown in number of events (normalized).

| **Cuts applied** | $5\pi 2\pi^0\nu_\tau$ (%) | gen. $\tau$ | $5\pi\pi^0\nu_\tau$ | $uds$ | $c\overline{c}$ |
|---|---|---|---|---|---|
| Pre-selection | 3.48 % | 882 | 57 | 20979 | 8380 |
| 1-prong tags | 1.00 % | 243 | 17 | 120 | 252 |
| Pion ID (signal side) | 0.91 % | 64 | 15 | 56 | 76 |
| Conversion veto (signal side) | 0.72 % | 2.5 | 12 | 28 | 29 |
| $1.3 < \mathrm{M}_{pseudo}^{5prong} < 1.8$ GeV/c$^2$ | 0.66 % | 0.7 | 3.2 | 0.7 | 1.4 |

Table 3.7: $\tau^- \to 3\pi^- 2\pi^+ 2\pi^0 \nu_\tau$ analysis. Effect of the cuts applied to MC signal $5\pi 2\pi^0\nu_\tau$ and background. All background samples are scaled to 232 fb$^{-1}$ data luminosity. Generic $\tau$ background does not contain the $\tau^- \to 3\pi^- 2\pi^+ \pi^0 \nu_\tau$ mode, which is considered separately as the largest background remaining after all the cuts. Signal efficiency is given in (%), background is shown in number of events (normalized).

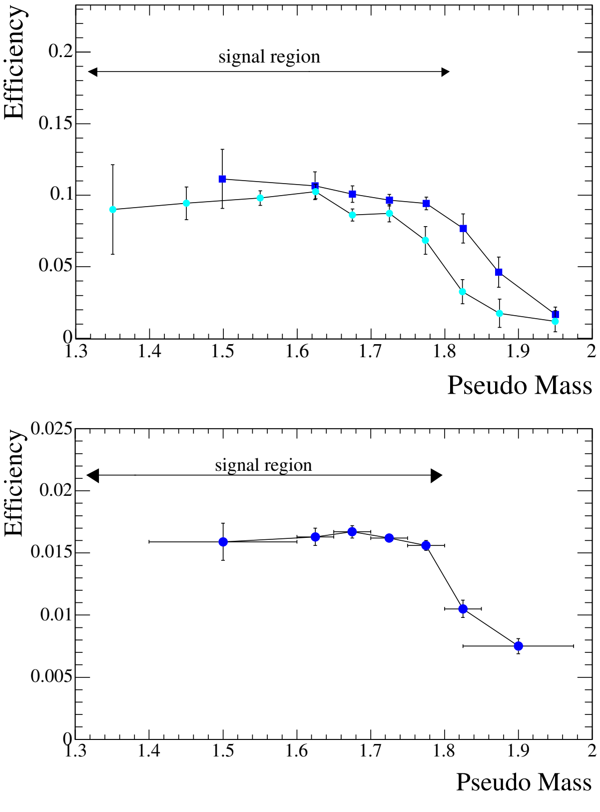

Figure 3.11: Signal selection efficiency as a function of the $\tau$ pseudo mass. Top plot: $\tau^- \to 4\pi^- 3\pi^+ \nu_\tau$ (dark blue) and $\tau^- \to 4\pi^- 3\pi^+ \pi^0 \nu_\tau$ (light blue) modes. Bottom plot: $\tau^- \to 3\pi^- 2\pi^+ 2\pi^0 \nu_\tau$ mode.

# CHAPTER 4

# DATA AND MONTE CARLO COMPARISON

The efficiency tables in the previous section show that the background simulated by Monte Carlo is strongly suppressed. But what if the MC simulation of the background does not accurately depict the data?

Monte Carlo simulations are based on known data and are tuned for a proper representation of known processes. Simulation of $\tau$ background decays is based on well-measured branching ratios and decay properties. Simulation of hadronic $q\bar{q}$ background is much more complicated since it relies heavily on correct modeling of QCD processes like quark fragmentation and hadronization. This is hard to model correctly, especially for the yet to be observed seven-hadron processes that we wish to study.

Tables 4.1 and 4.2 compare the number of events in the data and MC for $\tau^- \rightarrow 4\pi^-3\pi^+(\pi^0)\nu_\tau$ and $\tau^- \rightarrow 3\pi^-2\pi^+2\pi^0\nu_\tau$ analyses. There is a clear excess of data compared to Monte Carlo in both analyses. Moreover, the excess increases with the cuts. To make sure there is nothing extraordinary in the cut variables, data and MC for different variables after pre-selection are plotted (see Figure 4.1).

| Cuts applied | Monte Carlo | Data | Data/MC |
|---|---|---|---|
| Pre-selection | 48319 | 92772 | 1.92 |
| Pion ID (signal side) | 17385 | 42941 | 2.47 |
| Conversion veto (signal side) | 5296 | 19436 | 3.67 |
| 1-prong tags | 659 | 3475 | 5.27 |

Table 4.1: $\tau^- \to 4\pi^- 3\pi^+ (\pi^0)\nu_\tau$ analysis: Data-MC efficiency comparison throughout the cuts. MC consists of $\tau$, *uds* and $c\bar{c}$ backgrounds scaled to data luminosity of 232 fb$^{-1}$. Data is blinded below 1.8 GeV/c$^2$.

| Cuts applied | Monte Carlo | Data | Data/MC |
|---|---|---|---|
| Pre-selection | 30298 | 37778 | 1.25 |
| 1-prong tags | 632 | 864 | 1.37 |
| Pion ID (signal side) | 211 | 416 | 1.97 |
| Conversion veto (signal side) | 72 | 172 | 2.42 |

Table 4.2: $\tau^- \to 3\pi^- 2\pi^+ 2\pi^0 \nu_\tau$ analysis: Data-MC efficiency comparison throughout the cuts. MC consists of $\tau$, *uds* and $c\bar{c}$ backgrounds scaled to data luminosity of 232 fb$^{-1}$. Data is blinded below 1.8 GeV/c$^2$.

To understand the source of the data excess, MC and data are compared throughout the same selection cuts for various 1-N ($N \geq 3$) topologies. The level of disagreement is different for different topologies, as shown in Figure 4.2. For low track multiplicity topologies like 1-1 and 1-3, which are dominated by the $\tau$ events, the data-MC discrepancy is negligible and the agreement is consistently good throughout the cuts. The content of $q\bar{q}$ and $\tau$ events is roughly the same for topologies like 1-4 and 1-5 (this is different for $\tau^- \to 3\pi^- 2\pi^+ 2\pi^0 \nu_\tau$ analysis, which is also a 1-5 topology case, but has two additional $\pi^0$s, which increases the $q\bar{q}$ content significantly), and the data-MC discrepancy, although noticeable, is tolerable.

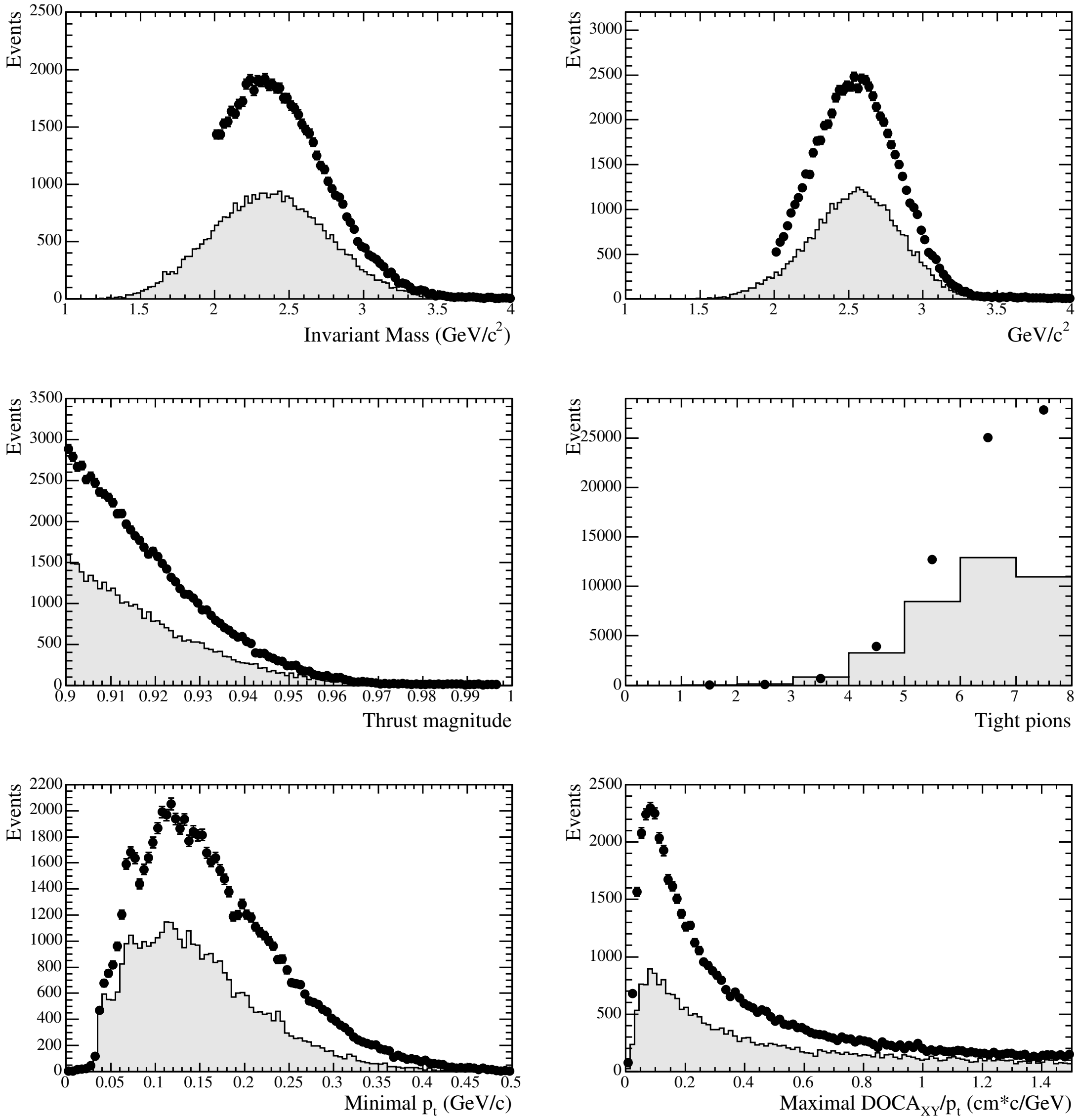

Figure 4.1: Data-MC comparison of cut variables after pre-selection for the $\tau^- \rightarrow 4\pi^- 3\pi^+ (\pi^0)\nu_\tau$ analysis. MC consists of $\tau$, uds, $c\bar{c}$ and $b\bar{b}$ backgrounds, each scaled to data luminosity of 124.3 fb$^{-1}$. The shaded area represents MC. In this particular figure, the data is blinded below 2 GeV/c$^2$ pseudo-mass.

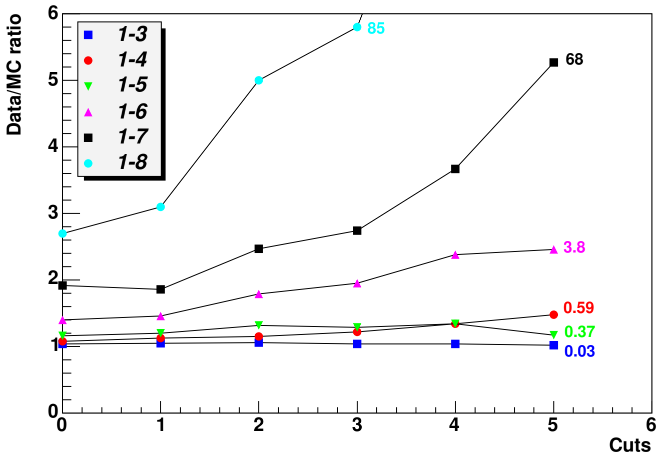

Figure 4.2: Data/MC ratio for different topologies of the $\tau^- \to 4\pi^- 3\pi^+ (\pi^0)\nu_\tau$ analysis. The numbers on the plot correspond to the $q\overline{q}/\tau$ ratio for each topology after the last cut.

Large track multiplicity topologies like 1-6, 1-7 and 1-8 are completely dominated by $q\overline{q}$ events, and the data-MC discrepancy is substantial. The trend is clear: the larger the $q\overline{q}/\tau$ ratio in the sample, the larger the data-MC discrepancy. Since the $q\overline{q}$ events dominate the multi-prong background, Monte Carlo simulation of the $e^+e^- \to q\overline{q}$ processes does not adequately represent the data in $\tau^- \to 4\pi^- 3\pi^+ (\pi^0)\nu_\tau$ and $\tau^- \to 3\pi^- 2\pi^+ 2\pi^0 \nu_\tau$ analyses, and cannot be used alone for the background estimate.

Contrary to $q\overline{q}$ processes, Monte Carlo simulation of $\tau$ events is based on measured branching ratios, and therefore is much more reliable to use for a background estimate. Given the smaller contribution from the $\tau$ background, the uncertainty of its estimate is primarily statistical and covers the small data-MC disagreement, which is within statistical and systematic errors. The level of disagreement is estimated by loosening the cuts against $\tau$ events, thus enhancing the $\tau$ content in the data, and imposing stricter criteria against $q\overline{q}$ background ensuring the purity of the $\tau$ sample in the data.

Despite the quantitative disagreement between the data and MC of the $q\overline{q}$ events, the shape of the pseudo-mass distribution appears to be correctly modeled (see Figure 4.3). This allows us to use the $q\overline{q}$ PDF obtained from Monte Carlo directly on the data.

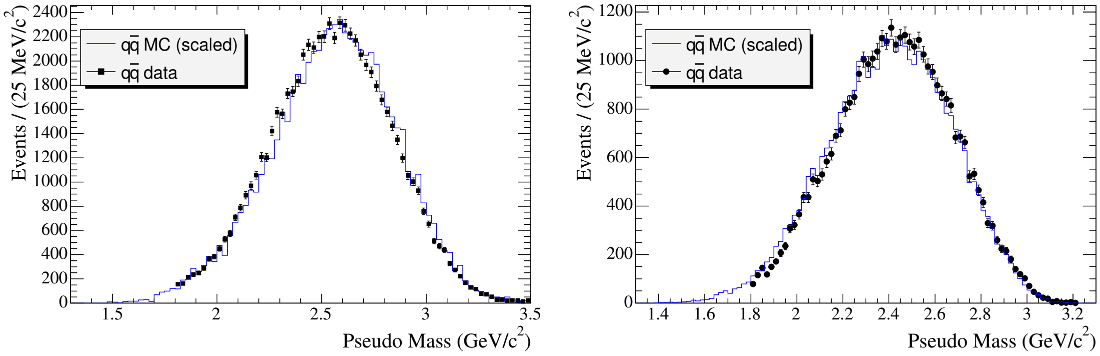

Figure 4.3: Pseudo-mass distributions of the data (blinded below 1.8 GeV/c$^2$ and MC $q\overline{q}$ for $\tau^- \to 4\pi^- 3\pi^+ (\pi^0)\nu_\tau$ (left plot) and $\tau^- \to 3\pi^- 2\pi^+ 2\pi^0 \nu_\tau$ (right plot) analyses. The $q\overline{q}$ data is obtained by subtracting the $\tau$ MC from the data distribution. MC $q\overline{q}$ is a combination of $uds$ and $c\overline{c}$ backgrounds, scaled to the number of data events above 1.8 GeV/c$^2$.

# CHAPTER 5

# BACKGROUND ESTIMATE IN THE SIGNAL REGION

As discussed in the previous section, Monte Carlo cannot be used for the quantitative $q\overline{q}$ background estimate in the data for both $\tau^- \to 3\pi^-2\pi^+2\pi^0\nu_\tau$ and $\tau^- \to 4\pi^-3\pi^+(\pi^0)\nu_\tau$ analyses. Monte Carlo simulation, however, suggests a Gaussian-like pseudo-mass distribution, which is also seen in the data above 1.8 GeV/$c^2$. The $q\overline{q}$ background in the signal region can be estimated by fitting the pseudo-mass spectrum above the signal region, and then extrapolating the fit below 1.8 GeV/$c^2$. The fitting procedures are slightly different for the $\tau^- \to 4\pi^-3\pi^+(\pi^0)\nu_\tau$ and $\tau^- \to 3\pi^-2\pi^+2\pi^0\nu_\tau$ analyses, but the idea is the same.

On the other hand, Monte Carlo simulation of generic $\tau$ events is reliable and valid to use for the $\tau$ background estimate in the data.

Below are the background estimate scenarios.

1. For $\tau^- \to 4\pi^-3\pi^+(\pi^0)\nu_\tau$ analysis:
    - Estimate the $\tau$ background from the MC and scale it to the data luminosity.
    - Subtract the $\tau$ background from the data to get a $q\overline{q}$ data sample.

- Fit the $q\overline{q}$ data pseudo-mass spectrum with a Gaussian function from 1.8 to 2.5 GeV/$c^2$. There is no need to fit the whole spectrum, since the high-mass events are of no interest for this analysis and may distort the fit parameters.
- Extrapolate the fit below 1.8 GeV/$c^2$. The ratio of integrals

  $$N_{bkg} = N_{HM} \frac{\int_{1.3}^{1.8} e^{-(m-\mu)^2/2\sigma^2} \ dm}{\int_{1.8}^{2.5} e^{-(m-\mu)^2/2\sigma^2} \ dm} \tag{5.1}$$

  where $N_{HM}$ is the number of events with the 7-prong pseudo-mass between 1.8 to 2.5 GeV/c$^2$, yields an estimate of the number of background events in the signal region.

2. For $\tau^- \to 3\pi^- 2\pi^+ 2\pi^0 \nu_\tau$ analysis:

   - Define a "Crystal Ball" PDF [28] for the $\tau$ background pseudo-mass spectrum after all cuts. The integral of the PDF in the signal region (1.3-1.8 GeV/c$^2$) normalized to the data luminosity provides the $\tau$ background estimate.
   - Define Gaussian PDFs for the $uds$ and $c\overline{c}$ spectra after all cuts.
   - Subtract the $\tau$ distribution from the data using the $\tau$ PDF.
   - Add $uds$ and $c\overline{c}$ PDFs and normalize the combined PDF to the data. This will be the MC fit scaled to the data, the integral of which will provide the $q\overline{q}$ background estimate in the signal region.
   - Use the combined $uds$ and $c\overline{c}$ PDF to fit the data. When fitting, we allow the PDF shape parameters to float. This will be called a data fit, the integral of which will provide the $q\overline{q}$ background estimate in the signal

region. The data fit will be used for the actual estimate, while the MC fit will be used as a cross-check.

## 5.1 $\tau$ Background Estimate

The background from $\tau$ events to the $\tau^- \to 4\pi^-3\pi^+(\pi^0)\nu_\tau$ mode, estimated using Monte Carlo simulation and presented in Table 3.6, yields 1.3±1.0 events in the signal region. The error of this estimate is due to the limited MC statistics.

Similar to the $\tau^- \to 4\pi^-3\pi^+(\pi^0)\nu_\tau$ analysis, the $\tau^- \to 3\pi^-2\pi^+\pi^0\nu_\tau$ decay is the dominant background to the $\tau^- \to 3\pi^-2\pi^+2\pi^0\nu_\tau$ mode (see Table 3.7). To study this background closely, we have generated a $\tau^- \to 3\pi^-2\pi^+\pi^0\nu_\tau$ sample corresponding to 1437 $\text{fb}^{-1}$ of data, in addition to 459 $\text{fb}^{-1}$ already available from the generic $\tau$ sample. The pseudo-mass distribution of the MC $\tau^- \to 3\pi^-2\pi^+\pi^0\nu_\tau$ events is shown in Figure 5.1 for lepton+hadron and lepton tags after all cuts. Since the spectra are similar for the lepton and hadron tags, we fit the combined lepton+hadron spectrum with the "Crystal Ball" function, and then apply the PDF on the lepton tag. This allows us to extract the background estimate using a statistically larger sample, which increases the statistical precision of the estimate. The good agreement between the estimated and observed (counted) background in the signal region, indicates that the chosen PDF correctly represents the distribution of the $\tau^- \to 3\pi^-2\pi^+\pi^0\nu_\tau$ events.

Table 5.1 shows the $\tau$ background in the signal region, estimated using the above technique. The remaining background from the $\tau^- \to 2\pi^-\pi^+2\pi^0\nu_\tau$ mode is not fitted due to limited statistics. The last column in the table shows the number of $\tau$ background events in the signal region counted from the final MC pseudo-mass

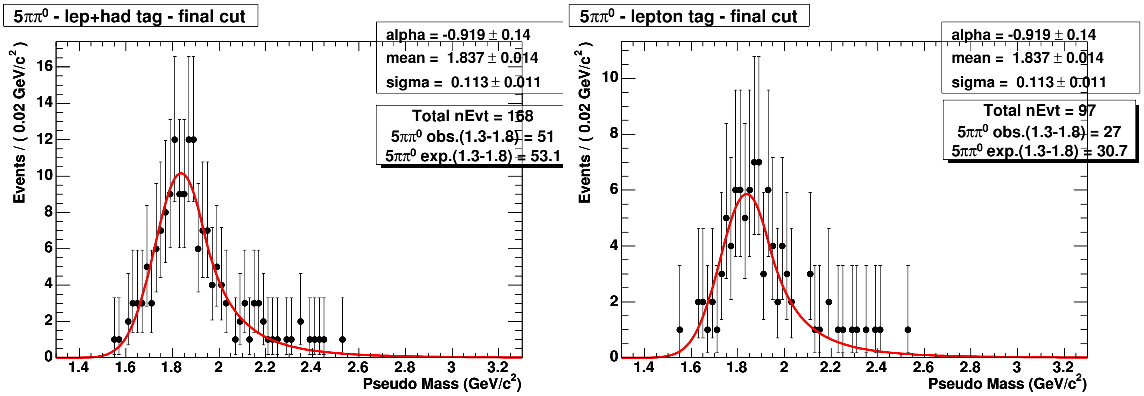

Figure 5.1: Pseudo-mass distributions of the MC $\tau^- \to 3\pi^-2\pi^+\pi^0\nu_\tau$ events for lepton+hadron (left plot) and lepton (right plot) tags. The distribution of the high-statistics sample with the lepton+hadron tag is fitted with a crystal ball function, and its PDF is used on the final $\tau^- \to 3\pi^-2\pi^+\pi^0\nu_\tau$ pseudo-mass distribution. Distributions are *not* scaled to the data luminosity.

| 1-prong Tags | $\tau^- \to 3\pi^-2\pi^+\pi^0\nu_\tau$ | Total $\tau$ bkg. (fit) | Total $\tau$ bkg. (count) |
|---|---|---|---|
| lepton+hadron | 6.3±0.9 | 7.3±1.1 | 7.0±1.1 |
| lepton | 3.6±0.6 | 4.3±0.8 | 3.9±0.8 |

Table 5.1: Estimated $\tau$ background in the signal region scaled to the data luminosity of 232 $\text{fb}^{-1}$. Column 4 is shown as a comparison to the actual estimates from column 3. Errors shown are statistical only.

distribution scaled to the data luminosity (see Table 3.7). There is good agreement between the number of counted events and the estimate the fit.

## 5.2 $q\overline{q}$ Background Estimate

The procedure for the $q\overline{q}$ background estimate is slightly different for the $\tau^- \to 4\pi^-3\pi^+(\pi^0)\nu_\tau$ and $\tau^- \to 3\pi^-2\pi^+2\pi^0\nu_\tau$ analyses. We will discuss them separately.

### 5.2.1 $\tau^- \rightarrow 4\pi^- 3\pi^+ (\pi^0) \nu_\tau$

Monte Carlo simulation of $q\overline{q}$ events suggests that a Gaussian fit below 2.6 GeV/c$^2$ provides a good representation of the background distribution in the signal region. No resonances from the $q\overline{q}$ are expected in the signal region, and the data agrees with simulation shape-wise above 1.8 GeV/c$^2$. The $q\overline{q}$ background in the signal region is estimated by fitting the $\tau$-subtracted data pseudo-mass spectrum in the 1.8 - 2.6 GeV/c$^2$ region with a Gaussian, and then extrapolating the fit to the signal region. The estimate is not sensitive to the upper bound of the fit.

The final pseudo-mass spectrum is based on substantially smaller statistics than the spectrum after the pre-selection, and correspondingly the fit parameters have larger uncertainties. However, the variables used in the cut-based event selection are not correlated with the pseudo mass, and the fit parameters (mean and sigma) only marginally vary with the tighter cuts. Figure 5.2 illustrates the $q\overline{q}$ data pseudo-mass spectra and their fits after the four selection steps. Figure 5.3 shows that the fit shape parameters can be approximated with the values from the pre-selection fit.

The background is estimated using equation 5.1. Table 5.2 shows the estimates obtained by fitting the $q\overline{q}$ data pseudo-mass spectrum after each cut and by using the fixed mean and sigma from the pre-selection fit in the extrapolation process. Comparison shows similar background yields with significantly smaller errors for the extrapolation method used in this analysis. The error calculation will be explained in section 6.2.2.

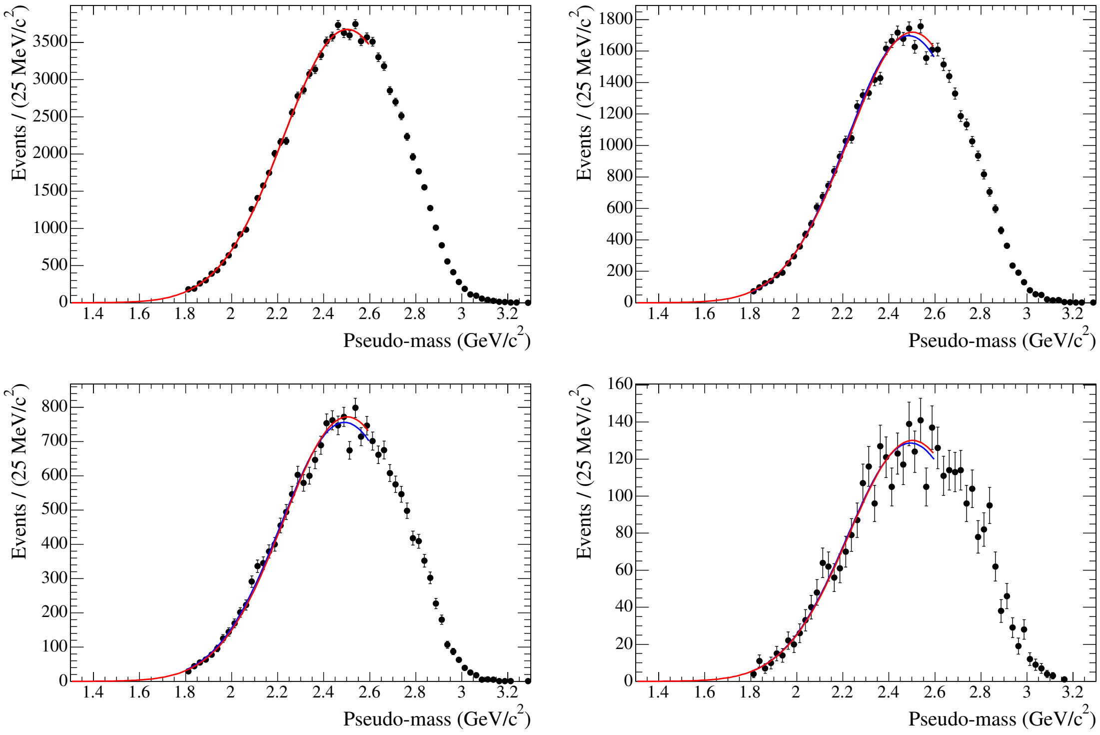

Figure 5.2: Pseudo-mass distributions and fits of the $\tau$-subtracted data after pre-selection (upper left), particle ID (upper right), conversion veto (lower left) and 1-prong tags (lower right). The blue curve represents the fit of the data from 1.8 to 2.6 GeV/c$^2$. The red curve superimposed is the Gaussian PDF with shape parameters identical to the values of the pre-selection fit. The data is blinded below 1.8 GeV/c$^2$.

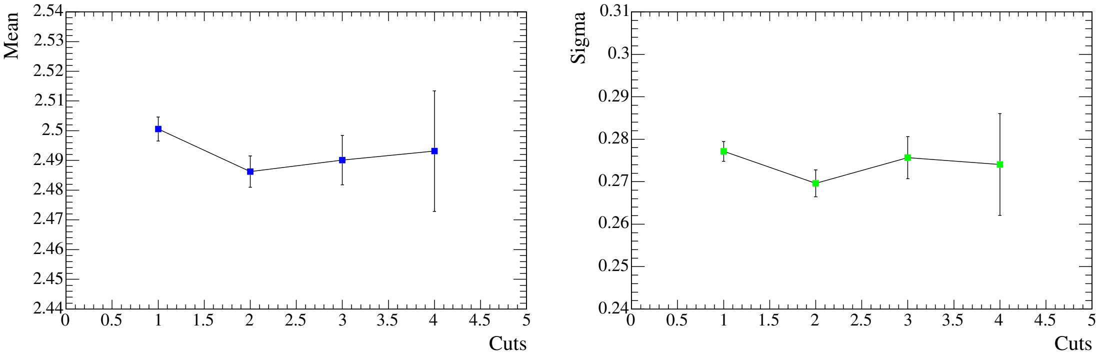

Figure 5.3: Mean and sigma of 1-7 topology $\tau$-subtracted data pseudo-mass fit from 1.8 to 2.6 GeV after each cut.

| **Cuts applied** | $N_{q\overline{q}}$ **(fixed** $\mu$,$\sigma$**)** | $N_{q\overline{q}}$ **(current** $\mu$,$\sigma$**)** |
|---|---|---|
| Pre-Selection | 574 ± 21 | 574 ± 21 |
| Particle ID | 241 ± 10 | 222 ± 19 |
| Conversion veto | 119 ± 5 | 126 ± 18 |
| 1-prong tags | 20.3 ± 0.8 | 20.2 ± 6.6 |

Table 5.2: Estimated $q\overline{q}$ background in the signal region of the 1-7 topology data. A comparison between the $q\overline{q}$ estimates obtained by fitting the pseudo-mass spectra from 1.8 to 2.6 GeV/c$^2$ with fixed and floating fit parameters is shown.

### Validation of the background estimate method

To validate the $q\overline{q}$ background estimate method, we study 1-8 topology data events. Although statistically limited, these events provide a clean hadronic background sample with a negligible ($< 0.5\%$) signal contribution, allowing us to validate the fitting method in the otherwise blinded signal region below 1.8 GeV/c$^2$.

Due to more tracks on the signal side, the pseudo-mass is larger than in the 1-7 topology and less events are observed in the signal region. Similar to the 1-7 topology, the $B\overline{B}$ contamination is negligible, so the $q\overline{q}$ data consists of $e^+e^- \rightarrow (u\overline{u}, d\overline{d}, s\overline{s})$ and $e^+e^- \rightarrow c\overline{c}$ events. The small $\tau$ contamination is subtracted from the data using a Monte Carlo simulation. The event selection and background estimate procedures for the 1-8 topology are similar to the 1-7 topology. Here, we require 8 charged tracks on the signal side and the fits are performed from 1.8 to 2.7 GeV/c$^2$. The $q\overline{q}$ data pseudo-mass spectra and the fits are shown in figure 5.4 for each of the four selection steps. As before, to extract the background estimate we use fixed values of the mean and the sigma, taken after the pre-selection.

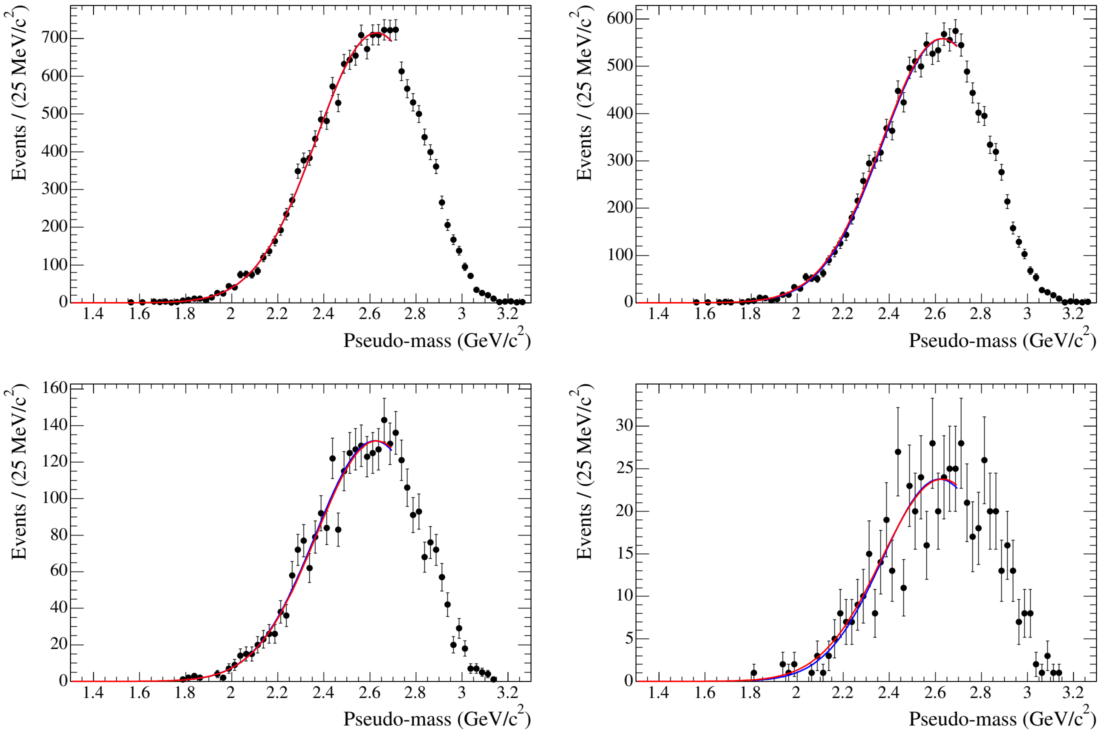

Figure 5.4: Pseudo-mass distributions and fits of the "$\tau$-event-free" 1-8 topology data after pre-selection (upper left), particle ID (upper right), conversion veto (lower left) and 1-prong tags (lower right). The blue curve represents the fit of the data from 1.8 to 2.7 GeV/c$^2$. The red curve superimposed is the Gaussian PDF with shape parameters identical to the values of the pre-selection fit.

The number of predicted and observed background events are compared in Table 5.3. The agreement between the two estimates is reasonable.

Validation can also be performed on the 1-7 topology data events in the pseudo-mass region of 1.8-2.0 GeV/c$^2$. This region is the closest to the blinded tail of the pseudo-mass distribution and provides a high-statistics sample. The comparison between the expected $q\overline{q}$ background extracted from the fitting method and the observed events shows good agreement (see Table 5.3).

| Cuts | $q\overline{q}$ expected (1-8 topology) | $q\overline{q}$ observed (1-8 topology) | $q\overline{q}$ expected (1-7 topology) | $q\overline{q}$ observed (1-7 topology) |
|---|---|---|---|---|
| Thrust | 19.0±2.7 | 23 | 3356±79 | 3238 |
| Particle ID | 12.2±1.6 | 10 | 1503±40 | 1415 |
| Conversion veto | 2.7±0.3 | 1 | 656±18 | 642 |
| 1-prong tag | 0.5±0.1 | 0 | 114±4 | 106 |

Table 5.3: Comparison between the expected $q\overline{q}$ background and observed $q\overline{q}$ events after each cut for 1-8 topology data in the (1.3-1.8 GeV/c$^2$) region, and 1-7 topology data in the (1.8-2.0 GeV/c$^2$) region.

We conclude, that the $q\overline{q}$ background estimate method is valid and a background yield of 20.3±0.7 events (see Table 5.2) is expected in the signal region.

### 5.2.2 $\tau^- \longrightarrow 3\pi^- 2\pi^+ 2\pi^0 \nu_\tau$

Similar to the $\tau^- \rightarrow 4\pi^- 3\pi^+ (\pi^0) \nu_\tau$ analysis, the background is estimated directly from the data. Here, however, rather than fitting the pseudo-mass spectrum with a Gaussian, we fit it with a PDF extracted from the Monte Carlo simulation.

The backgrounds from the *uds* and $c\overline{c}$ events are studied separately, and their MC simulated pseudo-mass distributions are fitted after all cuts with two Gaussians with different parameters. (Figure 5.5, top plots). Both PDFs are then added to form a double-Gaussian $q\overline{q}$ PDF, which is superimposed on the MC $q\overline{q}$ distribution (Figure 5.5, bottom left plot). Good agreement is observed between the number of $q\overline{q}$ events in the signal region estimated from the fit and counted in the distribution.

To extract the $q\overline{q}$ background in the signal region, we subtract the expected $\tau$ background contribution from the data pseudo-mass distribution, and fit the resulting histogram in the range $1.8 < M^* < 3.3\,\mathrm{GeV/c^2}$ with a double-Gaussian PDF whose parameters are allowed to float. To avoid experimenter bias, this fit is performed "blind", with the data in the signal region hidden. The fit function is then extrapolated below $1.8\,\mathrm{GeV/c^2}$ and its integral between 1.3 and $1.8\,\mathrm{GeV/c^2}$ yields the $q\overline{q}$ background estimate in the data.

Figure 5.5 (bottom right plot) shows the $q\overline{q}$ data pseudo-mass distribution and its fit extracted from the MC $q\overline{q}$ PDF. The background estimates using MC and data fits are shown for comparison. The estimate from the $q\overline{q}$ data fit ($2.2^{+1.7}_{-1.0}$ events) is final. The error calculation will be explained in section 6.2.2.

**Validation of the background estimate method**

Similar to the $\tau^- \to 4\pi^- 3\pi^+ (\pi^0) \nu_\tau$ case, the validation of the background estimate method is performed on a data sample which has a negligible amount of signal and background $\tau$ events. Such a 'signal-free' data sample can be studied unblinded. To obtain it, we require at least 3 high-energy photons ($E_\gamma > 300$ MeV) on the tag side, not associated with a $\pi^0$. MC studies show that after this requirement the expected signal efficiency is less than 0.01%. Background contamination from generic $\tau$ events is very small and is estimated from MC. Background from the $q\overline{q}$ events is estimated using both the MC and data fits. The resulting data spectra and the fits are shown in Figure 5.6. The expected background and observed events are also shown in the statistics box. The agreement indicates that the background estimate method is valid within the errors.

### 5.2.3 Summary of the background estimate

Table 5.4 summarizes the $\tau$ and $q\overline{q}$ background contributions expected in the signal region for both the $\tau^- \to 4\pi^- 3\pi^+ (\pi^0) \nu_\tau$ and $\tau^- \to 3\pi^- 2\pi^+ 2\pi^0 \nu_\tau$ analyses.

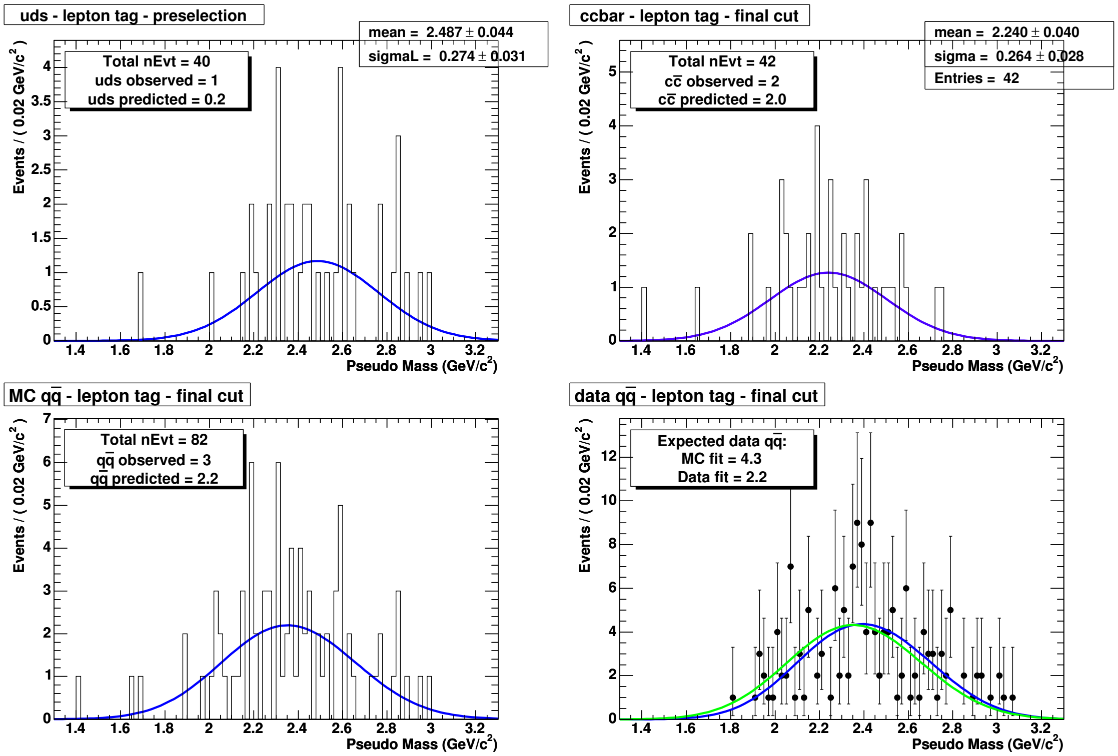

Figure 5.5: Pseudo-mass distributions of the MC *uds* (top left) and $c\bar{c}$ (top right) backgrounds, each fitted with a Gaussian, the total MC $q\bar{q}$ (bottom left) fitted with a double-Gaussian PDF, and the $\tau$-subtracted $q\bar{q}$ data events (blinded below 1.8 GeV/c$^2$) with the green curve being the MC $q\bar{q}$ PDF normalized to the data distribution and the blue curve representing the data fit using the MC $q\bar{q}$ PDF with the shape parameters floating (bottom right). Upper left statistics box shows the number of events in the signal region counted from the distribution and estimated from the fit. MC distributions are *not* scaled to the data luminosity.

| | $\tau^- \to 4\pi^- 3\pi^+ (\pi^0) \nu_\tau$ | $\tau^- \to 3\pi^- 2\pi^+ 2\pi^0 \nu_\tau$ |
|---|---|---|
| $\tau$ background | 1.3±1.0 | 4.3±1.0 |
| $q\bar{q}$ background | 20.3±0.8 | $2.2^{+1.7}_{-1.0}$ |
| Total background | 21.6±1.3 | $6.5^{+2.0}_{-1.4}$ |

Table 5.4: Final $\tau$, $q\bar{q}$ and total background estimates for the $\tau^- \to 4\pi^- 3\pi^+ (\pi^0) \nu_\tau$ and $\tau^- \to 3\pi^- 2\pi^+ 2\pi^0 \nu_\tau$ analyses.

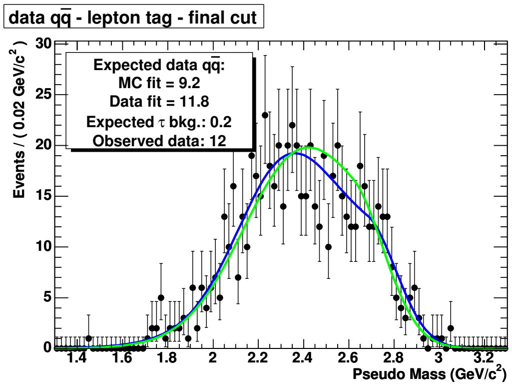

Figure 5.6: "Signal-free" data unblinded. Green curve is the MC $q\overline{q}$ PDF normalized to the data distribution. Blue curve is the data fit using the MC $q\overline{q}$ PDF with the shape parameters floating within $\pm 2\sigma$ range. Upper left statistics box compares the background in the signal region estimated from the MC and data fits.

# CHAPTER 6

# SYSTEMATIC UNCERTAINTIES AND MONTE CARLO CORRECTIONS

This section will be divided into 3 subsections, describing the uncertainty assigned to the signal efficiencies and the background estimates for the $\tau^- \rightarrow 3\pi^- 2\pi^+ 2\pi^0 \nu_\tau$ and $\tau^- \rightarrow 4\pi^- 3\pi^+ (\pi^0) \nu_\tau$ analyses, and the uncertainty on the number of $\tau$ pairs produced.

## 6.1 Signal Efficiency Uncertainty

The signal efficiency is studied using Monte Carlo simulation. Systematic uncertainties come from the charged track and neutral reconstruction, particle identification, limited MC statistics, luminosity and $\tau^+\tau^-$ cross-section.

### 6.1.1 Track Reconstruction Systematic Uncertainty

Track reconstruction yields a slightly larger efficiency for MC than for the data. This difference is taken into account by the correction factors, which are studied independently at the *BABAR*. Both analyses require *GoodTracksLoose* and *GoodTracksVeryLoose* tracks in an event. We apply flat corrections of -0.8% per GTL and -0.5% per GTVL to tune the MC to data. The systematic uncertainties are assigned as follows:

For **GoodTracksLoose** tracks:

- for tracks with $p_T < 200$ MeV/c the uncertainty is 1.3%.
- for tracks with $p_T > 200$ MeV/c the uncertainty is 0.6%.

For **GoodTracksVeryLoose** tracks:

- for tracks with $p_T < 200$ MeV/c the uncertainty is 1.2%.
- for tracks with $p_T > 200$ MeV/c the uncertainty is 0.7%.

In the final $\tau^- \rightarrow 3\pi^-2\pi^+2\pi^0\nu_\tau$ sample, we have 93% GTL ($p_T > 200$ MeV/c), 4% GTL ($p_T < 200$ MeV/c), 2% GTVL ($p_T > 200$ MeV/c) and 1% GTVL ($p_T < 200$ MeV/c). Thus, the total systematic uncertainty due to tracking is calculated to be 3.9%.

Similarly, the total tracking systematic uncertainty for the $\tau^- \rightarrow 4\pi^-3\pi^+(\pi^0)\nu_\tau$ analysis yields 5.2%.

### 6.1.2 Neutrals Systematic Uncertainty

In the $\tau^- \rightarrow 3\pi^-2\pi^+2\pi^0\nu_\tau$ analysis, two $\pi^0$'s are reconstructed. Based on the data and MC studies of the *pi0Loose* list, $\pi^0$'s have a correction factor of 0.981 applied to MC, and a systematic uncertainty of 3% per $\pi^0$. An additional 1% systematic, incurred by neglecting the weak variation of the efficiency with $\pi^0$ momentum, is added in quadrature. Another 1% uncertainty due to the sublist $\pi^0$ criteria is also added in quadrature. The total uncertainty due to the reconstruction of $2\pi^0$'s is 6.6%. This error is not applied to the $\tau^- \rightarrow 4\pi^-3\pi^+(\pi^0)\nu_\tau$ analysis, since we do not reconstruct a $\pi^0$.

In addition, we assign a 1.8% uncertainty for the signal photon identification following *BABAR*'s standard procedure.

### 6.1.3 Particle Identification Uncertainty

Particle ID (PID) was used extensively throughout both analyses, using different particle selectors. However, the performance of the selectors is not the same for data and MC. Particle identification efficiencies for control data and MC samples were used to derive corrections used in our analyses.

Systematic uncertainties to the PID requirements are calculated using bin-by-bin uncertainties provided by the particle ID efficiency tables. These tables are slightly different for $\tau^- \rightarrow 3\pi^-2\pi^+2\pi^0\nu_\tau$ and $\tau^- \rightarrow 4\pi^-3\pi^+(\pi^0)\nu_\tau$ analyses. Each particle species ($e, \mu$ and $\pi$) is assumed to have an independent error, obtained by averaging the total error of that species over the number of events. As a result, the uncertainties from the electron, muon and pion selectors were calculated to be 0.2%, 2.0% and 0.3% correspondingly for the $\tau^- \rightarrow 3\pi^-2\pi^+2\pi^0\nu_\tau$ analysis [3]. Since the h-tag implies that a particle is not identified as an electron or a muon, its uncertainty is calculated by adding the electron and muon tag uncertainties in quadrature, which yields 2.0%. The errors on each tag are weighted according to the tag efficiencies. For example, the lepton tag consists of 61% of the eletron tag and 39% of the muon tag, so the error of the lepton tag is 0.61×0.2%+0.39×2.0%=0.9%.

---

[3] These values are slightly different for the $\tau^- \rightarrow 4\pi^-3\pi^+(\pi^0)\nu_\tau$ analysis, but the method of the uncertainty calculation is the same.

The uncertainty on the signal side is 0.3% per pion added linearly, which gives 1.5% for the $\tau^- \to 3\pi^-2\pi^+2\pi^0\nu_\tau$, and 2.1% for the $\tau^- \to 4\pi^-3\pi^+(\pi^0)\nu_\tau$ case. The uncertainties of the tag and signal side are added in quadrature. Taking these uncertainties and the tag weights into account, we calculate the total uncertainty of 1.7% for the $\tau^- \to 3\pi^-2\pi^+2\pi^0\nu_\tau$ and 0.5% for the $\tau^- \to 4\pi^-3\pi^+(\pi^0)\nu_\tau$ analysis due to the particle identification.

### 6.1.4 Limited MC statistics

Statistical uncertainties due to limited MC samples are 1.8% for the $\tau^- \to 3\pi^-2\pi^+2\pi^0\nu_\tau$ and 2.7% for the $\tau^- \to 4\pi^-3\pi^+(\pi^0)\nu_\tau$ analysis.

### 6.1.5 Selection Stability

If a cut is applied at the threshold of a distribution, a slight fluctuation in the data may cause a change in the final result. If this effect is substantial, a systematic uncertainty due to it should be assigned.

To check the stability of the selection cuts, we vary them by up to ±10% of their values and calculate the effect on the branching ratio sensitivity. No instabilities were introduced by these variations, therefore we do not assign any additional systematic errors to this source.

### 6.1.6 Summary

All the uncertainties discussed above are summed up in Table 6.1. The uncertainties are added in quadrature to obtain the total uncertainty of the signal efficiency.

|  | $\tau \to 5\pi 2\pi^0 \nu_\tau$ | $\tau \to 7\pi(\pi^0)\nu_\tau$ |
|---|---|---|
| Tracking efficiency | 3.9% | 5.2% |
| Reconstruction of $2\pi^0$'s | 6.6% | N/A |
| Single Photon | 1.8% | N/A |
| PID uncertainty | 1.7% | 2.7% |
| Limited MC statistics | 1.8% | 0.5% |
| Total systematic uncertainty | 8.3% | 5.9% |

Table 6.1: Summary of the systematic uncertainties of the signal efficiency for the $\tau^- \to 3\pi^- 2\pi^+ 2\pi^0 \nu_\tau$ and $\tau^- \to 4\pi^- 3\pi^+ (\pi^0)\nu_\tau$ analyses.

## 6.2 Background Estimate Uncertainty

### 6.2.1 $\tau$ Background

As we described in section 5.1, the $\tau$ background is estimated using Monte Carlo. For the $\tau^- \to 4\pi^- 3\pi^+ (\pi^0)\nu_\tau$ analysis, MC predicts 1±1 $\tau^- \to 3\pi^- 2\pi^+ \nu_\tau$ events in 538 fb$^{-1}$, and 2±1.4 $\tau^- \to 3\pi^- 2\pi^+ \pi^0 \nu_\tau$ events in 552 fb$^{-1}$ of data. Both errors are statistical. This corresponds to 0.43±0.43 $\tau^- \to 3\pi^- 2\pi^+ \nu_\tau$ and 0.84±0.59 $\tau^- \to 3\pi^- 2\pi^+ \pi^0 \nu_\tau$ events in 232 fb$^{-1}$ of data. The MC corrections and the uncertainties due to charged track reconstructions, particle ID, luminosity and $\tau^+\tau^-$ cross-section described in section 6.1 also apply to the $\tau$ background estimate. In addition, there is a 14.9% branching ratio error for the $\tau^- \to 3\pi^- 2\pi^+ \pi^0 \nu_\tau$ mode added in quadrature to the uncertainties described above. The final $\tau$ background estimate is then 1.3±1.0 events.

For the $\tau^- \to 3\pi^- 2\pi^+ 2\pi^0 \nu_\tau$ case, the estimate of the dominant $\tau^- \to 3\pi^- 2\pi^+ \pi^0 \nu_\tau$ background is derived from the $\tau$ pseudo-mass fits (see section 5.1). The uncertainty of this estimate is based on the errors of fitted PDF shape parameters, namely the central value and the width. A two-dimensional Gaussian PDF [29], which includes correlations between the shape parameters, is used in a toy Monte Carlo to generate the values of the mean and the sigma according to their uncertainties expressed in the covariance matrix. The shape parameters are then used to estimate the number of background events in the signal region using the accept/reject method. This is repeated 100000 times and the distribution of the estimated number of background events is used to extract the uncertainty of the estimate by calculating 68% ($\pm 1\sigma$) from the central value. Figure 6.1 shows the distribution and the errors of the background estimate. Since the $\tau^- \rightarrow 3\pi^- 2\pi^+ \pi^0 \nu_\tau$ sample corresponds to 1896 $\mathrm{fb}^{-1}$ of data, the central value is larger than the estimates provided in Table 5.1, and both the estimate and its error are scaled down to the data luminosity.

Other contributions to the uncertainty include the statistical error on the fitted number of events in the pseudo-mass spectrum, the 8.4% error for tracking etc., and the 14.9% error of the $\tau^- \rightarrow 3\pi^- 2\pi^+ \pi^0 \nu_\tau$ branching ratio.

The remaining background from the $\tau^- \rightarrow 2\pi^- \pi^+ 2\pi^0 \nu_\tau$ mode is not fitted due to limited statistics (less than 5 events out of 675 $\mathrm{fb}^{-1}$ for each tag). The uncertainty of its contribution is calculated as a statistical error on the number of events in the signal region. The error of the $\tau^- \rightarrow 2\pi^- \pi^+ 2\pi^0 \nu_\tau$ branching ratio (7.4%) is also taken into account. This yields an estimate of $0.7 \pm 0.5$ $\tau^- \rightarrow 2\pi^- \pi^+ 2\pi^0 \nu_\tau$ background events in the signal region.

All of the uncertainties described above are added in quadrature. The total number of expected $\tau$ background events in 232 $\mathrm{fb}^{-1}$ of data is $4.3 \pm 1.0$.

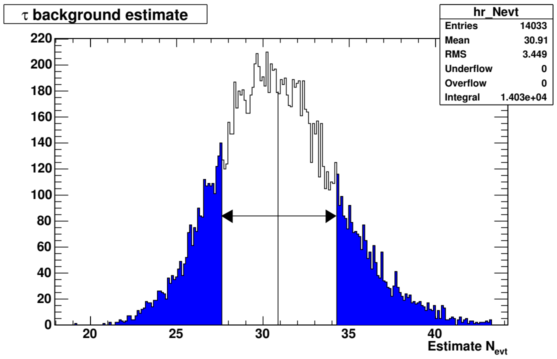

Figure 6.1: Distribution of the estimated number of $\tau$ background events (not normalized to data) in the data signal region. The colored portions correspond to 16% of the distribution. The arrows from the central value to the colored area correspond to $\pm 1\sigma$.

### 6.2.2 $q\overline{q}$ Background

The estimate of the $q\overline{q}$ background to $\tau^- \to 3\pi^-2\pi^+2\pi^0\nu_\tau$ and $\tau^- \to 4\pi^-3\pi^+(\pi^0)\nu_\tau$ analyses is extracted from fitting the $\tau$ pseudo-mass spectrum. The procedure of calculating the error on the estimate is described below for both analyses.

**$\tau^- \to 4\pi^-3\pi^+(\pi^0)\nu_\tau$**

The error on the $q\overline{q}$ background is a combination of errors from the fit parameters, the statistical error on the number of events fitted, and the systematic error from the fit range chosen. The uncertainty of the estimate introduced by the fit parameters is calculated similarly to the case of the $\tau$ background uncertainty in the $\tau^- \to 3\pi^-2\pi^+2\pi^0\nu_\tau$ analysis: using randomly generated fits of the pseudo-mass spectrum by varying the fit PDF shape parameters according to their errors. The uncertainty is then ±0.7 events.

To estimate the systematic error due to the fit range choice we vary the fit upper bound and see how the estimate changes. As it is seen from Table 6.2, the estimate change due to different fit ranges is small. We compare the "working" point of 2.6 GeV/c$^2$ with 20.3±0.7 estimated background events with the average counted from the table, which is 20.2. This leads to a systematic error of ±0.1 events.

| **Fit Upper Bound** | $\mathbf{N}_{bkg}$ |
|---|---|
| 2.45 | 19.8 ± 1.0 |
| 2.50 | 20.1 ± 0.9 |
| 2.55 | 20.4 ± 0.8 |
| 2.60 | 20.3 ± 0.7 |
| 2.65 | 20.6 ± 0.7 |
| 2.70 | 20.4 ± 0.6 |
| 2.75 | 20.3 ± 0.6 |

Table 6.2: The $q\overline{q}$ background estimate for inclusive $7\pi(\pi^0)$ mode using different fit ranges in 1-7 topology data.

Finally, the statistical uncertainty is calculated as a square-root of the number of events fitted, which yields ±0.4 events. All errors are added in quadrature and the total error of the $q\overline{q}$ background estimate is ±0.8 events.

### $\boldsymbol{\tau^- \longrightarrow 3\pi^-2\pi^+2\pi^0\nu_\tau}$

Similar to the $\tau^- \rightarrow 4\pi^-3\pi^+(\pi^0)\nu_\tau$ analysis, the $q\overline{q}$ background estimate is derived from the data, therefore no corrections or uncertainties due to tracking, particle ID, etc are applied. To calculate the statistical uncertainty of the $q\overline{q}$ background estimate we vary the number of events in each bin of the data $q\overline{q}$ pseudo-mass spectrum above 1.8 GeV/c$^2$ according to its Poisson error and refit the resulting histogram for a new estimate. The statistical uncertainty of $^{+1.6}_{-1.0}$ events is extracted from the variance of the distribution of the generated $q\overline{q}$ background estimates. Variations in the functional form of the fit PDF are taken into account as a systematic uncertainty of $^{+0.7}_{-0.0}$ events. The total uncertainty is calculated by adding the statistical and systematic uncertainties in quadrature. Thus, the $q\overline{q}$ background estimate is $2.2^{+1.7}_{-1.0}$ events.

### 6.2.3 Summary

The uncertainties of the $\tau$ and $q\overline{q}$ background estimates discussed above are summed up in Table 6.3 for $\tau^- \to 3\pi^-2\pi^+2\pi^0\nu_\tau$ and $\tau^- \to 4\pi^-3\pi^+(\pi^0)\nu_\tau$ analyses. The uncertainties are added in quadrature to obtain the total error of the background.

| | $\tau \to 5\pi 2\pi^0\nu_\tau$ | $\tau \to 7\pi(\pi^0)\nu_\tau$ |
|---|---|---|
| $\tau$ background | 4.3±1.0 | 1.3±1.0 |
| $q\overline{q}$ background | $2.2^{+1.7}_{-1.0}$ | 20.3±0.8 |
| Total background | $6.5^{+2.0}_{-1.4}$ | 21.6±1.3 |

Table 6.3: Summary table of the background estimates and uncertainties for $\tau^- \to 3\pi^-2\pi^+2\pi^0\nu_\tau$ and $\tau^- \to 4\pi^-3\pi^+(\pi^0)\nu_\tau$ analyses.

## 6.3 Uncertainty on the Number of $\tau$ Pairs

The uncertainty on the number of $\tau$ pairs produced is calculated from the uncertainty on the luminosity (1.1%) and the $\tau$-pair production cross section (2.2%). The total $N_{\tau^+\tau^-}$ uncertainty is 2.3% [24].

# CHAPTER 7

# RESULTS

## 7.1 $\tau^- \rightarrow 4\pi^-3\pi^+(\pi^0)\nu_\tau$

The 1-7 topology data pseudo-mass distribution above 1.8 GeV/c$^2$ was shown in Figure 5.2 for the 4 main selection steps. The data distribution below 1.8 GeV/c$^2$ was unblinded only after the background contributions and their uncertainties were estimated (see Table 6.3). Figure 7.1 illustrates the data distribution after all cuts. Out of 232 fb$^{-1}$ of data, 24 events have passed the selection criteria. Out of the 24 events, 7 had an identified electron on the tag side, 3 had a muon, 2 had a $\rho$ meson and 12 had a hadron. The number of observed events is consistent with the expected background of 21.6±1.3 events. No evidence for $\tau$ decays to 7 charged tracks is found. Table 7.1 compares the expected background and observed events for the 4 selection steps. Good agreement between the event numbers once again indicates the validity of the background estimate method performed in this analysis.

The upper limit calculation for the $\tau^- \rightarrow 4\pi^-3\pi^+(\pi^0)\nu_\tau$ decay branching ratio is based on the following likelihood function, which convolutes a Poisson distribution with two Gaussian resolution functions for the background and the efficiency, taking

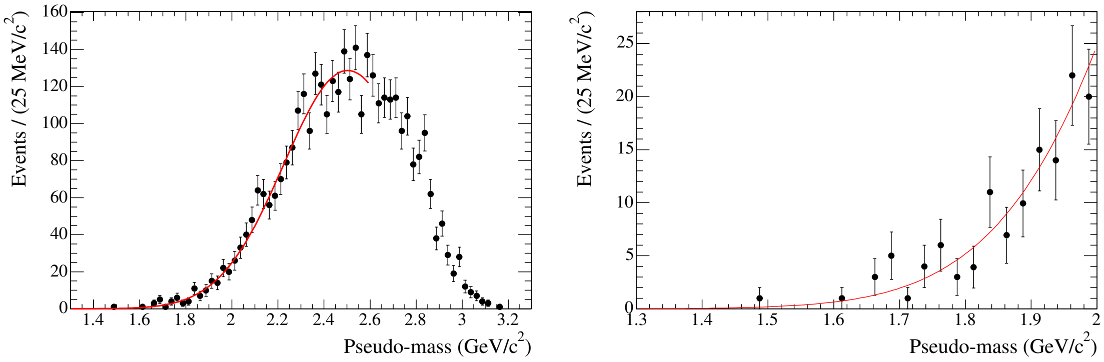

Figure 7.1: Final 1-7 topology data pseudo-mass distribution: the whole spectrum (left plot) and below 2.0 GeV/c$^2$ (right plot). Overlaid is the background extrapolation function.

| | $\tau$ bkg. | $q\overline{q}$ bkg. | Observed events |
|---|---|---|---|
| Pre-selection | $128 \pm 13$ | $574 \pm 21$ | 695 |
| Particle ID | $28 \pm 6$ | $241 \pm 10$ | 244 |
| Conversion Veto | $2.4 \pm 1.3$ | $119 \pm 5$ | 104 |
| 1-Prong Tag | $1.3 \pm 1.0$ | $20.3 \pm 0.8$ | 24 |

Table 7.1: Predicted and observed number of events in the signal region of $1.3 < M^* < 1.8\,\mathrm{GeV/c^2}$. The $\tau$ background yield is obtained from the MC simulation, while the $e^+e^- \to q\overline{q}$ yield is determined by fitting the data in the pseudo mass sideband.

into account their uncertainties:

$$\mathcal{L}(n,\hat{b},\hat{f};\mathcal{B},b,f) = \frac{\mu^n e^{-\mu}}{n!}\frac{1}{2\pi\sigma_b\sigma_f}e^{-\frac{1}{2}\left(\frac{\hat{b}-b}{\sigma_b}\right)^2-\frac{1}{2}\left(\frac{\hat{f}-f}{\sigma_f}\right)^2} \tag{7.1}$$

where $\mathcal{B}$ denotes the branching fraction of $\tau^- \to 4\pi^-3\pi^+(\pi^0)\nu_\tau$, $f = 2N_{\tau\tau}\epsilon$, $\epsilon$ is the signal efficiency, $b$ is the expected total background, $\mu = \langle n \rangle = f\mathcal{B} + b$, $n$ is the number of observed events, and $\hat{b}$ ($\hat{f}$) is sampled from a normal distribution $N(b, \sigma_b)$ ($N(f, \sigma_f)$). The number of $\tau$-pair events $N_{\tau\tau}$ is $(206.5 \pm 4.7) \times 10^6$. The errors on the number of $\tau$-pair events from luminosity and cross section, and efficiency are incorporated in $\sigma_f$.

The likelihood function is maximized with respect to the branching fraction $\mathcal{B}$, $\hat{f}$ and $\hat{b}$, and the following numerical value for the branching fraction is obtained by MINUIT [30]:

$$\mathcal{B}(\tau^- \to 4\pi^- 3\pi^+ (\pi^0)\nu_\tau) = (0.7^{+1.4}_{-1.3}) \times 10^{-7}. \tag{7.2}$$

Since there is no evidence for a signal we have computed a Bayesian upper limit using a uniform prior in the branching fraction, the background, and the efficiency. This is done by integrating out $\hat{f}$ and $\hat{b}$ in the likelihood function and plotting $\mathcal{L}$ as a function of $\mathcal{B}$. In this way we normalize the distribution to unity and get as the result of this analysis an upper limit at the point where the integral reaches 0.9:

$$\mathcal{B}(\tau^- \to 4\pi^- 3\pi^+ (\pi^0)\nu_\tau) < 3.0 \times 10^{-7} \text{ (at 90 \% CL)}. \tag{7.3}$$

With the same approach, setting the number of observed events $N_{obs}$ to the expected number of background events of $N_{exp} = 21.6$, we calculate the sensitivity of the analysis to be $\mathcal{B}^{N_{obs} \equiv N_{exp}}(\tau^- \to 4\pi^- 3\pi^+ (\pi^0)\nu_\tau) < 2.5 \times 10^{-7}$ at 90 % CL.

The result of the upper limit calculation with and without systematic uncertainties is plotted in Figure 7.2. If the uncertainties are neglected, the branching ratio upper limit drops down to $2.9 \times 10^{-7}$.

## 7.2 $\tau^- \to 3\pi^- 2\pi^+ 2\pi^0 \nu_\tau$

The 1-5 data pseudo-mass distribution above $1.8\,\text{GeV}/\text{c}^2$ after all the cuts was shown in Figure 5.5. The data distribution below $1.8\,\text{GeV}/\text{c}^2$ was unblinded only after the background contributions and their uncertainties were estimated (see Table 6.3). Figure 7.3 illustrates the unblinded data distribution. Out of $232\,\text{fb}^{-1}$ of

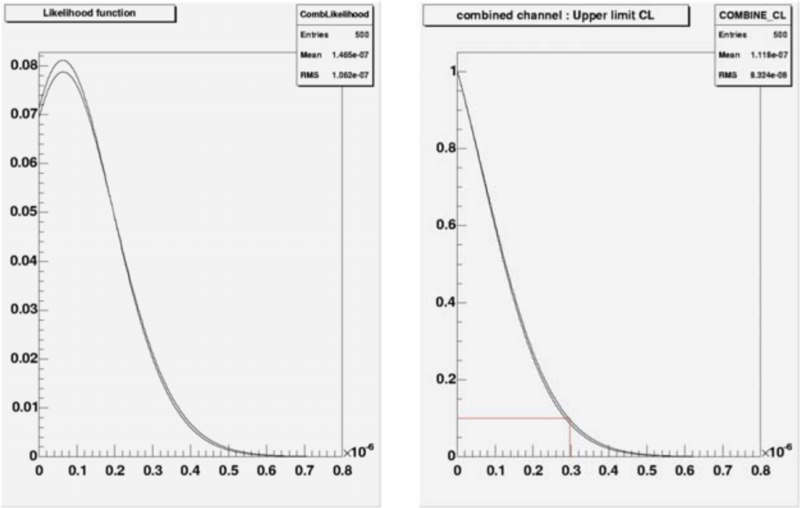

Figure 7.2: Branching ratio upper limit calculation. Left plot: likelihood function. Right plot: $\mathcal{B}$ upper limit: Upper curve shows the UL incorporating the systematic uncertainties. Lower curve shows UL neglecting the uncertainties.

data, 10 events passed the selection criteria. Out of the 10 events, 7 had an identified electron on the tag side and 3 had a muon. The observation of 10 events in the data is consistent with the expected background of $6.5^{+2.0}_{-1.4}$ events. No evidence for $\tau$ decays to 5 charged and 2 neutral pions in $232\,\mathrm{fb}^{-}1$ was found.

The upper limit for the $\tau^- \to 3\pi^- 2\pi^+ 2\pi^0 \nu_\tau$ decay branching ratio is calculated using the following expression:

$$\mathcal{B}(\tau^- \to 3\pi^- 2\pi^+ 2\pi^0 \nu_\tau) < \frac{\lambda_{N_{signal}}}{2 \times N_{\tau\tau} \times \epsilon} \tag{7.4}$$

where $\lambda_{N_{signal}}$ is the upper limit of the number of signal events at the 90% confidence level. This number is obtained using a limit calculator program written by R. Barlow [31], that follows the Cousins and Highland approach [32] of incorporating systematic uncertainties into the upper limit, using the observed $N_{obs}$ and expected

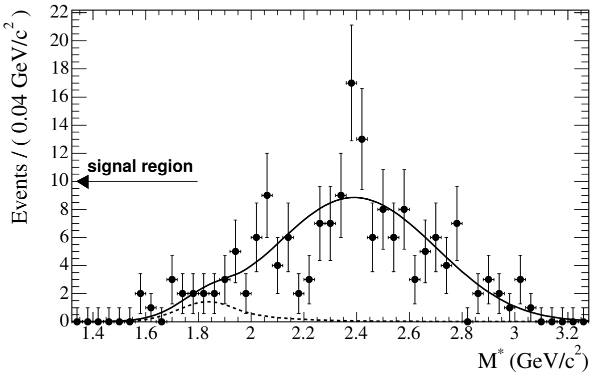

Figure 7.3: Pseudo-mass M$^*$ distribution of the data events passing the $\tau^- \rightarrow 3\pi^- 2\pi^+ 2\pi^0 \nu_\tau$ selection criteria. The solid curve represents the total expected background PDF. The dashed curve illustrates the $\tau$ background contribution.

$N_{exp}$ number of events, as well as the uncertainties on $N_{exp}$ and signal efficiency. The denominator of equation 7.4 is called the sensitivity $S$. The uncertainty on $N_{\tau\tau}$ together with the uncertainty on the signal efficiency is the uncertainty on the sensitivity $\sigma_S$ and is included in the upper limit calculation. The advantage of the calculator is its ability to include the asymmetric errors.

The method uses a Monte Carlo technique for evaluation of the confidence intervals. A trial value for the limit $\lambda_{N_{signal}}$ is taken and assumed to be from a Gaussian together with the expected number of background events $N_{exp}$. For simplification, the sensitivity $S$ is taken to be 1, and the error $\sigma_S$ contains the errors on the signal efficiency and luminosity. The $\lambda_{N_{signal}}$ and $N_{exp}$ are repeatedly varied by their standard deviations $\sigma_S$ and $\sigma_{N_{exp}}$, and a Poisson distribution of the number of observed events with mean ($\lambda_{N_{signal}}$+$N_{exp}$) is created. The trial value for the limit is then varied until 10% of the trial sample events are less than $N_{obs}$ events in data. This yields $\lambda_{N_{signal}}$=9.2, which is then plugged into expression 7.4 for the branching ratio upper limit calculation:

$$\mathcal{B}(\tau^- \to 3\pi^-2\pi^+2\pi^0\nu_\tau) < 3.4 \times 10^{-6} \text{ (at 90 \% CL).} \tag{7.5}$$

The branching ratio sensitivity is obtained by setting the number of observed events $N_{obs}$ to the expected number of background events, which yields $\lambda_{N_{signal}}$=4.9, and $\mathcal{B}^{N_{obs}\equiv N_{exp}}(\tau^- \to 3\pi^-2\pi^+2\pi^0\nu_\tau) < 1.8 \times 10^{-6}$ at 90 % CL.

## 7.3 Summary

The results are summarized in Table 7.2. The upper limit for the $\tau^- \to 3\pi^-2\pi^+2\pi^0\nu_\tau$ decay branching ratio is more than 30 times smaller than the current upper limit established by the CLEO Collaboration. The upper limit for the $\tau^- \to 4\pi^-3\pi^+(\pi^0)\nu_\tau$ decay branching ratio is approximately an order of magnitude times smaller than the current upper limit. Both are significant improvements over the currently published limits, and hopefully will provide more insights into the decay dynamics of the multi-hadron decays of the $\tau$ lepton.

| | $\boldsymbol{\tau^- \to 3\pi^-2\pi^+2\pi^0\nu_\tau}$ | $\boldsymbol{\tau^- \to 4\pi^-3\pi^+(\pi^0)\nu_\tau}$ |
|---|---|---|
| $N_{\tau\tau}$ | $(206.5 \pm 4.7) \times 10^6$ | $(206.5 \pm 4.7)\times 10^6$ |
| $e^+e^- \to \tau^+\tau^-$ background | $4.3 \pm 1.0$ | $1.3 \pm 1.0$ |
| $e^+e^- \to q\overline{q}$ background | $2.2^{+1.7}_{-1.0}$ | $20.3 \pm 0.8$ |
| Total background | $6.5^{+2.0}_{-1.4}$ | $21.6 \pm 1.3$ |
| Signal efficiency | $(0.66 \pm 0.05)$ % | $(9.35 \pm 0.55)$ % |
| $\mathcal{B}$ sensitivity (90% CL) | $1.8 \times 10^{-6}$ | $2.5 \times 10^{-7}$ |
| $\mathcal{B}$ upper limit (90% CL) | $3.4 \times 10^{-6}$ | $3.0 \times 10^{-7}$ |

Table 7.2: Number of $\tau$-pairs analyzed, expected $\tau$ and $q\overline{q}$ background estimates, the $\tau^- \to 4\pi^-3\pi^+(\pi^0)\nu_\tau$ signal efficiency yield, the decay branching ratio sensitivities and upper limits for $\tau^- \to 3\pi^-2\pi^+2\pi^0\nu_\tau$ and $\tau^- \to 4\pi^-3\pi^+(\pi^0)\nu_\tau$ analyses.

# CHAPTER 8

# EXCLUSIVE DECAY CHANNELS

Both the $\tau^- \to 4\pi^-3\pi^+(\pi^0)\nu_\tau$ and $\tau^- \to 3\pi^-2\pi^+2\pi^0\nu_\tau$ decay modes are inclusive. In the $\tau^- \to 4\pi^-3\pi^+(\pi^0)\nu_\tau$ analysis, we did not require a reconstructed $\pi^0$ on the signal side, neither did we reject it. In the $\tau^- \to 3\pi^-2\pi^+2\pi^0\nu_\tau$ analysis we did not search for any particular resonance mode through which the decay may possibly go. This chapter contains studies of the following exclusive channels:

- $\tau^- \to 4\pi^-3\pi^+\nu_\tau$
- $\tau^- \to 4\pi^-3\pi^+\pi^0\nu_\tau$
- $\tau^- \to 2\omega\pi^-\nu_\tau$, $\omega \to \pi^-\pi^+\pi^0$

There are no previously reported measurements or limits established for these modes.

## 8.1 $\tau^- \to 4\pi^-3\pi^+\nu_\tau$

To select $\tau^- \to 4\pi^-3\pi^+\nu_\tau$ events, no photons are allowed on the signal side. This requirement reduces the background from $e^+e^- \to q\overline{q}$ processes, as well as the potential background from the $\tau^- \to 4\pi^-3\pi^+\pi^0\nu_\tau$ mode. All other selection criteria and background estimate methods remain identical to the inclusive analysis. Figure 8.1 illustrates the data pseudo-mass spectrum after all cuts. The results are shown in Table 8.1. The upper limit calculation is identical to the inclusive analysis, and takes into account the errors on the expected background and signal efficiency. The difference of almost a factor of 2 between the sensitivity and the upper limit, shown in the table, is due to the overestimate of the expected background.

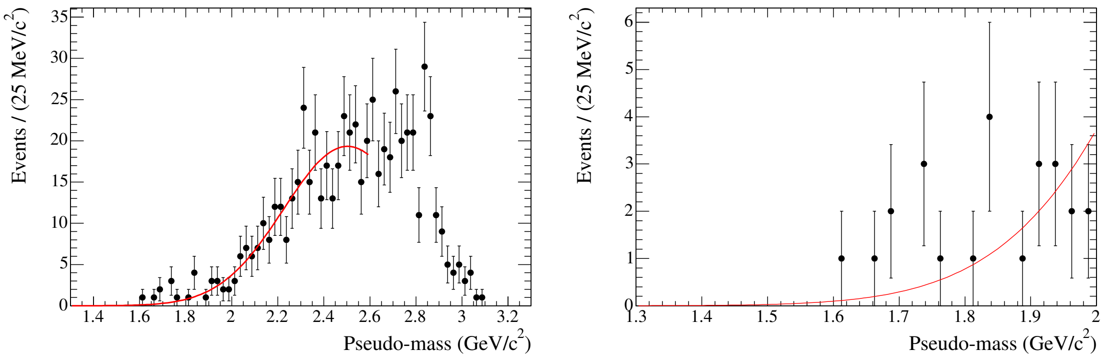

Figure 8.1: Data pseudo-mass distribution for the $\tau^- \to 4\pi^- 3\pi^+ \nu_\tau$ events: the whole spectrum (left plot) and below $2.0\,\mathrm{GeV/c^2}$ (right plot). Overlaid is the background extrapolation function.

## 8.2 $\tau^- \longrightarrow 4\pi^- 3\pi^+ \pi^0 \nu_\tau$

For this mode a $\pi^0$ needs to be reconstructed on the signal side. Reconstruction of a $\pi^0$ is done by demanding two photon candidates on the 7-prong side that have an invariant mass between 113 and $155\,\mathrm{MeV/c^2}$, which is the $3\sigma$ range of a Gaussian fit to the $\pi^0$ mass spectrum. This requirement rejects possible background from the $\tau^- \to 4\pi^- 3\pi^+ \nu_\tau$ mode. Apart from demanding one reconstructed $\pi^0$ on the signal

| | |
|---|---|
| $e^+e^- \rightarrow \tau^+\tau^-$ background | $0.8 \pm 0.8$ |
| $e^+e^- \rightarrow q\overline{q}$ background | $3.1 \pm 0.1$ |
| Total background | $3.9 \pm 0.8$ |
| $\tau^- \rightarrow 4\pi^-3\pi^+\nu_\tau$ efficiency % | $5.46 \pm 0.33$ |
| $\tau^- \rightarrow 4\pi^-3\pi^+\pi^0\nu_\tau$ efficiency % | $0.81 \pm 0.05$ |
| Sensitivity $\mathcal{B}(\tau^- \rightarrow 4\pi^-3\pi^+\nu_\tau)$ (90% CL) | $2.2 \times 10^{-7}$ |
| Upper limit $\mathcal{B}(\tau^- \rightarrow 4\pi^-3\pi^+\nu_\tau)$ (90% CL) | $4.3 \times 10^{-7}$ |

Table 8.1: Expected $\tau$ and $q\overline{q}$ background estimates, signal efficiency yield, the $\tau^- \rightarrow 4\pi^-3\pi^+\nu_\tau$ decay branching ratio sensitivity and upper limit.

side, all other selection criteria and background estimate methods remain identical to the inclusive analysis.

Figure 8.2 shows the data pseudo-mass spectrum for 1-7 topology events with 1 reconstructed $\pi^0$ on the signal side. The observation of 7 events in 232 $\text{fb}^{-1}$ of data is consistent with the expected background of 8.2±0.5 events. No evidence for a $\tau^- \rightarrow 4\pi^-3\pi^+\pi^0\nu_\tau$ signal was found. The results are summarized in Table 8.2.

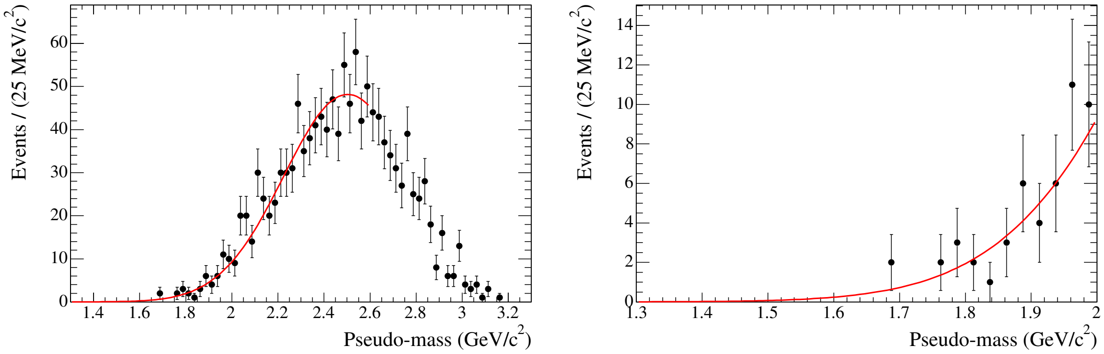

Figure 8.2: Data pseudo-mass distribution for the $\tau^- \rightarrow 4\pi^-3\pi^+\pi^0\nu_\tau$ events: the whole spectrum (left plot) and below 2.0 GeV/c$^2$ (right plot). Overlaid is the background extrapolation function.

| | |
|---|---|
| $e^+e^- \to \tau^+\tau^-$ background | $0.4 \pm 0.4$ |
| $e^+e^- \to q\overline{q}$ background | $7.8 \pm 0.3$ |
| Total background | $8.2 \pm 0.5$ |
| $\tau^- \to 4\pi^-3\pi^+\nu_\tau$ efficiency % | $0.31 \pm 0.03$ |
| $\tau^- \to 4\pi^-3\pi^+\pi^0\nu_\tau$ efficiency % | $3.60 \pm 0.34$ |
| Sensitivity $\mathcal{B}(\tau^- \to 4\pi^-3\pi^+\pi^0\nu_\tau)$ (90% CL) | $4.2 \times 10^{-7}$ |
| Upper limit $\mathcal{B}(\tau^- \to 4\pi^-3\pi^+\pi^0\nu_\tau)$ (90% CL) | $2.5 \times 10^{-7}$ |

Table 8.2: Expected $\tau$ and $q\overline{q}$ background estimates, signal efficiency yield, the $\tau^- \to 4\pi^-3\pi^+\pi^0\nu_\tau$ decay branching ratio sensitivity and upper limit.

## 8.3 $\tau^- \to 2\omega\pi^-\nu_\tau$

According to isospin model calculations [17], the $\tau^- \to 2\omega\pi^-\nu_\tau$ mode, with a subsequent decay of $\omega \to \pi^-\pi^+\pi^0$, is predicted to be the dominant channel for the $\tau^- \to 3\pi^-2\pi^+2\pi^0\nu_\tau$ decay. The search for the exclusive $\tau^- \to 2\omega\pi^-\nu_\tau$ decay may allow us to reach the sensitivity of the $10^{-7}$ order.

A MC signal sample of 120000 $\tau^- \to 2\omega\pi^-\nu_\tau$ events is generated and passed through the same pre-selection criteria described in section 3.3. We also generated 114000 $\tau^- \to \omega2\pi^-\pi^+\nu_\tau$ events (corresponding to $530\,\mathrm{fb}^{-1}$), since the generic $\tau$ sample does not contain this decay mode. This is expected to be the dominant background for the $\tau^- \to 2\omega\pi^-\nu_\tau$ signal.

Figure 8.3 compares the pseudo-mass distribution of $\tau^- \to 2\omega\pi^-\nu_\tau$ and $\tau^- \to 3\pi^-2\pi^+2\pi^0\nu_\tau$ MC events after the pre-selection. As expected, the $\tau^- \to 2\omega\pi^-\nu_\tau$ mode has a much narrower mass range due to its kinematical constraints. Table 8.3 compares the efficiencies of the modes $\tau^- \to 2\omega\pi^-\nu_\tau$ and $\tau^- \to 3\pi^-2\pi^+2\pi^0\nu_\tau$.

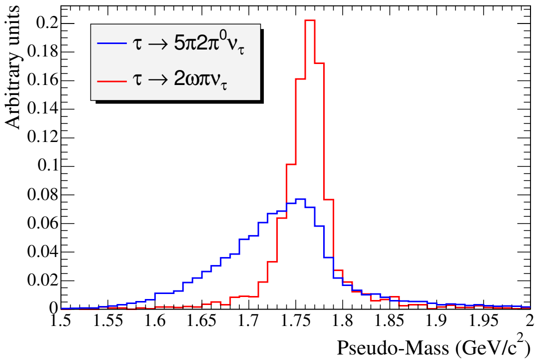

Figure 8.3: The pseudo-mass spectra of the $\tau^- \rightarrow 2\omega\pi^-\nu_\tau$ (red) and $\tau^- \rightarrow 3\pi^-2\pi^+2\pi^0\nu_\tau$ (blue) MC samples after the pre-selection.

| **Cuts** | $\boldsymbol{\tau^- \rightarrow 3\pi^-2\pi^+2\pi^0\nu_\tau}$ | $\boldsymbol{\tau^- \rightarrow 2\omega\pi^-\nu_\tau}$ |
|---|---|---|
| Pre-selection | 3.5±0.3% | 3.9±0.3% |
| 1-prong tags | 2.0±0.2% | 2.2±0.2% |
| Pion ID | 1.8±0.2% | 2.0±0.2% |
| Conversion veto | 1.4±0.1% | 1.6±0.2% |
| Pseudo-Mass | 1.3±0.1% | 1.5±0.1% |

Table 8.3: MC efficiencies of $\tau^- \rightarrow 3\pi^-2\pi^+2\pi^0\nu_\tau$ and $\tau^- \rightarrow 2\omega\pi^-\nu_\tau$ modes throughout the cuts. No reconstruction of the $\omega$ is done at this point.

The event selection was re-optimized for this analysis. The photon and $\pi^0$ selection criteria are loosened to be:

- $E_\gamma > 50\,\mathrm{MeV}$
- $N_{crystal} > 1$
- LAT $< 0.6$
- $E_{\pi^0} > 200\,\mathrm{MeV}$

Omegas are reconstructed from the $\omega \to \pi^-\pi^+\pi^0$ decay. Figure 8.4 (left plot) shows the invariant mass of all combinations of two oppositely charged tracks and a reconstructed $\pi^0$. Any combination not pointing to a true $\omega$ (from MC truth) is referred to as a non-$\omega$ combination. The right plot shows the invariant mass of the reconstructed $\omega$'s within the 0.70-0.86 GeV/c$^2$ range. The shape of the $\omega$ resonance is well-simulated (see Figure 8.5). To retain the $\omega$ meson, we require $0.76 < M_\omega < 0.80\,\mathrm{GeV/c^2}$. The relative efficiency of the selected signal events with both $\omega$'s reconstructed is 8.2%, while the purity of the $2\omega$ selection is 87%.

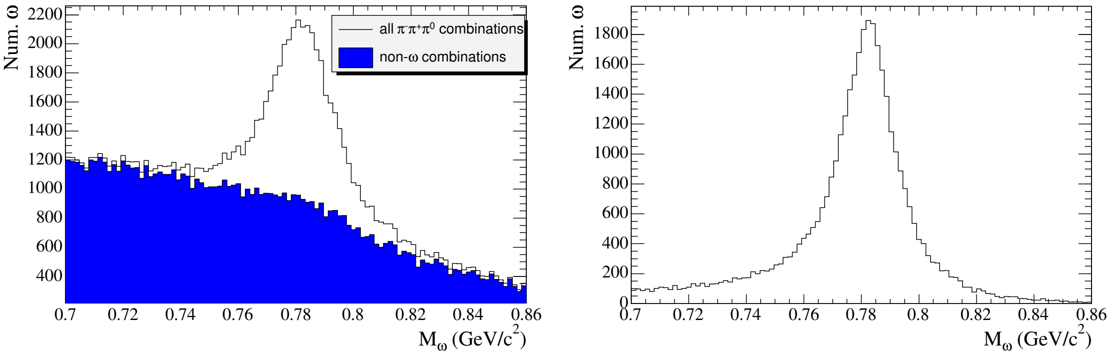

Figure 8.4: Left plot: Invariant mass distribution of all combinations of oppositely charged tracks and a reconstructed $\pi^0$ (white histogram) and non-omega combinations that are not from a true omega (blue filled histogram). Right plot: Invariant mass of the reconstructed omegas.

Reconstruction of both $\omega$ mesons effectively suppresses the background, and therefore further selection cuts can be substantially loosened to increase the signal efficiency. The conversion veto and residual neutral energy cuts are dropped from the event selection. In addition, hadrons are allowed on the tag side, and only loose pion identification is required on the signal side. Table 8.4 shows the signal efficiency and

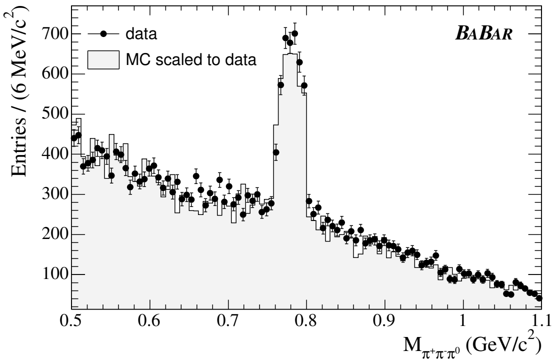

Figure 8.5: Invariant mass distribution of all $\pi^+\pi^-\pi^0$ combinations in data and MC. MC distribution consists of $\tau$ events scaled to the data luminosity and $q\overline{q}$ events scaled to the number of $\tau$-subtracted data events. The peak illustrates the $\omega$ mesons.

the background level throughout the cuts. We successfully suppress the background and keep the signal efficiency level higher than in the $\tau^- \to 3\pi^-2\pi^+2\pi^0\nu_\tau$ analysis. The sources and values of the systematic uncertainties to the signal efficiency are not different from the inclusive analysis (see Table 6.1), since we use the same variables for the event selection in both analysis. We do not include additional uncertainty due to the omega reconstruction, since it is based on the pion ID and $\pi^0$ reconstruction uncertainties, already taken into account. The only difference is the statistical uncertainty due to different sample sizes used.

The background is estimated from Monte Carlo simulation (see Figure 8.6). Despite the quantitative discrepancy between the data and MC $q\overline{q}$, the scaled MC $q\overline{q}$ pseudo-mass spectrum agrees with the data within the errors. The pseudo-mass distribution of the $q\overline{q}$ background does not suggest any tail, which is explained by the kinematical suppression below 1.7 GeV/c$^2$. We expect no $q\overline{q}$ contribution in the signal region of 232 fb$^{-1}$ of data. The uncertainty in zero $q\overline{q}$ background events was

| **Cuts applied** | gen. $\tau$ | $\tau^- \to \omega 2\pi^-\pi^+\nu_\tau$ | $q\overline{q}$ | signal (%) |
|---|---|---|---|---|
| Pre-selection | 2596 | 262 | 91566 | 7.0±0.6 |
| Reconstruction of $2\omega$ | 124 | 25 | 6684 | 2.6±0.2 |
| 1-prong tags | 83 | 19 | 1408 | 1.8±0.2 |
| Loose $\pi$ ID (signal side) | 23 | 16 | 701 | 1.6±0.2 |
| $1.7 < M^* < 1.8\,\mathrm{GeV/c^2}$ | 0 | 0.4 | 0 | 1.53±0.13 |

Table 8.4: Effect of the cuts applied to MC signal and background. All background samples are scaled to $232\,\mathrm{fb}^{-1}$ data luminosity. Generic $\tau$ background does not contain the $\tau^- \to \omega 2\pi^-\pi^+\nu_\tau$ mode, it is considered separately. Signal efficiency is given in (%), the background is shown in number of events (normalized).

calculated using the same technique described for the inclusive $\tau^- \to 3\pi^- 2\pi^+ 2\pi^0 \nu_\tau$ analysis. As a result, the total expected $q\overline{q}$ background is $0.0^{+0.1}_{-0.0}$ events.

As a cross-check, we repeat the procedure described in section 5.2.2, requiring at least 3 high-energy photons ($E_\gamma > 500\,\mathrm{MeV}$), not associated with a $\pi^0$, on the tag side. This suppresses the possible signal and $\tau$ events, allowing to unblind the data and compare it with MC. The remaining $q\overline{q}$ pseudo-mass spectrum is shown in Figure 8.7 for the data and MC. As expected, there is no tail below $1.8\,\mathrm{GeV/c^2}$, and the scaled MC agrees with the data (2.0±1.7 $q\overline{q}$ events predicted by MC in the signal region, no events observed in the data). We conclude, that the $q\overline{q}$ MC scaled to the data is reasonable for the background estimate.

The only background contribution comes from the $\tau^- \to \omega 2\pi^-\pi^+\nu_\tau$ mode. Out of $530\,\mathrm{fb}^{-1}$ of MC simulated $\tau^- \to \omega 2\pi^-\pi^+\nu_\tau$ events, only 1 was found in the signal region, which corresponds to $0.4^{+1.0}_{-0.4}$ events in $232\,\mathrm{fb}^{-1}$ of data. The uncertainty in the $\tau$ background estimate is calculated as a Poisson error of 1 event at 68% confidence level, scaled down by a MC/data scaling factor.

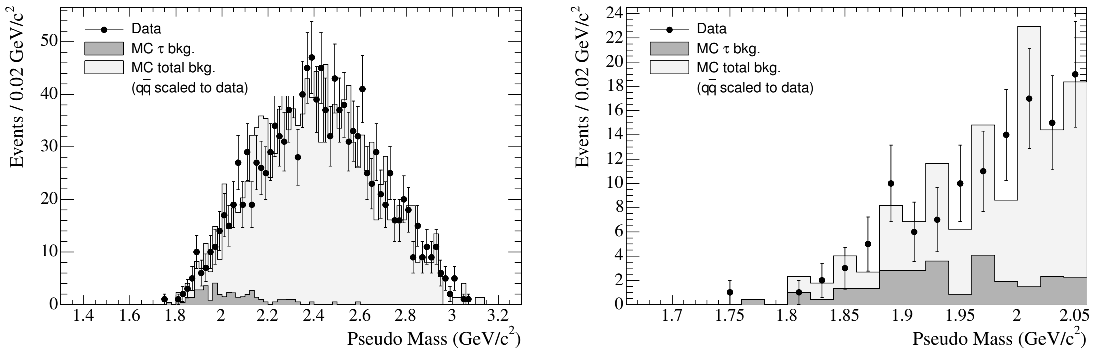

Figure 8.6: Pseudo-mass distributions of the data (points) and MC (shaded plots) events in the whole range (left) and below 2.0 GeV/c$^2$ (right plot) passing the selection criteria. Dark shaded plot corresponds to the Monte Carlo $\tau$ background scaled to the data luminosity. Light shaded plot corresponds to the $\tau$ and $q\overline{q}$ Monte Carlo backgrounds combined, where the $q\overline{q}$ Monte Carlo is normalized by a data/MC factor. The data signal region below 1.8 GeV/c$^2$ was blinded during the background estimation.

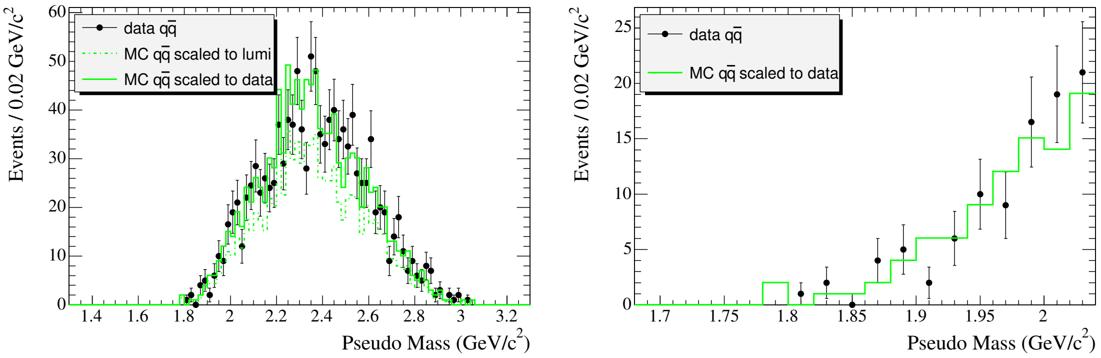

Figure 8.7: Pseudo-mass distributions of the "signal-free" unblinded data and MC $q\overline{q}$ scaled to the data luminosity (green dashed line) and to the data spectrum (green solid line). Right plot: Pseudo mass distribution between 1.7 and 2.0 GeV/c$^2$.

Out of 232 fb$^{-1}$ of data, 1 event (see Figure 8.6) passed the selection criteria, which is consistent with the expected background of $0.4^{+1.0}_{-0.4}$ events. We did not find any evidence for the $\tau^- \to 2\omega\pi^-\nu_\tau$ decay, and calculated the branching ratio upper limit at 90% confidence level using the limit calculator [31]. Due to the higher signal efficiency and lower background level, the upper limit for the $\tau^- \to 2\omega\pi^-\nu_\tau$ decay is almost 6 times lower than for the inclusive $\tau^- \to 3\pi^-2\pi^+2\pi^0\nu_\tau$ decay mode. Table 8.5 summarizes the results of the $\tau^- \to 2\omega\pi^-\nu_\tau$ search. Hypothetical $\tau^- \to 2\omega\pi^-\nu_\tau$ signal is plotted in Figure 8.8, assuming the decay branching ratio of $10^{-6}$ and $5 \times 10^{-7}$.

| $N_{\tau\tau}$ | $(206.5 \pm 4.7) \times 10^6$ |
|---|---|
| $\tau^- \to 2\omega\pi^-\nu_\tau$ efficiency | $(1.53 \pm 0.13)\%$ |
| Expected $\tau^+\tau^-$ background | $0.4^{+1.0}_{-0.4}$ |
| Expected $q\overline{q}$ background | $0.0^{+0.1}_{-0.0}$ |
| Expected total background | $0.4^{+1.0}_{-0.4}$ |
| Observed events | 1 |
| $\mathcal{B}(\tau^- \to 2\omega\pi^-\nu_\tau)$ (90% CL) | $< 5.4 \times 10^{-7}$ |

Table 8.5: Expected background, observed data events, signal efficiency and the upper limit of the $\tau^- \to 2\omega\pi^-\nu_\tau$ decay at 90% confidence level.

## 8.4 Summary

We have searched for exclusive 5-prong and 7-prong $\tau$ decays involving $\omega$ resonances and neutral pions. No evidence for a signal was found, and the upper limits

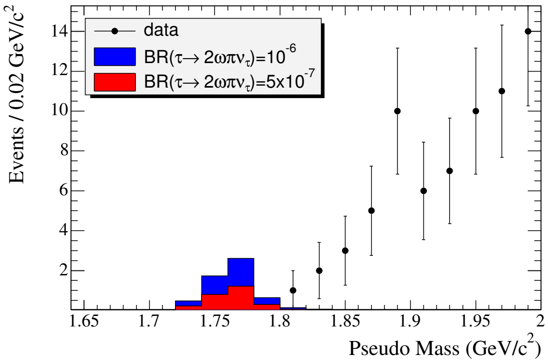

Figure 8.8: Predicted pseudo-mass spectrum of the $\tau^- \to 2\omega\pi^-\nu_\tau$ mode in $232\,\mathrm{fb}^{-1}$ of data for $\mathcal{B}(\tau^- \to 2\omega\pi^-\nu_\tau) = 10^{-6}$ (blue) and $\mathcal{B}(\tau^- \to 2\omega\pi^-\nu_\tau) = 5 \times 10^{-7}$ (red).

at 90% confidence level were calculated for the exclusive modes, summarized in Table 8.6. The limits are consistent with the inclusive analyses of $\tau^- \to 3\pi^-2\pi^+2\pi^0\nu_\tau$ and $\tau^- \to 4\pi^-3\pi^+(\pi^0)\nu_\tau$ decays.

| | |
|---|---|
| $\mathcal{B}(\tau^- \to 4\pi^-3\pi^+\nu_\tau)$ | $< 4.3 \times 10^{-7}$ |
| $\mathcal{B}(\tau^- \to 4\pi^-3\pi^+\pi^0\nu_\tau)$ | $< 2.5 \times 10^{-7}$ |
| $\mathcal{B}(\tau^- \to 2\omega\pi^-\nu_\tau)$ | $< 5.4 \times 10^{-7}$ |

Table 8.6: Upper limits for the $\tau^- \to 4\pi^-3\pi^+\nu_\tau$, $\tau^- \to 4\pi^-3\pi^+\pi^0\nu_\tau$ and $\tau^- \to 2\omega\pi^-\nu_\tau$ exclusive decay branching ratios at 90% confidence level.

# CHAPTER 9

# MEASUREMENT OF THE $\tau^- \rightarrow 3\pi^- 2\pi^+ \pi^0 \nu_\tau$ DECAY BRANCHING RATIO

The $\tau^- \rightarrow 3\pi^- 2\pi^+ \pi^0 \nu_\tau$ decay has already been observed by several experiments with an average branching ratio of $(1.81 \pm 0.27) \times 10^{-4}$ [6], but has never been measured at *BABAR*. This inclusive multi-pion mode is the closest observed decay to our 7-pion searches. A branching ratio measurement of the $\tau^- \rightarrow 3\pi^- 2\pi^+ \pi^0 \nu_\tau$ mode consistent with the PDG value will validate our event selection criteria and the background estimate method. We keep the event selection criteria identical to the $\tau^- \rightarrow 3\pi^- 2\pi^+ 2\pi^0 \nu_\tau$ analysis (except for reconstructing only one $\pi^0$ instead of two on the signal side) and use the same background estimate method.

Figure 9.1 (left plot) shows the pseudo-mass of the signal $\tau^- \rightarrow 3\pi^- 2\pi^+ \pi^0 \nu_\tau$ mode and the background from generic $\tau$ events, which are dominated by the $\tau^- \rightarrow 3\pi^- 2\pi^+ \nu_\tau$ decays. Monte Carlo is used to estimate the $\tau$ background in the signal region. The generic $\tau$ pseudo-mass spectrum is fitted with a 'Crystal Ball' PDF, and the $\tau^- \rightarrow 3\pi^- 2\pi^+ \pi^0 \nu_\tau$ spectrum is fitted with an exponential in the 1.8-3.3 GeV/c$^2$ range. A total of 67±9 $\tau$ background events are expected in the signal region. Both PDFs are added and the total PDF is shown in Figure 9.1 (right plot) superimposed on the total $\tau$ distribution above the signal region.

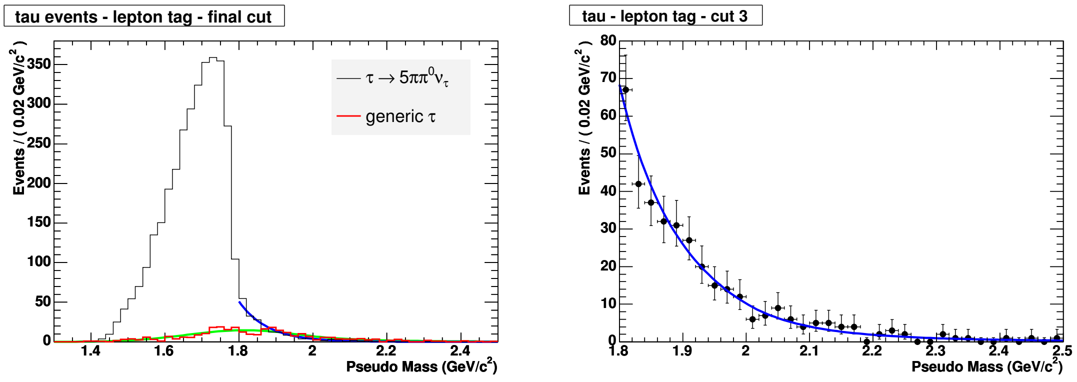

Figure 9.1: Left plot: MC pseudo-mass distributions and the fits of the $\tau^- \to 3\pi^- 2\pi^+ \pi^0 \nu_\tau$ and generic $\tau$ events. Green curve corresponds to the 'Crystal Ball' PDF used to fit the generic $\tau$ spectrum. Blue curve is an exponential fit of the signal mode above the signal region. Right plot: total MC $\tau$ distribution above the signal region and the corresponding PDF.

Similar to the $\tau^- \to 3\pi^- 2\pi^+ \pi^0 \nu_\tau$ analysis, the $uds$ and $c\overline{c}$ distributions are fitted separately and the combined PDF obtained from MC is used to fit the data. Figure 9.2 shows the $uds$ pseudo-mass distribution fitted with a Gaussian below 2.5 GeV/c$^2$, and the pseudo-mass distribution of the $c\overline{c}$ events fitted with a double Gaussian PDF, where one of the Gaussians with the central value at 2.1 GeV/c$^2$ is presumably due to the multi-pion decays of the $D^*$. In both cases, the fits successfully describe the background in the signal region.

The sum of the $uds$ and $c\overline{c}$ PDFs is used to fit the data $q\overline{q}$ spectrum obtained by subtracting the $\tau$ distribution from the data. Similarly to the fitting procedure described in section 5.2.2, we let the shape parameters float within a certain range and use the MC $q\overline{q}$ PDF to fit the data above the signal region. The fit is then extrapolated below 1.8 GeV/c$^2$ for the $q\overline{q}$ background estimate. The resulting spectra are shown in Figure 9.3, along with the corresponding MC and data fits. The $q\overline{q}$

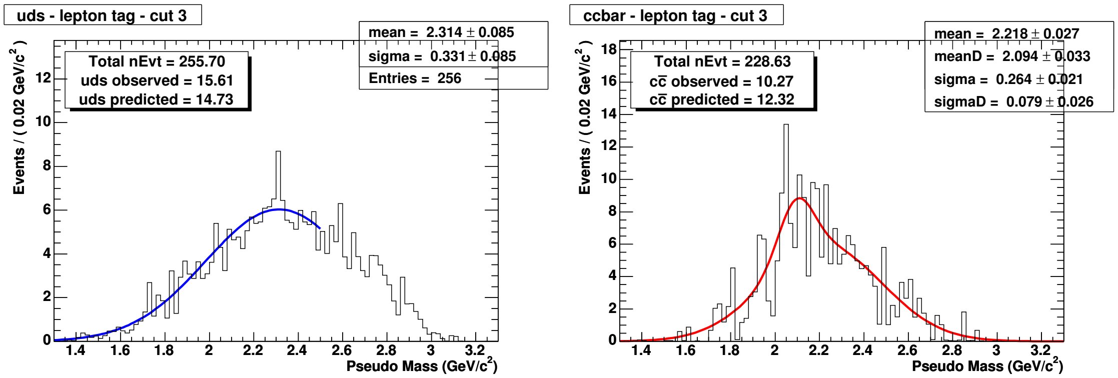

Figure 9.2: MC pseudo-mass distribution of the *uds* events (left plot) fitted with a Gaussian below 2.5 GeV/c$^2$, and $c\overline{c}$ events fitted with a double Gaussian PDF. Numbers in the result boxes show the background expected from the fitting procedure and background events counted in the signal region of the pseudo-mass distribution.

background estimates from both the MC and data fits are also shown in the plot. After estimating the $\tau$ and $q\overline{q}$ backgrounds expected in the signal region, we have unblinded the data spectrum (see Figure 9.4).

Using the signal events extracted from the data by subtracting the expected $\tau$ and $q\overline{q}$ backgrounds in the signal region, we compare the properties of reconstructed $\pi^0$'s in data and MC (see Figure 9.5). The agreement is a good sign of a correct $\pi^0$ reconstruction and modeling in the MC.

The final results are shown in Table 9.1. The origin of the systematic uncertainties of the $\tau$ background were explained in section 6.2.1. The systematic uncertainty of the $q\overline{q}$ background estimate is set to the difference between the MC and data fit yields. This is probably an overestimate, but since we do not aim for a precision measurement, a rough estimate will do here.

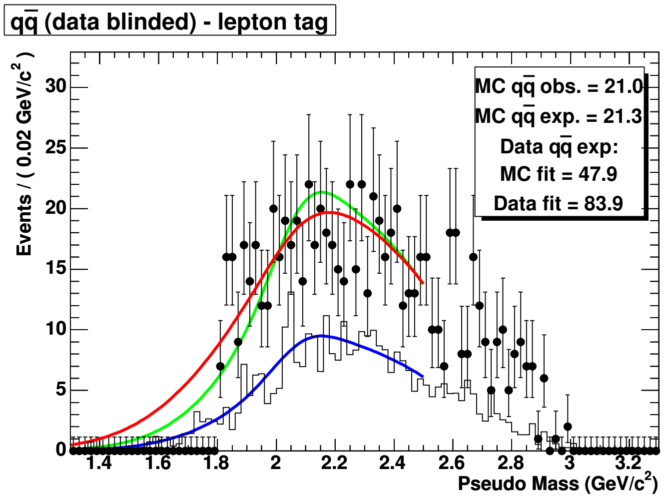

Figure 9.3: The histogram represents the MC $q\overline{q}$ pseudo-mass distribution normalized to the data luminosity. Data points are the $q\overline{q}$ data, blinded below 1.8 GeV/c$^2$. The blue curve is the $q\overline{q}$ PDF superimposed on the MC $q\overline{q}$ distribution. The green curve is the same PDF normalized by the data $q\overline{q}$ distribution. The red curve is a data fit with MC $q\overline{q}$ PDF, allowing the PDF shape parameters float. The statistics box shows the number of background events counted and estimated from the blue, green and red fits in the signal region.

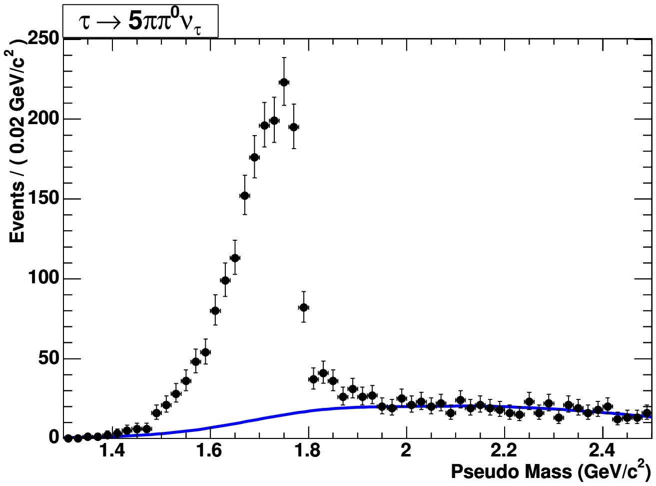

Figure 9.4: Pseudo-mass distribution of the data after the $\tau^- \to 3\pi^-2\pi^+\pi^0\nu_\tau$ event selection, illustrating a clear $\tau^- \to 3\pi^-2\pi^+\pi^0\nu_\tau$ signal. The expected total background PDF, a combination of the $\tau$ and $q\overline{q}$ PDFs, is represented by the curve.

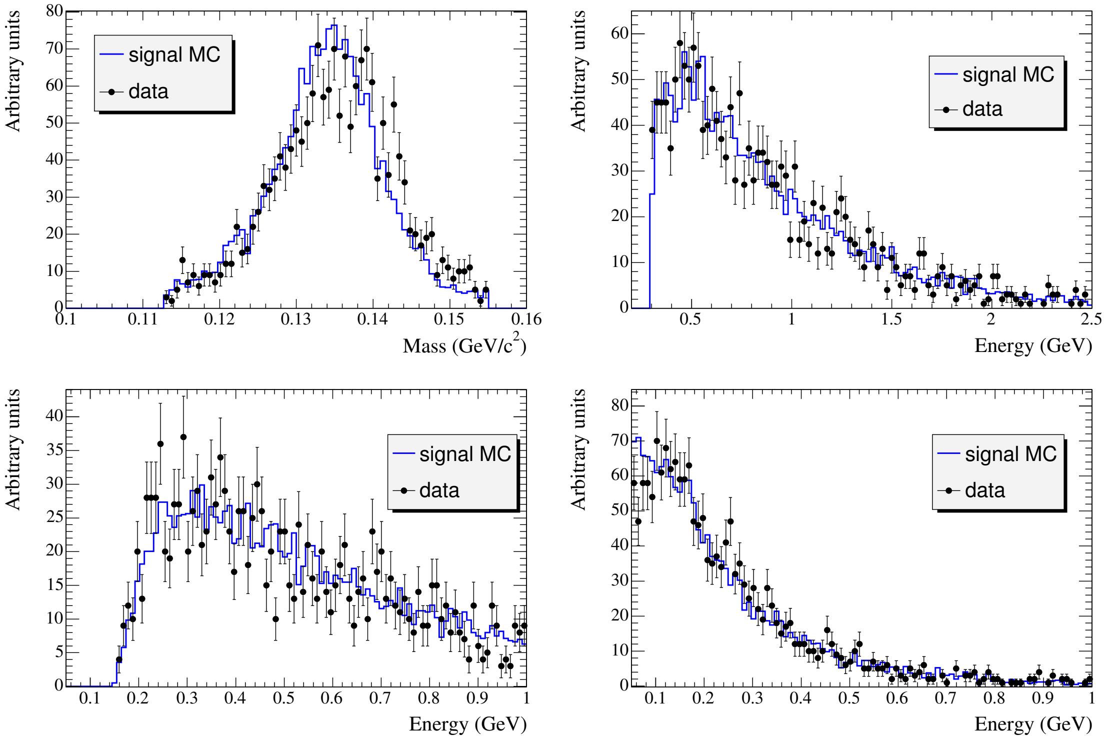

Figure 9.5: Reconstructed $\pi^0$ spectra in data (data point) and MC (blue histogram) signal. Top left: $\pi^0$ mass. Top right: $\pi^0$ energy. Bottom: energies of the $\pi^0$'s high-energy (left) and low-energy (right) daughter.

For comparison, Table 9.2 shows previously measured branching ratios and the current PDG value of the $\tau^- \to 3\pi^- 2\pi^+ \pi^0 \nu_\tau$ decay. Our result shows good agreement, which validates the event selection and the background estimate method used in the $\tau^- \to 3\pi^- 2\pi^+ \pi^0 \nu_\tau$ and $\tau^- \to 3\pi^- 2\pi^+ 2\pi^0 \nu_\tau$ analyses. Moreover, our measurement is more precise than the PDG value.

| | |
|---|---|
| $\tau^- \to 3\pi^-2\pi^+\pi^0\nu_\tau$ efficiency (%) | 2.16±0.16 |
| Expected $\tau$ background | 67±9 |
| Expected $q\overline{q}$ background | 84±42 |
| Observed data | 1742 |
| Extracted signal | 1591±38±122 |
| **Branching Ratio** | **(1.79±0.04±0.14)×10**$^{-4}$ |

Table 9.1: Final results of the $\tau^- \to 3\pi^-2\pi^+\pi^0\nu_\tau$ study. For comparison, the PDG value of the $\tau^- \to 3\pi^-2\pi^+\pi^0\nu_\tau$ branching ratio is $(1.81 \pm 0.27) \times 10^{-4}$.

| **Experiment** | **Branching Ratio** $(\times 10^{-4})$ |
|---|---|
| ALEPH, 96 | 1.8±0.7±1.2 |
| OPAL, 99 | 2.7±1.8±0.9 |
| CLEO, 01 | 1.7±0.2±0.2 |
| **PDG 2004** | **1.81±0.27** |

Table 9.2: Previous measurements of the $\tau^- \to 3\pi^-2\pi^+\pi^0\nu_\tau$ branching ratio quoted by the PDG 2004.

# CHAPTER 10

# SUMMARY AND CONCLUSION

We have searched for inclusive and exclusive decays of the $\tau$ lepton to 7 or 8 pion final states. We have analyzed $232\,\text{fb}^{-1}$ of data at center-of-mass energies on or near the $\Upsilon(4S)$ resonance, recorded with the *BABAR* detector at PEP-II asymmetric-energy $e^+e^-$-collider. The analyzed sample corresponds to more than 200 million $e^+e^- \rightarrow \tau^+\tau^-$ events, or more than 400 million $\tau$ decays. This data sample is substantially larger than those used in other experiments searching for similar decays.

We have followed a conventional cut-based technique to suppress the background and select the signal events. Monte Carlo simulation was used to study the properties of the signal and background. To reconstruct the signal events an approximation of the $\tau$ invariant mass, called pseudo mass, was used. It utilizes the approximation of the $\tau$ neutrino direction by the momentum vector of the seven hadrons, resulting in a significant improvement in the background rejection rate. We have found that the Monte Carlo does not adequately reproduce the $e^+e^- \rightarrow q\overline{q}$ events due to difficulties in modeling the fragmentation processes in rare multi-hadron decays. Therefore, the background estimate was extracted directly from the data by fitting it above the signal region with a PDF extracted from Monte Carlo and extrapolating the fit to the signal region for the background estimate. We used various cross-checks to validate this method.

Calculations suggest a very limited phase space for the seven-body $\tau$ decays and do not predict any signal up to $O(10^{-12})$ level, unless the decay goes through a resonance. Unfortunately, we did not see any evidence for a signal and calculated upper limits for branching ratios of various multi-pion decay channels, both inclusive and exclusive, presented in Table 10.1. For comparison, we also included the current results from the Particle Data Group 2004. For each of the decay modes we either have substantially improved the upper limit or present a result for the first time. In addition, we have measured the branching ratio of the $\tau^- \to 3\pi^-2\pi^+\pi^0\nu_\tau$ decay, which is consistent with and more precise than the PDG value.

In conclusion, these multi-pion $\tau$ decay modes are not likely to be observed with less than $1\,\mathrm{ab}^{-1}$ of data, which most likely rules out the observation by the *BABAR* experiment, but encourages other high-luminosity experiments to continue the search.

| **Multi-pion decay modes** | ***BABAR* (2005-2006)** | **PDG (2004)** |
|---|---|---|
| $\mathcal{B}(\tau^- \to 4\pi^-3\pi^+(\pi^0)\nu_\tau)$ | $< 3.0 \times 10^{-7}$ | $< 24 \times 10^{-7}$ |
| $\mathcal{B}(\tau^- \to 4\pi^-3\pi^+\nu_\tau)$ | $< 4.3 \times 10^{-7}$ | N/A |
| $\mathcal{B}(\tau^- \to 4\pi^-3\pi^+\pi^0\nu_\tau)$ | $< 2.5 \times 10^{-7}$ | N/A |
| $\mathcal{B}(\tau^- \to 3\pi^-2\pi^+2\pi^0\nu_\tau)$ | $< 3.4 \times 10^{-6}$ | $< 110 \times 10^{-6}$ |
| $\mathcal{B}(\tau^- \to 2\omega\pi^-\nu_\tau)$ | $< 5.4 \times 10^{-7}$ | N/A |
| $\mathcal{B}(\tau^- \to 3\pi^-2\pi^+\pi^0\nu_\tau)$ | $(1.79\pm0.04\pm0.14)\times10^{-4}$ | $(1.81\pm0.27)\times10^{-4}$ |

Table 10.1: Summary of the results of the multi-prong $\tau$ decay studies and comparison with the current data in the PDG 2004. The branching ratio upper limits are quoted at 90% confidence level.

# APPENDIX A

# GLOSSARY OF TERMS

### Luminosity

Instantaneous luminosity $\mathcal{L}$ at an $e^+e^-$ collider is defined as

$$\mathcal{L} = f n_B \frac{N_1 N_2}{A} \tag{A.1}$$

where $f$ is the revolution frequency, $n_B$ is the number of bunches in one beam, $N_i$ is the number of particles in each beam, and $A$ is the cross section of the beam. Integrated luminosity is given by $L = \int \mathcal{L} dt$

### Cherenkov radiation

When a charged particle passes through a medium at a speed greater than the speed of light in that medium ($v = c/n$, where $n$ is a refraction index in the medium), it emits electromagnetic radiation called Cherenkov radiation.

### Decay rate

Decay rate, $\Gamma$, of a particle is the probability per unit time that the particle will decay. If $N_0$ particles have a decay rate $\Gamma$, the number of particles at a given time $t$ is $N(t) = N_0 e^{-\Gamma t}$. The mean lifetime of the particle can be expressed as $\tau = 1/\Gamma$.

If a particle has several decay modes $\Gamma_i$ ($i = 1, ..., n$), the total decay rate is given by $\Gamma_{tot} = \sum_i \Gamma_i$ and the mean lifetime of the particle is $\tau = 1/\Gamma_{tot}$.

### Branching ratio

If a particle has a certain decay mode, its branching ratio is defined as

$$\mathcal{B} = \frac{\Gamma_i}{\Gamma_{tot}} \tag{A.2}$$

### Second-class currents

Depending on G-parity [10, 11], the hadronic currents in $\tau$ decay are separated into first-class currents ($J^{PG} = 0^{++}, 0^{--}, 1^{+-}, 1^{-+}$), and second-class currents with opposite G-parity ($J^{PG} = 0^{+-}, 0^{-+}, 1^{++}, 1^{--}$). To date only first class currents have been observed in $\tau$ decays.

### Lateral energy distribution (LAT)

LAT [33] measures the spread of the electromagnetic shower in the EMC:

$$LAT = \frac{\sum_{i=3}^{n} E_i r_i^2}{\sum_{i=3}^{n} E_i r_i^2 + E_1 r_0^2 + E_2 r_0^2}, \qquad E_1 \geq E_2 \geq ... \geq E_n \tag{A.3}$$

where the sum extends over all crystals in a shower, $r_0 = 5cm$ is the average distance between two crystal front faces, and $r_i$ is the distance between the $i$th crystal and the shower center. EM showers typically have smaller LAT than hadronic showers.

### Pion identification in *BABAR*

Pion identification in this analysis is based on a pion likelihood selector. The likelihood selector calculates the likelihood for each charged particle hypothesis, based on the information from the DIRC, DCH and SVT:

$$L_i = L_i^{DIRC} \times L_i^{DCH} \times L_i^{SVT} \tag{A.4}$$

The DCH and SVT likelihoods are based on comparison between the measured $dE/dx$ and the expected $dE/dx$ from the Bethe-Bloch parametrization [6]. Then the DCH and SVT likelihoods are calculated based on a Gaussian and a Bifurcated Gaussian PDFs respectively. The DIRC likelihood is based on the Cherenkov angle, number of photons, and track quality. Tight and loose identification of pions depends on $L_{(K)}/(L_{(K)} + L_{\pi})$ and $L_{(p)}/(L_{(p)} + L_{\pi})$ ratios. These ratios are close to zero for tightly identified pions.

### Lepton identification in ***BABAR***

Lepton $(e, \mu)$ identification in this analysis is based on cut-based electron and muon selectors. Tight and loose identification depends on the cut variables.

**Very tight electron** (used in $\tau^- \to 4\pi^- 3\pi^+ (\pi^0) \nu_\tau$ analysis) satisfies:

- $0.89 < E/p < 1.2$
- number of crystal hits $> 3$
- $540 < dE/dx$ (DCH) $< 860$
- $0.1 <$ LAT $< 0.6$
- A42 (Zernike Moment) [34] $< 0.11$
- DIRC cut: $3\sigma$ cut on the measured Cerenkov angle to be consistent with an electron hypothesis.
- Track-cluster matching cuts on the separation in $\phi$ between the track impact point into the EMC and the shower centroid $\phi$ (projected onto the front face of the crystal).

**Tight electron** (used in $\tau^- \to 3\pi^- 2\pi^+ 2\pi^0 \nu_\tau$ analysis) satisfies:

- $0.75 < E/p < 5.0$
- number of crystal hits $> 3$

- $500 < dE/dx$ (DCH) $< 1000$

- $0.0 <$ LAT $< 0.6$

**Very tight muon** (used in $\tau^- \to 4\pi^- 3\pi^+ (\pi^0) \nu_\tau$ analysis) passes:

- 0.05 GeV $< E_{CAL} <$ 0.4 GeV (for tracks in the angular region covered by EMC)

- number of IFR layers $> 1$

- $\Delta\lambda$ (expected number of interaction lengths - measured number of interaction lengths) $< 0.8$

- $\chi^2$ of the IFR track match $< 5$

- $\chi^2$ of the IFR track fit $< 3$

- $\lambda > 2.2$ (number of interaction lenghts)

- track continuity $> 0.34$

- average multiplicity of hit strips for each layer $< 8$

- standard deviation of the average multiplicity $< 4$.

**Tight muon** (used in $\tau^- \to 3\pi^- 2\pi^+ 2\pi^0 \nu_\tau$ analysis) passes:

- 0.05 GeV $< E_{CAL} <$ 0.4 GeV

- number of IFR layers $> 1$

- $\Delta\lambda < 1.0$

- $\chi^2$ of the IFR track match $< 5$

- $\chi^2$ of the IFR track fit $< 3$

- $\lambda > 2.2$

- track continuity $> 0.3$

- average multiplicity of hit strips for each layer $< 8$

- standard deviation of the average multiplicity $< 4$.

# APPENDIX B

# PSEUDO MASS

If the direction of the $\tau$ neutrino (and hence the $\tau$ lepton) was known the invariant mass of the $\tau$ could be simply calculated. Unfortunately, it is not known, however, it can be approximated. The ARGUS Collaboration introduced the pseudo-mass technique for $\tau$ mass calculations [27]. They approximate the $\tau$ neutrino direction by the combined momentum vector of the hadrons. The invariant mass with such an approximation is called a pseudo mass, and its spectrum is continuous at lower masses and has a sharp cutoff at the $\tau$ mass.

$$\begin{aligned}
m_\tau^2 &= P_\tau^2 = (P_h + P_{\nu_\tau})^2 \\
&= (E_h + E_{\nu_\tau})^2 - (\vec{p}_h + \vec{p}_{\nu_\tau})^2 \\
&= E_\tau^2 - (\vec{p}_h^2 + \vec{p}_{\nu_\tau}^2 + 2|\vec{p}_h||\vec{p}_{\nu_\tau}|cos(\vec{p}_h, \vec{p}_{\nu_\tau})) \\
&= E_\tau^2 - \vec{p}_h^2 - E_{\nu_\tau}^2 - 2|\vec{p}_h|E\nu_\tau cos(\vec{p}_h, \vec{p}_{\nu_\tau})) \\
&= 2E_h(E_\tau - E_h) + m_h^2 - 2|\vec{p}_h|(E_\tau - E_h)cos(\vec{p}_h, \vec{p}_{\nu_\tau}))
\end{aligned}$$

where $E_{\nu_\tau} = E_\tau - E_h$ is used and $m_{\nu_\tau}$ is approximated to be zero. Index $h$ here stands for a hadron, but for a multi-prong event $P_h$ and $E_h$ describe the total momentum and energy of multi-prong tracks. The neutrino direction is approximated by the total multi-prong momentum vector, hence $cos(\vec{p}_h, \vec{p}_{\nu_\tau}) = 1$. Substituting $E_{beam}$ for $E_\tau$ we get:

$$m_\tau^{2*} = 2E_h(E_\tau - E_h) + m_h^2 - 2|\vec{p}_h|(E_\tau - E_h)$$

$$m_\tau^{2*} = 2(E_\tau - E_h)(E_h - |\vec{p}_h|) + m_h^2$$

which is the expression 3.3 for the 7-prong events.

Figures B.1 and B.2 compare the 7-prong pseudo-mass with invariant mass.

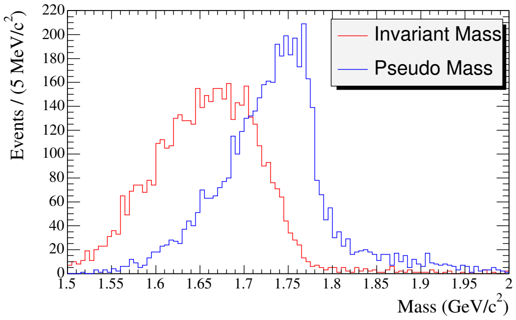

Figure B.1: Comparison of the 7-prong invariant mass and pseudo-mass.

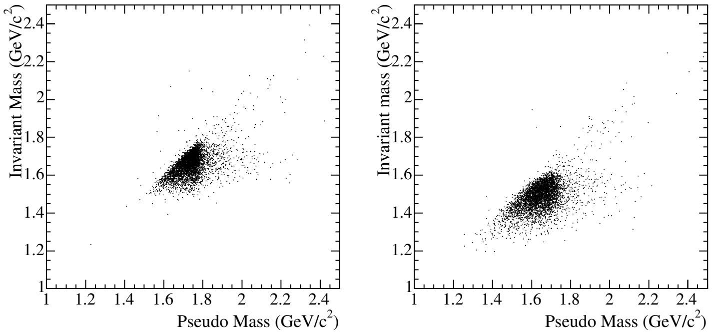

Figure B.2: The 7-prong invariant mass vs. pseudo mass. Left plot: $\tau^- \rightarrow 4\pi^- 3\pi^+ \nu_\tau$ mode, right plot: $\tau^- \rightarrow 4\pi^- 3\pi^+ \pi^0 \nu_\tau$ mode

# BIBLIOGRAPHY

[1] M. L. Perl *et al.*, Phys. Rev. Lett. **735**, 1489 (1975).

[2] M. L. Perl *et al.*, Phys. Lett. B **63**, 466 (1976).

[3] J. Burmester *et al.*, Phys. Rev. B **68**, 297 (1977).

[4] R. Brandelik *et al.*, Phys. Lett. B **70**, 125 (1977).

[5] M. L. Perl *et al.*, Phys. Lett. B **70**, 487 (1977).

[6] S. Eidelman *et al.*, (Physics Data Group), Phys. Lett. B **592** 1 (2004).

[7] B. Bysma *et al.*, (HRS Collaboration) Phys. Rev. D **35**, 2269 (1987).

[8] K. Ackerstaff *et al.*, (OPAL Collaboration) Phys. Lett. B **404**, 213 (1997).

[9] K. Edwards *et al.* (CLEO Collaboration), Phys. Rev. D. **56**, 5297 (1997).

[10] D. Griffiths, “Introduction to Elementary Particles” (John Wiley & Sons Inc., NY, 1987).

[11] A. Stahl, “Physics with Tau Leptons” (Springer-Verlag Berlin Heigelberg 2000).

[12] A. Pich, e-Print Archive: hep-ex/0203002.

[13] S. Nussinov and M. V. Purohit, Phys. Rev. D **65** 034018 (2002).

[14] A. Anastassov *et al.* (CLEO Collaboration), Phys. Rev. Lett. **86**, 4467 (2001).

[15] R. Barate *et al.* (ALEPH Collaboration), Euro. Phys. J. C **2**, 395 (1998).

[16] D. Gibaut *et al.* (CLEO Collaboration), Phys. Rev. Lett. **73**, 934 (1994).

[17] R. J. Sobie, Phys. Rev. D **60**, 017301 (1999).

[18] A. Pais, Ann. Phys. (N.Y.) **9**, 548 (1960).

[19] B. Aubert *et al.* (BABAR Collaboration), Phys. Rev. D **72** 012003 (2005).

[20] B. Aubert *et al.* (BABAR Collaboration), To be submitted to Phys. Rev. D. (2006).

[21] PEP-II – An asymmetric B Factory, Conceptual Design Report, SLAC-418, LBL-5379, 1993.

[22] B. Aubert *et al.* (BABAR Collaboration), Nucl. Instrum. Meth. **A479**, 1 (2002).

[23] http://root.cern.ch/

[24] B. F. Ward, S. Jadach and Z. Was, Nucl. Phys. Proc. Suppl. **116**, 73 (2003).

[25] S. Jadach, Z. Was, R. Decker and J. H. Kuhn, Comput. Phys. Commun. **76** 361 (1993).

[26] T. Sjostrand et al., "Pythia 6.2, Physics and Manual", (2002). e-Print Archive: hep-ph/0108264.

[27] H. Albrecht *et al.* (ARGUS Collaboration), Phys. Lett. B**292**, 221 (1992).

[28] T. Skwarnicki, DESY internal report DESY-F31-86-02 (1986).

[29] G. Cowan, "Statistical Data Analysis" (Clarendon Press Oxford 1998) 34.

[30] F. James and M. Roos, Comput. Phys. Commun. **10** 343 (1975).

[31] R. Barlow, Comput. Phys. Commun. **149** 97 (2002).

[32] R. D. Cousins and V. L. Highland, Nucl. Instr. Meth. A**320** 331 (1992).

[33] A. Drescher *et al.* (ARGUS Collaboration), Nucl. Instrum. Meth. **A237**, 464 (1985).

[34] R. Sinkus and T. Voss, Nucl. Instrum. Methods, **A391**, 360 (1997)